Optimization of airfoils and wing planforms for airborne wind energy applications

Sina Rangriz

A Thesis

in

The Department

of

Mechanical, Industrial and Aerospace Engineering

Presented in Partial Fulfillment of the Requirements

For the Degree of Master of Applied Science (Mechanical Engineering)

Concordia University

Montréal, Québec, Canada

August 2024

Concordia University

School of Graduate Studies

This is to certify that the thesis prepared

By: **Sina Rangriz**

Entitled: **Optimization of airfoils and wing planforms for airborne wind energy applications**

and submitted in partial fulfillment of the requirements for the degree of

Master of Applied Science (Mechanical Engineering)

complies with the regulations of this University and meets the accepted standards with respect to originality and quality.

Signed by the final examining committee:

_____ Dr. Marius Paraschivoiu, Chair and Internal Examiner

_____ Dr. Ebenezer Ekow Essel, External Examiner

_____ Dr. Mojtaba Kheiri, Supervisor

Approved by _____

Dr. Muthukumaran Packirisamy, Chair

Department of Mechanical, Industrial and Aerospace Engineering

_____ 2024 _____

Dr. Mourad Debbabi, Dean

Gina Cody School of Engineering and Computer Science

Abstract

Optimization of airfoils and wing planforms for airborne wind energy applications

Sina Rangriz

This research work focuses on the optimization of airfoils and wings for the use in airborne wind energy applications, especially crosswind kite power systems. The thesis is divided into three major parts. Each part includes an optimization framework which is composed of four blocks: an airfoil or wing geometry builder, an aerodynamic solver, an optimizer, and a post-processor. These blocks interact with each other to solve the problem of maximizing/minimizing an aerodynamic objective function while at the same time maximizing/minimizing a structural objective function such as airfoil thickness or wing aspect ratio. It is thus inevitable to have a multi-objective framework that includes both objective functions.

The first part addresses airfoil optimization by minimizing the inverse aerodynamic efficiency and the negative maximum thickness ratio, which are conflicting objectives. Results with and without induced drag (from a finite aspect ratio wing) and tether drag effects show that optimal airfoils accounting for induced drag have a cusped trailing edge, while those considering tether drag have a flap-like trailing edge, both improving aerodynamic performance.

The second part focuses on wing planform optimization, aiming to minimize the inverse aerodynamic efficiency and aspect ratio simultaneously. The optimization framework is

validated by minimizing the drag-to-lift ratio, resulting in wings with elliptic planforms. The planforms optimized for aerodynamic efficiency do not differ significantly from elliptic shapes.

The third part of the thesis deals with the optimization of box-wing airfoils. Box-wings consist of two wings connected by vertical fins at their tips, forming a box-like shape when viewed from the front. The analysis is performed for an infinite aspect ratio, i.e., two-dimensional configuration. The inverse of the total aerodynamic efficiency and the negative of the combined maximum thickness ratio of the two airfoils are minimized simultaneously. The numerical results indicate that the optimal configurations feature a thick lower (or forward) airfoil and a thin upper (or aft) airfoil. This suggests that the lower airfoil primarily serves a structural role, while the upper airfoil plays a crucial aerodynamic role.

Acknowledgments

This page will show the real contributors to this project. I would like to express my deepest gratitude to Dr Mojtaba Kheiri for their invaluable guidance, encouragement, and unwavering support throughout this research journey. Their expertise, patience, and insightful feedback have been instrumental in shaping the direction and quality of this thesis. My heartfelt appreciation goes to my family for their support, understanding, and sacrifices, especially my father who taught me to be strong, kind, composed, and motivated in the journey of life. I am immensely grateful to Negar for their love, understanding, and constant encouragement as a part of this journey. Their unwavering belief in me has been a source of strength and motivation. I would like to thank my friends and colleagues, Amar, Mohadeseh, Sanaz, Hossein, Kyana, Durai, Mahdi, Antoine, Ehsan, Vitor, Mehdi, and Reza for helping me during this journey. It is worth expressing my sincere gratitude for the funding provided by NSERC and Concordia University. Lastly, I would like to express my sincere gratitude to the people I lost in my way and the people who stayed beside me to complete this study. This thesis would not be completed without the collective support and encouragement of all mentioned above.

Contents

List of Figures

List of Tables

Chapter 1

Introduction to Airborne Wind Energy and Crosswind Kite Power Systems

1.1 Background

Over the past few decades, the increasing global population has heightened the energy demand. Fossil fuels as energy sources have accelerated global warming and climate change. The non-renewable nature of conventional fuels also affects their future dependability. To fight off these challenges while addressing global energy needs, renewable energy resources, such as wind, hydro, and solar should be leveraged.

The drive towards sustainable energy sources also motivates researchers to innovate for energy efficiency. Within the wind energy sector, there are a few novel ideas that show significant promise. One such recent innovative concept is Airborne Wind Energy (AWE) which utilizes airborne modules tethered to the ground to harness wind energy from high

altitudes. These systems use less material by replacing traditional wind turbine towers with very light tethers. They can also capitalize on the stronger and steadier winds at higher altitudes. This results in a significantly improved mass of the system-to-its power output ratio compared to conventional wind turbines and thus has the potential to reduce the unit cost of energy considerably [16, 17].

AWE systems can be classified based on several factors. Broadly, they fall into two categories: flying systems and aerostatic systems. Depending on the flight path of the airborne module, they can be further categorized into crosswind, tether-aligned, and rotational types. Classification can also be based on the structure of the airborne module, distinguishing between soft kites and rigid kites. Additionally, take-off and landing methods serve as another basis for classification. The tether configurations, such as single, bridle, dual, and multiple, also provide a framework for categorizing AWE systems; for more details on the AWE classification, the reader is referred to [18–20].

Crosswind Kite Power Systems (CKPSs) represent a class of airborne devices initially proposed by Loyd in his seminal work [21]. This groundbreaking paper introduced the concept of harnessing wind energy through a kite flying crosswind. Loyd's work also provides simplified equations for estimating the power output of these systems, emphasizing the critical role of crosswind motion. This motion increases the kite's relative velocity beyond the ambient wind speeds, thereby significantly enhancing its power generation capacity.

A CKPS can utilize one or more kites tethered to a ground station, flying at velocities several times the wind speed. For optimal energy production, the wind direction forms a small angle with the kite's axis of rotation [22]. The trajectory of the kite can be controlled using a combination of reel-in and reel-out forces, aerodynamic forces, and control surfaces.

CKPSs can be classified into various types based on their operation or configuration. However, Loyd categorized them into two primary types based on the power generation

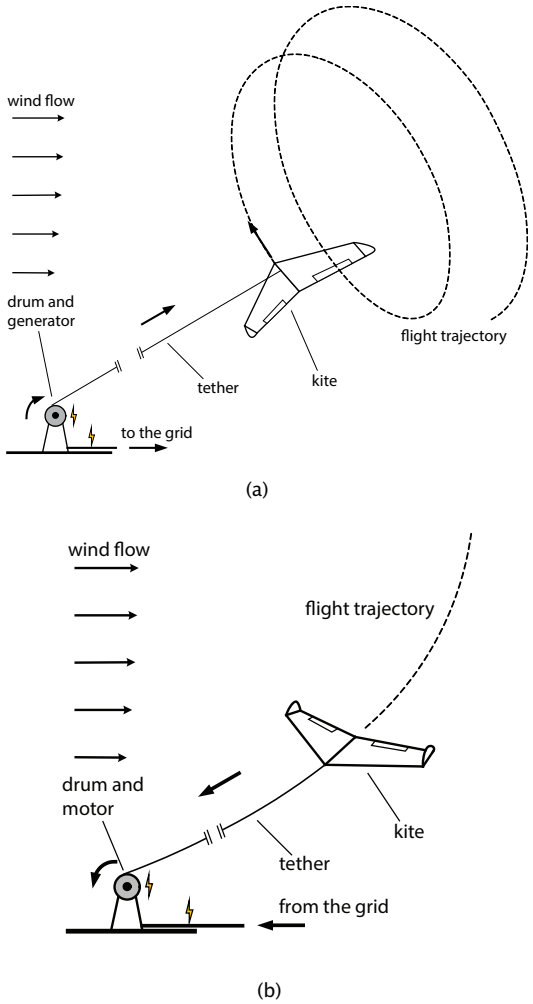

Figure 1.1: Schematic drawings showing the lift mode or ground-based power generation: (a) reeling-out or power generation phase, and (b) reeling-in or power consumption phase. The images were reproduced from [1].

mode: lift-mode and drag-mode systems, as shown in Fig. 1.1 and Fig. 1.2, respectively. In lift-mode systems, the aerodynamic forces generated by the kite are mechanically transmitted to the ground via a reel-in/reel-out motion of the tether. The winch from which tether reel-in/reel-out, is connected to a generator that produces electricity during the reel-out phase. Conversely, drag-mode systems have turbines coupled to generators onboard the airborne module. The electricity generated in the airborne module is then transmitted to the ground

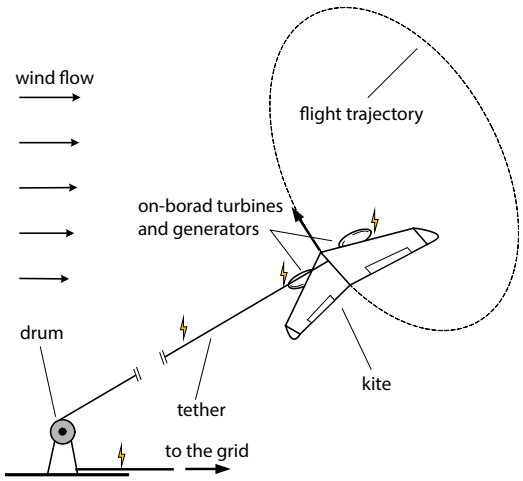

Figure 1.2: A schematic drawing showing the drag mode or on-board power generation. The image was reproduced from [1].

through conducting tethers. The lift-mode systems are also known as ground-gen systems and the drag-mode systems as fly-gen systems.

As also shown in Fig. 1.1, the power generation cycle of a lift mode CKPS comprises two main stages: the power production phase and the power consumption phase. During the power production phase, the aerodynamic forces on the kite pull the tether, causing it to reel out from a winch. This phase generates energy, as the winch is connected to a generator. Once the kite reaches a designated altitude, the power consumption phase begins, during which the tether is reeled in using energy, and the kite is retracted to its initial position. The end of this stage marks the beginning of the next cycle. The two stages are optimized to ensure a net positive energy output.

The operational cycle of a drag-mode CKPS differs significantly from that of a lift-mode system. In a drag-mode system, power is generated onboard using turbines coupled to generators. The generated energy is then transmitted to the ground through a conductive tether. Unlike lift-mode systems, drag-mode systems have simpler dynamics because they do not involve reel-in/reel-out motion. However, the construction of tethers in drag-mode

systems is more complex due to the need for transferring electricity to the ground.

Flying in crosswind conditions enables CKPSs to achieve velocities several times greater than the wind speed, leading to increased aerodynamic forces and consequently higher power generation. Additionally, CKPSs can harvest wind energy from larger areas compared to aerostatic systems. However, their complex dynamics present significant reliability challenges, which remain a major obstacle to their widespread industrial deployment [16].

Despite these challenges and having a low Technology Readiness Level (TRL), interested readers refer to this study [23] for TRL definition, the potential for material savings, simplified maintenance procedures, and enhanced power production make CKPSs and other AWE systems attractive to the wind energy industry.

In recent decades, several companies like Kitemill, Skysails, TwingTec, and Skypull have developed ground-gen prototypes, while Makani, Kitekraft, and Windlift have focused on fly-gen prototypes. Makani's M600 kite is shown in Fig. 1.3. Typically, these kites operate at altitudes ranging from 300 m to 1000 m. This altitude range is chosen because flying higher, from 1000 m to 4000 m, minimally increases wind speeds and necessitates excessively long tethers [24]. Loyd [21] originally predicted similar power outputs for ground-gen and fly-gen systems, but recent studies suggest varying performance advantages; for further details, interested readers are referred to [1, 22, 25].

The three major components of a CKPS are (i) airborne module, (ii) tether, and (iii) ground station.

The aerodynamics of the system are primarily influenced by the airborne module and the tether. The tether drag is significant and should not be neglected when predicting the aerodynamic performance of the system. Special attention should be given to the aerodynamic design of the kite wing, including the airfoil profile, planform shape, and aspect ratio since it is generating most of the aerodynamic forces needed for flying and power generation.

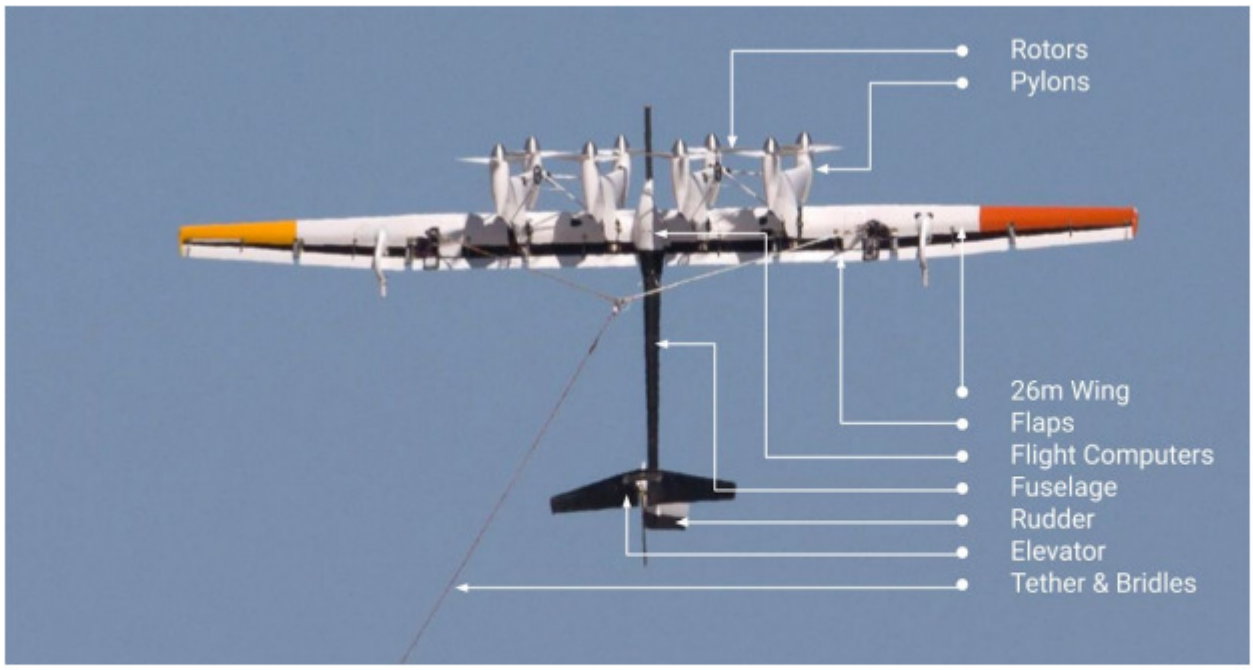

Figure 1.3: Figure showing the M600 Makani kite and its components. The image was reproduced from [2].

A simplified formula for the power output of a kite operating in a pumping mode has been derived in a paper by Argatov [26]. This formula underscores the significance of parameters such as aerodynamic lift and lift-to-drag ratio in determining the power output. The aerodynamic performance of crosswind kite power systems has been extensively studied in recent years [22, 27, 28]. These studies highlight the potential advantages of CKPSs compared to conventional wind turbines.

Other significant areas of interest in AWE include the dynamics and control of the system, as well as its structural design. Control systems play a crucial role in stabilizing the dynamics of the kite and maintaining an optimal flight trajectory to maximize power output [19]. Additionally, an optimal structural design can reduce the weight of the kite, enhancing power production capacity and ensuring system reliability under sudden load fluctuations. The use of composite materials is common for constructing lighter kites [29].

In conclusion, optimizing the power output of crosswind kite power systems demands a thorough understanding of their aerodynamics, structure, and control strategies. Aerodynamic parameters like lift and drag coefficients must be finely tuned through optimization. Given that the performance requirements and operational envelopes differ from traditional aircraft or wind turbines, a dedicated, robust, and efficient optimization framework is crucial for CKPSs. Additionally, exploring novel wing designs such as box-wing configurations could significantly enhance the efficiency and performance of the system.

1.2 Motivation

CKPSs represent an emerging technology currently at a low TRL. The operation of these kites presents significant challenges, and recent industry efforts have primarily concentrated on developing functional prototypes. These prototypes typically employ airfoils commonly used in the aerospace or wind turbine industry, which are not optimized for kite performance. Due to distinct performance requirements and operational conditions, the aerodynamic design of kites must be different.

Ideally, CKPS designers should have access to a wide variety of airfoils to achieve optimal power output. However, the current selection is limited. Given the promising potential of CKPSs, choosing optimized airfoils and planform configurations could significantly advance the industry. Aerodynamic solvers, such as XFOIL and MSES, are valuable tools that can aid in developing better designs specifically tailored for CKPS applications.

1.3 Objectives

This thesis explores the aerodynamic optimization of airfoils and wings for harnessing wind power in AWE systems. In particular, the primary objectives are categorized as follows:

1. Create an airfoil optimization framework specifically for monoplane CKPSs and analyze how induced drag and tether drag influence the optimal airfoil profiles.

2. Develop a planform optimization framework for CKPS wings.

3. Develop an airfoil optimization framework for box-wing CKPSs.

1.4 Literature review

1.4.1 Aerodynamic theory of CKPS

Understanding the aerodynamics of CKPSs is essential for comprehending how aerodynamic forces are converted into power by the system. Developing equations for power output, incorporating rotational effects, aerodynamic interactions, and aerodynamic coefficients is critical for identifying key performance parameters and clarifying the relationship between aerodynamics and power generation.

Research has extensively explored the design of drag power kites, highlighting the critical role of high aerodynamic lift coefficients in the performance of CKPSs [30]. Additionally, precise modeling of these kites necessitates direct measurements of the velocity vector, angle of attack, and sideslip angle [31]. This underscores the complexity of kite aerodynamics and emphasizes the need for comprehensive aerodynamic measurements in research and development.

Flying crosswind at a large radius enables kites to harness wind power over a broader area and produce substantial aerodynamic forces [28]. The lift and drag coefficients of kites change with power adjustments, steering inputs, and flight trajectory orientation, underscoring the intricate nature of kite aerodynamics [32]. However, these dynamic characteristics

of aerodynamic coefficients are often overlooked during the initial design phases.

CKPSs generate power from aerodynamic forces. A well-known factor in the aerodynamic performance of conventional airplanes is the glide ratio, represented as C_L/C_D, where C_L and C_D are the lift coefficient and drag coefficient, respectively. CKPSs also utilize similar coefficients to generate thrust (the drag created by the onboard turbines) in drag mode and a pulling force in lift mode [27].

Identifying the key aerodynamic performance parameters is essential for optimizing CKPSs. Some research has focused on developing dynamic and quasi-steady models for kite power systems [33, 34]. These models account for factors such as gravity, tether length, and wind conditions to accurately predict the behavior of kite power systems [33]. Additionally, developing power production equations that consider passivity can determine the power limits of crosswind kites, providing insights into the maximum power that can be harvested [35].

The preliminary aerodynamic design relies on computationally faster analytical models, such as actuator disc theory, rather than computationally expensive Computational Fluid Dynamics (CFD) analyses.

In a study by Kheiri et al., [27], the generalized power equation for CKPSs is derived using the actuator disc theory. This approach assumes steady wind conditions with airflow reaching the rotor perpendicularly. Considering an actuator disc moving downwind at a speed of v_d (Fig. 1.4), the flow velocity at the disc, v_r, is given by

$$v_r \equiv (v_\infty - v_d)(1 - a), \tag{1.1}$$

where v_∞ is the freestream velocity, v_d is the velocity at which the disc moves, and a is the induction factor.

The induction factor is a non-dimensional parameter that indicates the kinetic energy

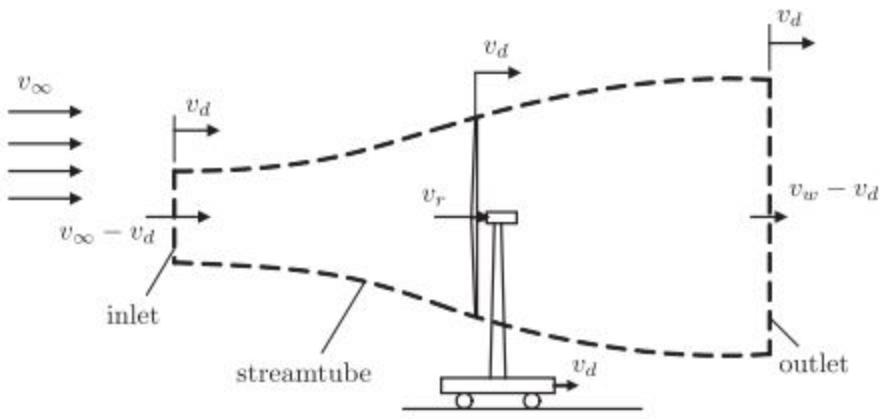

Figure 1.4: Schematic of a *streamtube* extended from upstream to downstream of a wind turbine which is moving with a constant speed of $v_d = ev_\infty$ subjected to an incoming wind where v_∞ is the uniform wind field velocity, i.e., freestream velocity. The inlet and outlet velocities are $v_\infty - v_d$ and $v_w - v_d$, respectively. Also, $0 \leq e \leq 1$ which defines as the ratio of reel-out to freestream velocity [1].

loss across the disc. Furthermore, based on the extended actuator disc theory, the absolute wake velocity is $v_w = v_\infty[1 - 2a(1 - e)]$, where $e = v_d/v_\infty$ is called the reel-in/reel-out ratio. To find the power output of this system, which is similar to the lift-mode kite, the thrust is multiplied by the reel-in/reel-out velocity v_d. Interested readers can refer to [27] for more details.

lift mode power generation

Utilizing the extended actuator disc and blade element momentum theory, and equating the total axial force generated by the kite to the total axial aerodynamic force acting on the kite, the induction factor of a kite flying in lift mode can be obtained from [27]

$$\frac{a}{1-a} = \frac{1}{4}\left(\frac{A_k}{A_s}\right) C_L \left(\frac{C_L}{C_D}\right)^2, \tag{1.2}$$

where A_k represents the kite planform area while A_s is the swept area, i.e., the annulus swept by the kite while flying in the sky.

The power output in lift mode is the product of the thrust and reel-out speed, which can be expressed as a function of aerodynamic coefficients and the induction factor, as given by Equation 1.3:

$$P_L = Tv_d = \left(\frac{1}{2}\rho A_s v_\infty^3\right) C_L \left(\frac{C_L}{C_D}\right)^2 (1-a)(1-e)^2 e. \tag{1.3}$$

The swept-area-normalized power coefficient, which is consistent with wind turbine literature is given by:

$$C_{PL}^{(s)} = \frac{P_L}{\frac{1}{2}\rho A_s v_\infty^3} = 4a(1-a)(1-e)^2 e, \tag{1.4}$$

while the kite-area-normalized power coefficient is given by

$$C_{PL}^{(k)} = \frac{P_L}{\frac{1}{2}\rho A_k v_\infty^3} = \frac{4}{\sigma} a(1-a)(1-e)^2 e, \tag{1.5}$$

where $\sigma = A_k/A_s$ may be considered as solidity factor.

Theoretically, the maximum of $C_{PL}^{(k)}$ is achieved when the kite sweeps an infinitely large area, i.e., $\sigma = A_k/A_s \to 0$, and $e = 1/3$

$$C_{PL,max}^{(k)} = \frac{4}{27}\chi, \tag{1.6}$$

where $\chi = C_L(C_L/C_D)^2$ which is called the aerodynamic efficiency [1].

Drag mode power generation

Theoretically speaking, in drag mode crosswind kites, power is generated by the thrust of small wind turbines mounted on the kite's wing. The direction of the thrust is closely aligned with the direction of the relative wind and contributes to the drag of the airborne module.

Assuming that this drag acts in the same direction as the kite's overall drag, the efficiency of power generation can be expressed as the ratio of the drag force introduced by the turbines to the total drag of the kite, denoted as $\kappa = D_p/D = C_{D_p}/C_D$. The induction factor can be formulated as:

$$\frac{a}{1-a} = \frac{1}{4}\left(\frac{A_k}{A_s}\right) C_L \left(\frac{C_L}{C_D}\right)^2 \left(\frac{1}{1+\kappa}\right)^2. \tag{1.7}$$

The general expression for the power in drag mode is found by multiplying the thrust with the crosswind speed as given below:

$$P_D = \left(\frac{1}{2}\rho A_k V_\infty^3\right) C_L \left(\frac{C_L}{C_D}\right)^2 (1-a)^3 \frac{\kappa}{(1+\kappa)^3}. \tag{1.8}$$

Thus, the kite-area-normalized power coefficient can be written as

$$C_{PD}^{(k)} = C_{PD}^{(k)}(\sigma, \chi, e) = \frac{P_D}{\frac{1}{2}\rho A_k v_\infty^3} = \frac{\chi}{\left((1+\kappa)^2 + \frac{1}{4}\chi\sigma\right)^3} \kappa(1+\kappa)^3. \tag{1.9}$$

The maximum value of $C_{PD}^{(k)}$ occurs when the kite is sweeping an infinitely large area, which means $\sigma = 0$, and when the thrust produced by the onboard turbines is half of the total drag of the kite, i.e., $\kappa = 1/2$. These lead to

$$C_{PD,max}^{(k)} = \frac{4}{27}\chi. \tag{1.10}$$

From Eqs. 1.6 and 1.10, one can conclude that with a negligible solidity factor, σ, the maximum power generation in both lift and drag modes would be the same. A similar observation was also made in [21]. As shown in later chapters concerning the optimization framework, the aerodynamic objective function will include the aerodynamic efficiency term,

χ.

1.4.2 Aerodynamic optimization

Aerodynamic shape optimization improves the performance by refining the design of objects interacting with airflows, such as wind turbines, aircraft, and automobiles. For example, optimizing the shape of an airfoil can enhance its glide ratio, a key objective in aerospace engineering. Similar optimization strategies have the potential to boost power generation within the AWE industry. Recent advancements in high-speed computation have enabled the use of high-fidelity CFD solvers, mesh deformation techniques, and optimization tools to address this problem.

While extensive research has focused on optimizing airfoils and blades for wind turbines, there remains a notable gap in aerodynamic optimization specifically tailored for CKPSs and other AWE systems. For CKPSs, equations 1.6 and 1.10 demonstrate that the maximum power coefficient of the kite in both lift and drag modes depends on the aerodynamic efficiency χ. Therefore, a primary objective of this thesis is to maximize this coefficient by exploring variations in airfoil shape, wing planform, and using unconventional wing designs such as box-wings. This section will be structured as follows: firstly, relevant studies on the aerodynamic optimization of wind turbine blades and airfoils will be reviewed. Next, a literature review focusing on efforts in aerodynamic optimization for AWE and CKPSs will be provided.

Aerodynamic optimization of wind turbine blades and airfoils

The shape and orientation of the blade relative to the wind are crucial factors influencing the power produced. A blade can comprise different airfoils from root to tip and incorporate geometric twists to accommodate varying incoming flow angles. Aerodynamics of blades can

be optimized for various purposes, such as maximizing power output and minimizing power loss due to occurrences like ice formation, leading-edge contamination, wake interaction, and wind shear. This process involves modifying the blade's design variables, including shape, angles, and placement on the rotor, among others.

Zhang et al. [36] proposed a method for optimizing wind turbine blades that addresses the challenges of complex aerodynamic loads while ensuring the structurally sound design of the blades. The objective of the work was to maximize the glide ratio, or lift-to-drag ratio, by incorporating the torsional rigidity of the blade into the equations. The Class-Shape Transformation (CST) method was used to characterize airfoil geometry, and CFD along with MATLAB-based structural codes were employed for aerodynamic and structural analysis, respectively. To reduce computational costs, a surrogate model was developed, and airfoils, such as NACA64618, DU91-W2-250, and DU97-W-350 were optimized. This study highlights the importance of using a reliable aerodynamic solver in the optimization framework, with an emphasis on the structural considerations of the blade.

Low-fidelity aerodynamic solvers are often implemented in the optimization framework to reduce computational costs. For example, in [37], the wind turbine's airfoil optimization framework addresses the performance reduction caused by leading edge contamination due to icing effects. CST was employed to parameterize the airfoils. In addition, a modified version of XFOIL and an optimizer based on the derivative-free Covariance Matrix Adaptation Evolution Strategy were used.

The evolutionary algorithms are often applied in optimization studies where multiple aspects of the design should be examined. For instance, Benim et al. [38] combined CFD simulations with the Response Surface Method to evaluate the aerodynamic performance of the airfoils. The Bi-objective Mesh Adaptive Direct Search method was utilized as the optimizer to maximize the power and minimize the standard deviation of thrust within a

predefined space for flow variables. This method utilized two objective functions highlighting the significance of considering conflicting objectives in the optimization framework.

Aeroacoustic optimization can also be of interest in the wind turbine field. For example, in [39], three objective functions, i.e., aerodynamic, structural, and acoustic objective functions, were combined to make a new objective function. In this study, the modified version of XFOIL, known as RFOIL, and the Archive-based Micro Genetic Algorithm were used as the aerodynamic solver and optimization method, respectively.

As an example of minimization of the aerodynamic loss, Yitrici [40] studied the effect of ice formation at the leading edge of the wind turbine blade on the aerodynamic performance of the wind turbine. The blade profile shape has a significant role in the ice formation. Thus, optimization of the profile shape while considering various icing conditions was investigated. Blade element momentum theory along with a method for ice formation prediction was implemented in a gradient-based optimization framework to find the optimal blade profiles.

Different aspects of aerodynamics, such as acoustics, force, wake, and stability, are crucial considerations. It is up to the designer to select and frame the objective functions to address the operational and performance requirements. Whether the optimization method is global or local depends on the nature of the problem and the depth of the study.

Optimization of AWE and CKPS devices

Research on AWE technologies over the last decades has significantly focused on understanding and predicting their effectiveness. This includes investigations into structural integrity, aerodynamic performance, and control systems, among others. Notably, recent studies such as those cited in [13, 41–45] have delved into the aerodynamic analysis specific to CKPSs.

In his thesis [13], Kroon devised a framework to optimize airfoils for rigid wings used in crosswind kite power systems. He employed RFOIL, a variant of XFOIL tailored for wind

turbines, as the aerodynamic solver and utilized Non-dominating Sorting Genetic Algorithm II (NSGA-II) for the optimization. Airfoil parameterization was achieved using the CST function. The primary aerodynamic objective of the study was to maximize aerodynamic efficiency, denoted earlier as χ, while simultaneously considering the maximum thickness-to-chord ratio as a structural objective function.

The aerodynamic characteristics of airborne wind turbines share similarities with conventional wind turbines, but certain differences exist. Saleem and Kim [43] introduced an optimization framework for an airfoil of an airborne wind turbine. They utilized the PARSEC airfoil parameterization method and XFOIL to enhance the performance of the NACA 9415 airfoil, aiming to maximize the lift coefficient through the application of a genetic algorithm.

One approach to enhance the performance of CKPSs involves using multi-element airfoils, which can adapt to different operational requirements. Porta Ko et al. [42] introduced a multi-objective optimization framework. They employed MSES, a specialized low-fidelity aerodynamic solver for multi-element airfoils, and utilized NSGA-II for optimization. Their framework focused on optimizing flap settings during the production phase with considerations for the consumption phase.

Low- and high-fidelity simulations of a box-wing configuration were performed in [41]. This research highlights the importance of innovations in AWE. They automated CFD mesh creation while incorporating eight design parameters using Pointwise. The simulations utilized Reynolds-averaged Navier-Stokes (RANS) equations. The turbulence closure was achieved through the $k-\omega$ SST equations. APAME and OpenFoam were employed as low- and high-fidelity software within this framework.

Beyond the aerodynamic aspect, the optimization framework can also include considerations for cost, trajectory, and control systems.

The dynamic behavior of the kite in the presence of gusts was studied in [45]. A sensitivity analysis of the traction force was conducted to determine the degree of dependence of this force on trajectory parameters. An adaptive algorithm was developed to maximize real-time traction as a result of aerodynamic forces.

Trevisi et al. [44] investigated the annual power production and economic aspects of CKPSs using a unified model. The results demonstrated a slight superiority of drag-mode kites, highlighting their competitiveness. A gradient-based optimization algorithm was employed in the study, and sensitivity analysis was performed using a surrogate model.

Trajectory optimization was studied in [46], where a reduced-order optimal control problem that contains only the periodic behavior of the trajectory in the frequency domain is to be solved. This problem was implemented in a gradient-based optimization framework, with the objective function being the negative value of thrust, shaft power, or electric power averaged over a single loop of flight.

Optimization of control strategies was proposed and validated experimentally in [47], demonstrating improved power generation of crosswind kites. Tracking control was studied in [48], where an empirical law connected the kite's steering input and the yaw rate. This research highlighted the potential for autonomous flight during the traction phase of CKPSs. Additionally, the operational phases have been studied in [49], facilitating the automation of the kite.

Although the literature on AWE is extensive, a robust optimization framework for the aerodynamic performance of AWE is still lacking. Additionally, novel wing configurations such as box-wing should be investigated to enhance designs for higher power production and improved aerodynamic performance. A design framework that incorporates both aerodynamic and structural considerations still needs further development.

1.5 Contributions

The main contributions of this study are summarized in the following research papers:

Journal papers:

- Rangriz, S., Kheiri, M. (2024). Designing optimal airfoils for crosswind kite power systems. Journal of Wind Engineering & Industrial Aerodynamics (under review).
- Kheiri, M., Victor, S., Rangriz, S., Karakouzian, M. M., & Bourgault, F. (2022). Aerodynamic performance and wake flow of crosswind kite power systems. Energies, 15(7), 2449.

Conference papers/presentations:

- Rangriz, S., & Kheiri, M. (2023). Design of optimal airfoils for airborne wind energy applications. In AIAA Science and Technology Conference (p. 1155).
- Kheiri, M., Rangriz, S., & Bourgault, F. (2024). Aerodynamic shape optimization of airfoils and wings for crosswind kites. In the 10th International Airborne Wind Energy Conference (AWEC 2024), Madrid, Spain.

1.6 Road map

The chapters in this thesis are organized as follows: Chapter 2 provides an overview of the optimization methods and the one employed in this research. Chapter 3 briefly discusses the features of the aerodynamic tools (from low- to high-fidelity) utilized within the present optimization frameworks or employed for comparison purposes. Chapter 4 presents the results from the optimization of airfoils for the use in CKPSs. Chapter 5 covers wing planform

optimization and its results. Chapter 6 focuses on the aerodynamic optimization of box-wing airfoils. Finally, Chapter 7 offers concluding remarks and outlines proposed future work.

Chapter 2

Optimization techniques

2.1 Introduction

In general, an optimization problem can be described as [50]

$$\text{Minimize} \quad f(x_i), \tag{2.1}$$

$$\text{subject to:} \quad g_j(x_i) \leq 0, \quad j = 1..p \tag{2.2}$$

$$h_k(x_i) = 0, \quad k = 1..q \tag{2.3}$$

$$x_{iL} \leq x_i \leq x_{iU}, \quad i = 1..r, \tag{2.4}$$

where x_i are design variables, $f(x_i)$ is the objective function, $g_j(x_i)$ is the inequality constraint; $h_k(x_i)$ indicates the equality constraint, and x_{iL} and x_{iU} show the lower and upper bounds of x_i, respectively. As an example, Fig.2.1 shows different constraints in the design space.

The objective function, constraints, and design variables bounds are determined based

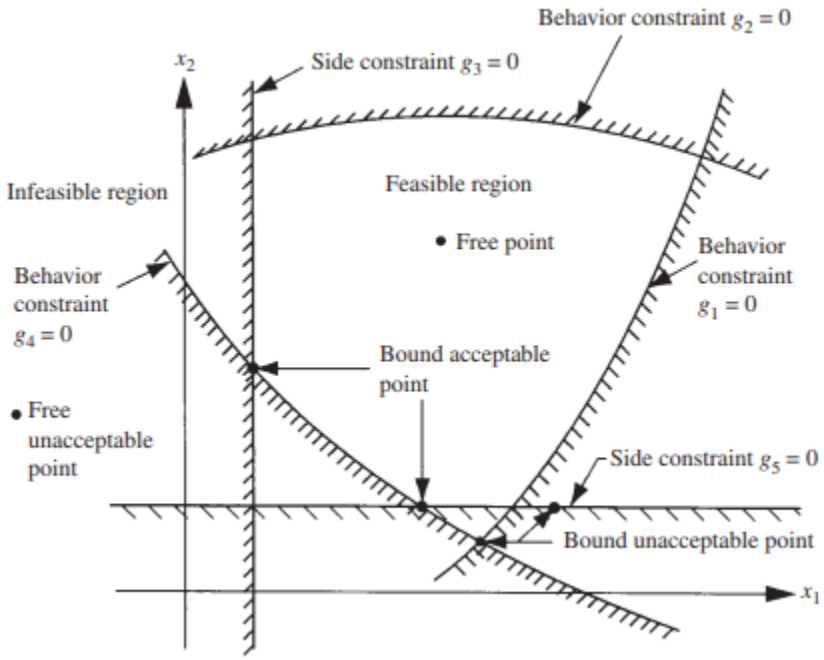

Figure 2.1: Design constraints in a hypothetical two-dimensional design space [3].

on the problem definition and also the physical or non-physical properties involved in the problem [3]. Optimization techniques tackle the problem by finding the best combination of design variables that leads to the lowest value in the objective function while ensuring that each set of solutions satisfies Eq.(2.2) to (2.4).

The optimization techniques are either traditional, in which traditional mathematical programming is used, or non-traditional, which have been developed in recent years. In recent decades, non-traditional methods have significantly influenced engineering problem solving. These techniques adopt comprehensive approaches, employing stochastic or probabilistic methods, trial-and-error approaches, heuristics, and bio-inspired algorithms mimicking natural species' behavior. Their primary goal is to find global optima efficiently. The evolution of optimization methods was slow before the advancement of computers and computer resources. After that, non-traditional methods were developed that possess an iterative nature such as genetic algorithms, particle swarm optimization, simulated annealing, ant colony

optimization, neural network optimization, and fuzzy optimization, to name a few.

Local and global optimization techniques are utilized in many applications in engineering. Most of the local optimization techniques are built upon gradient-based methods. However, these algorithms come with several limitations. These include their tendency to identify local optima, challenges in tackling discrete optimization problems, difficult implementation due to the complex nature of optimization problems which make them less efficient, and susceptibility of the answer to numerical errors.

On the other hand, global optimization techniques can find global or near-global solutions where the issues of local optimization techniques have been resolved. These techniques can be classified as deterministic and evolutionary algorithms.

Another classification is single objective and multi-objective optimization techniques. In practice, numerous problems require compromising between objectives simultaneously, emphasizing the importance of multi-objective optimization development. This lets the decision-maker select the solutions that satisfy the requirements set by the design purposes. Non-sorting genetic algorithm II (NSGA-II) and particle swarm optimization are two widely used multi-objective techniques implemented for solving engineering problems, particularly in wind energy.

For example, Ma et al.,[51] explored the optimization process involved in designing turbine blades. They employed Particle Swarm Optimization combined with the FAST solver, an open-source tool used to analyze the dynamic response of offshore horizontal-axis wind turbines. The focus of the study was on investigating the impact of wave and period of the fluctuation in power output of wind turbines while aiming to enhance the blade design through optimization.

Furthermore, the minimization of mass and cost is performed in [52] where aiming for a more efficient small-scale wind turbine. An integrated framework was developed in which

structural constraints such as stress, strain, deformation, and natural frequency of the blade were introduced in the NSGA-II method. In this Fluid-Structure Interaction study the aerodynamic aspect and composite structure of the blades were studied.

Other optimization methods were widely used in the wind energy industry. For instance, Yang and Cho [53] investigated the effect of wind turbine farm layout on wind farm performance. The study considered various layouts to minimize the wake effect and turbulence imposed by upstream wind turbines on downstream turbines, thereby reducing fatigue loads. The simulated annealing algorithm was implemented to minimize the ratio of the total cost over the total energy output of the farm.

Generally, most of the optimization problems available in the literature for crosswind kite power systems concern the optimal control of such systems to hold the kite on a fixed trajectory, along with aerodynamic optimization to maximize the aerodynamic efficiency of the kite. As an example, Bauer et al. [30] studied the performance of small- and large-scale kites with high aerodynamic forces in which multi-element airfoils were positioned in monoplane and biplane configurations. The optimization section has been completed by evaluating a fixed design of a large-scale kite and maximizing the fraction of the allowed investment cost, development cost profit margin, and the kite's surface area at the fixed design point with the Covariance Matrix Adaptation Evolution Algorithm method.

2.2 Non-dominated sorting genetic algorithm II (NSGA-II)

NSGA-II is categorized as one of the evolutionary algorithms. Although NSGA-I can handle a multi-objective problem, the computational complexity of the method prohibits its use for a large population. In addition, solutions with the best score were lost in the next generations which adds up to the convergence time. Furthermore, a sharing parameter needs to be adjusted in NSGA-I to preserve the diversity among the population.

To resolve these problems, NSGA-II was developed by Deb et al. [4]. Losing feasible solutions and computational complexity of the NSGA-I are resolved by introducing a fast non-dominated sorting algorithm. The complexity of the computations is reduced by the order of the population size.

NSGA-II selects individuals front-wise, which means solutions are grouped into different fronts based on their domination count. A front is a set of solutions where no solution dominates any other. The front-wise approach will lead to a situation where one of the fronts needs to be split, then the crowding distance will decide the selection of the solutions. Crowding distance is a measure that indicates the proximity of a solution to its neighbors in the fitness space. The extreme points of the front are assigned a crowding distance of infinity to ensure that they are always selected.

In NSGA-II, two values are calculated for every solution: 1) The number of solutions that outperform the solution p, or the domination count n_p; 2) A set of solutions that the solution p outperforms, or S_p. Finding solutions with $n_p = 0$ and placing them in the non-dominated front is the basis for this sorting. The next step would be to visit the set S_p that is part of the foremost front and to reduce each member's n_p by 1. That solution is part of the next non-dominated front if n_p goes to zero. When every front is identified, this process is

complete.

The crowded-comparison approach would ensure diversity, eliminating the difficulties seen by the sharing parameter approach. The crowded-comparison approach needs two steps:

a) The average distance examines density estimation, called the crowding distance, of two points on either side of the i-th solution as shown in Fig.2.2. b)The Crowded-Comparison Operator is used to ensure that the selection process will be toward the region in which the population has a better rank or the lower population density. To examine that, two values are calculated, non-domination rank, which is the front that the individual belongs to, and crowding distance. The individual with a lower, i.e., better, rank is selected. If both solutions are from the same rank, then the solution located in a lower-density region is selected.

The main loop of NSGA-II initially starts with a random parent population P_0. Applying non-dominating sorting, this population is sorted in the first place. After the ranks of the individuals in P_0 are obtained, the child will be produced. To produce the child generation, i.e. Q_t, from the parent generation, i.e., P_t, binary tournament selection, recombination, and mutation operations are done. Next, the parent population and child population are combined to create a set, $R_t = P_t \cup Q_t$. Again, this set is sorted based on non-domination sorting. This procedure continues until the last non-dominated set cannot be found. Finally, the last set will be sorted and the best of the solutions will be selected as the final members

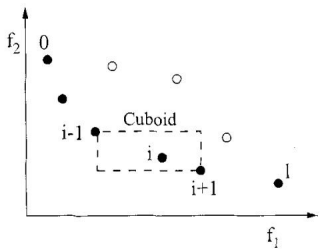

Figure 2.2: Crowding-distance of the ith solution [4].

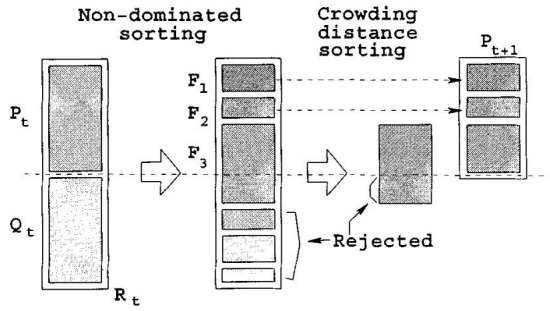

Figure 2.3: NSGA-II procedure [4].

of the Pareto optimal front. The NSGA-II procedure has been illustrated in Fig. 2.3. In this study, two definitions are important for setting the correct NSGA-II parameters: the definition of crossover and mutation. These parameters can control the optimizer's behavior.

2.2.1 Crossover

In NSGA-II, the crossover is the process of creating new offspring solutions by combining the genetic chromosomes of two parent solutions. In the genetic algorithm framework, which serves as the foundation for NSGA-II, this is an essential stage for exploring the solution space and possibly, discovering superior solutions.

Crossover is utilized in the NSGA-II framework to produce new individuals that inherit characteristics from their parents. The goal of this procedure is to increase population diversity and potentially enhance the solutions that are discovered. Depending on the nature of the problem and the features of the solutions, different crossover types may be employed. For example, in problems with binary decision variables, a common crossover technique is the two-point crossover, where a point is selected in the parent solutions, and the genetic information between these points is swapped to create the offspring.

In practice, implementing crossover in NSGA-II involves with selecting pairs of parent solutions and applying the crossover operator to them. This can be done using various

operators, such as the two-point crossover for binary variables. The choice of crossover operator and its parameters can significantly impact the performance of the algorithm, so it is important to choose an operator that is well-suited to the problem at hand.

The Crossover index refers to the non-negative parameter and determines the probability of creating offspring near the parents. This parameter was introduced in the simulated binary crossover method [54].

2.2.2 Mutation

Subsequently, after the implementation of crossover, to get better fitness values for the next generation, the mutation operator will work on the new generation to change them according to the mutation probability value specified by the user [3].

Through small and random alterations to each individual's genetic chromosomes, the mutation in genetic algorithms adds variety to the population. This approach is crucial to explore the search space and prevent early convergence to poor answers. To improve the algorithm's capacity to identify global optima, the mutation operator is engineered to preserve variety and explore deeper into the search space.

The mutation probability utilized in this study shows the probability of a single individual undergoing a mutation process. This value should be selected carefully since it can determine how the next generation would vary in its neighborhood. An unrealistically high value would perturb the population that will go far from suitable convergence [3].

Chapter 3

Aerodynamic Tools

3.1 Introduction

Aerodynamic solvers are used to simulate the behavior of fluid flows around objects. These solvers are categorized as high- and low-fidelity, where the governing equations employed in high- and low-fidelity solvers are simplified Navier-Stokes (N-S) equations. The assumptions for obtaining the simplified version of N-S equations determine part of the computational cost of each solver. For example, in the Euler equation, the fluid has no viscosity, or in the Stokes equation the flow is incompressible and the inertial term is negligible.

Another factor that determines the computational cost is the numerical scheme involved in the N-S equations discretization. However, this topic is beyond the scope of this thesis and will not be pursued further.

The importance of aerodynamic solvers lies in their ability to predict the performance of aerodynamic objects, such as wings, kites, airfoils, and wind turbine blades in terms of aerodynamic parameters like lift, drag, and pitching moment. These solvers provide detailed insights into the aerodynamic behavior of such objects and aid designers in modifying their

designs to achieve the desired efficiency.

In this section, the aerodynamic tools used to obtain aerodynamic lift and drag coefficients of airfoils and wings in the present work, as part of the optimization process, are discussed. Two primary features of these tools include being computationally fast and being integrated with other tools in optimization frameworks. Low-fidelity solvers are part of the optimization framework while computational fluid dynamic (CFD) simulations are utilized for verification and comparison purposes.

A brief description of each solver's capability and their validation and verification studies are presented in this chapter.

3.2 XFOIL

An interactive tool called XFOIL is used to aerodynamically analyze airfoils. Mark Drela created XFOIL in the 1980s for the MIT Daedalus project. Implementing the accuracy and high speed of a high-order panel method and the full inviscid/viscous interaction, which was used in Drela and Giles's two-dimensional viscous aerodynamic design and analysis code, in the same code, was the main purpose of XFOIL development. In December 2013, the most recent version, 6.99, was made available. XFOIL is still a commonly used tool in the field of aerodynamics and aircraft design, despite its antiquity.

The program operates by taking the coordinates specifying the shape of a 2D airfoil, along with Reynolds and Mach numbers, to calculate the pressure distribution over the airfoil. This information is then used to determine lift and drag characteristics and is shown with pressure distribution in a Graphical User interface (GUI); see, for example, Fig.3.1. XFOIL also supports inverse design, allowing the program to modify an airfoil's shape to achieve desired parameters. This capability is vastly used in gradient-based optimization

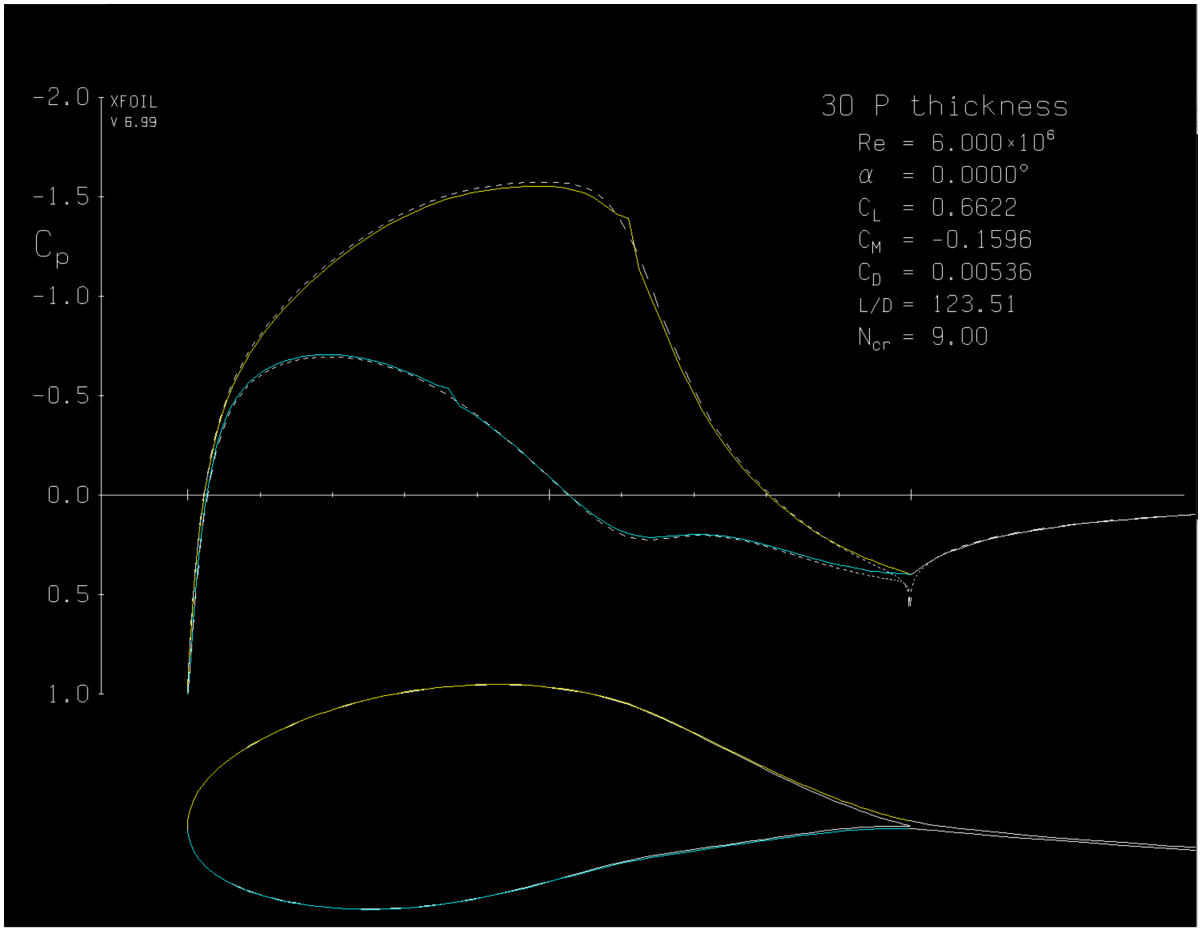

Figure 3.1: The GUI of XFOIL, showing a typical airfoil profile and the corresponding pressure distribution obtained from the present study optimization.

problems in the Aerospace industry.

One of the key features of XFOIL is its ability to perform viscous and inviscid analyses of existing airfoils. This includes examining forced or free transition, transitional separation bubbles, limited trailing edge separation, and lift and drag predictions where separation is not significant. In addition, it supports the Karman-Tsien compressibility correction for fixed or varying Reynolds or Mach numbers.

With the use of interactive surface speed distribution modification, XFOIL provides two ways for designing and redesigning airfoils: the Full-Inverse approach, which is based on

a complex mapping formulation, and the Mixed-Inverse method, which is an expansion of XFOIL's fundamental panel method. These techniques are especially helpful for multi-point design and redesign issues where there is no way to change some elements of the airfoil.

The software also facilitates redesign by allowing interactive specification of geometric parameters, such as maximum thickness and camber, leading-edge radius, trailing-edge thickness, camber line via geometry specification or loading change specification, and explicit contour geometry. This level of interactivity makes XFOIL a powerful tool for airfoil analysis and redesign.

XFOIL supports batch execution for long calculations, making it convenient for running calculations or interacting with it for optimization purposes. It also provides tools for writing and reading airfoil coordinates and polar save files, enabling efficient data management and analysis. For visualization, XFOIL includes tools for plotting airfoil geometry, pressure distributions, and polar, using a Versaplot-derivative plot package [55, 56].

XFOIL's verification and validation are available in the literature, and more and more studies are performed on this subject; thus, they are not repeated here.

3.3 OpenVSP

3.3.1 Description

Open Vehicle Sketch Pad (OpenVSP) is an open-source parametric aircraft geometry tool originally developed by NASA. It enables the users to create 3D models of aircraft defined by common engineering parameters, which can then be processed into formats suitable for engineering analysis.

OpenVSP is designed to quickly generate computer models from ideas, making it particularly powerful for generating and evaluating unconventional design concepts. It offers

various basic geometries common to aircraft modeling, such as wings, pods, fuselages, and propellers, as well as advanced components like bodies of revolution and conformal geometries. All the designs can be modified and assembled to create a complete model of aircraft or aerial apparatus.

In addition to the geometry modeler, OpenVSP includes multiple tools for the aerodynamic or structural analysis of models. These tools include CompGeom for mesh generation, Mass Properties Analysis for computing properties like the center of gravity and moment of inertia, Projected Area Analysis for computing projected area, Computational Fluid Dynamics (CFD) Mesh, and Finite Element Analysis (FEA) Mesh for generating meshes for CFD and FEA analysis software, respectively, DegenGeom for generating simplified representations of geometry models, VSPAERO for vortex lattice or panel method-based aerodynamic and flight dynamic analysis, wave drag analysis for estimating wave drag, parasite drag analysis for estimating parasite drag based on parameters like wetted area and skin friction coefficient, Surface fitting for fitting a parametric surface to a point cloud, and finally, texture manager for applying image textures to geometry for aiding visualization.

OpenVSP provides a GUI upon launch, featuring a workspace window and a geometry browser where individual components can be tracked down. These components can be selected, added, or deleted, similar to a feature tree in CAD software. OpenVSP also offers Application Programming Interface (API) capabilities, which can be accessed using Matlab, Python, or AngelScript. In this study, the Matlab API has been utilized to build the wing model and accomplish the wing platform study. The GUI of OpenVSP is shown in Fig. 3.2.

In addition, OpenVSP supports the import of multiple geometry formats like STL, CART3D (.tri), and PLOT3D, as well as point clouds for fitting a parametric surface. Geometry created in OpenVSP can be exported in various formats, including STL, CART3D (.tri), PLOT3D, STEP, IGES, OBJ, SVG, DXF, and X3D, allowing for mesh generation and

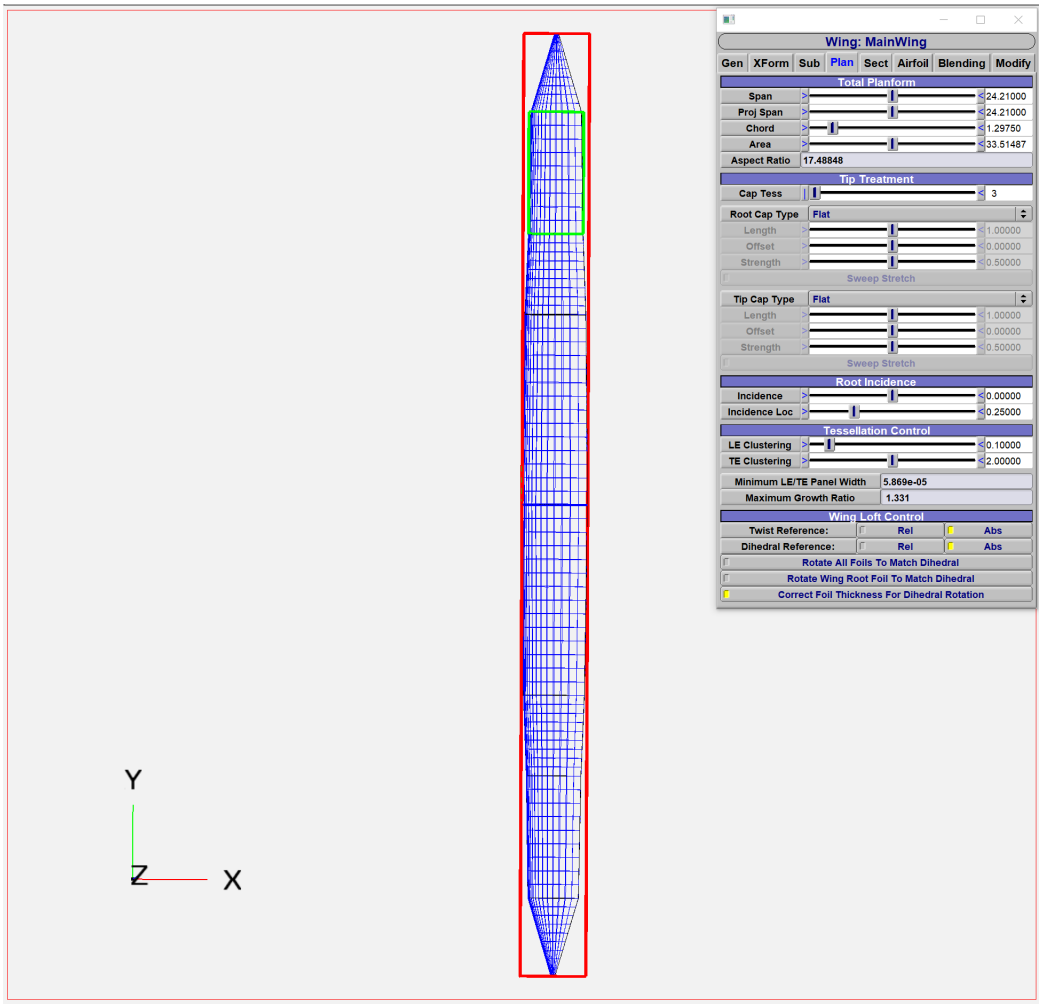

Figure 3.2: GUI of OPENVSP shows the wing provided from verification study with the $AR = 17.45$

use in CFD or FEA software.

The potential flow aerodynamic solver, VSPAERO has been implemented to analyze the wings created in the optimization problem.

3.3.2 Validation

The validation of VSPAERO is performed by evaluating its computational predictions against existing experimental data available in the literature. The validation aims to examine the

accuracy and reliability of VSPAERO for wing lift and drag predictions. VSPAERO offers two methods, namely the vortex lattice method (VLM) and the panel method to obtain the necessary aerodynamic data.

The experimental data were taken from the report to examine the effect of scale and turbulence on the wing characteristics [5]. The wing, which is characterized as a rectangular planform with a chord and span length of 5 and 30 inches, is held in a variable density wind tunnel where the Reynolds number is $Re = 3.46 \times 10^6$ while the airfoil section is Clark-Y. Interested readers are referred to this study. This wing is modeled in the OPENVSP and aerodynamic results are obtained using VSPAERO for validation purposes.

Figure 3.3 presents the lift and drag coefficient variations as a function of the angle of attack. While the lift coefficient variation is generally in good agreement with the experimental data, discrepancies are observed in the drag coefficient predictions. These discrepancies occur when VSPAERO employs VLM, which is known for its limitations in accurately predicting drag in VSPAERO. The decision to use VLM was driven by the need to minimize computational costs, as more detailed methods like panel methods are computationally intensive, especially in optimization frameworks. This approach offers a balance between computational efficiency and the accuracy of aerodynamic predictions.

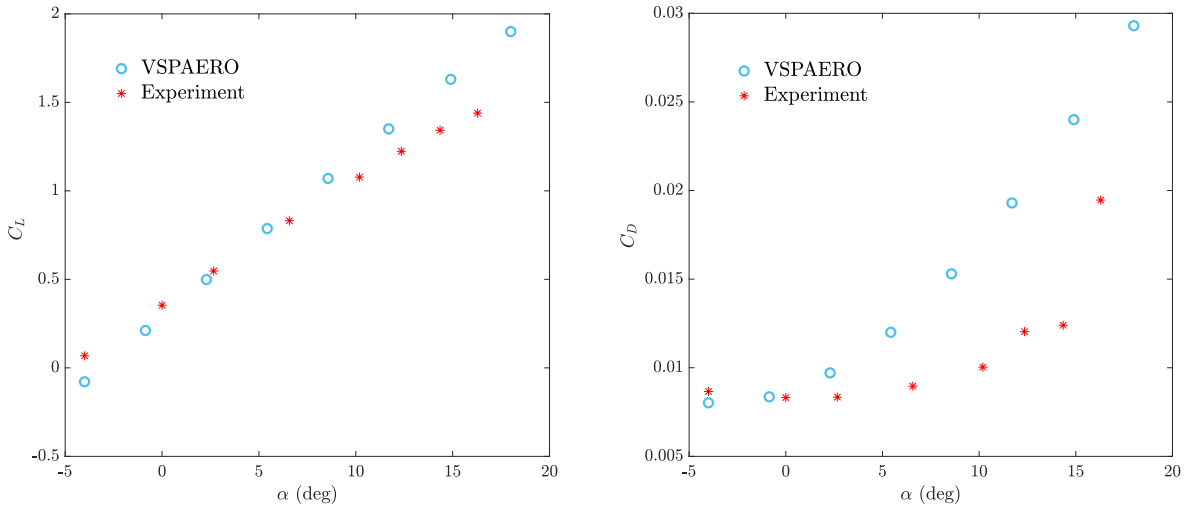

(a) (b)

Figure 3.3: (a) Lift, (b) drag coefficient versus angle of attack obtained from VSPAERO and the experimental results available in [5].

3.4 MSES

MSES (Multi-element Surface Evolution System) is a comprehensive software suite designed for the analysis and design of multi-element airfoils. It is a member of the larger MSES family of programs created at the MIT Department of Aeronautics and Astronautics by Mark Drela. The MSES suite, which includes the analysis of flow solutions, the modification of airfoil shape, and the optimization of airfoil designs, is specially made for the study of aerodynamics in airfoils [6]. The governing equation is the conservative Euler equation.

The programs are divided into two categories: primary and supporting programs. The three primary programs are MPLOT, MSES, and MSET. Additional programs that are regarded as supporting programs include PPLOT, LINDOP, MPOLAR, AIRSET, EDP, and MPOLAR. A brief description of each program will be presented here.

3.4.1 Primary programs

- **MSET:** This program reads the airfoil coordinate file and generates the initial grid. It is the starting point for the analysis process, setting up the computational domain based on the airfoil geometry provided.

- **MSES:** The core of the MSES suite, this program calculates the flow solution around the airfoil. It uses the initial grid generated by MSET to solve the aerodynamic flow equations, providing detailed information about the flow characteristics around the airfoil.

- **MPLOT:** This program is used to plot the flow solution generated by MSES. It visualizes the flow patterns, pressure distributions, and other relevant data, aiding in the interpretation of the aerodynamic performance of the airfoil.

3.4.2 Supporting programs

- **AIRSET:** A tool for examining and manipulating multi-element airfoil geometry. It allows users to adjust the geometry of the airfoil and outputs an airfoil file suitable for grid initialization in MSET.
- **EDP:** A visual editor for specified surface pressure distributions, which are input for inverse design calculations in MSES. This program facilitates the design of airfoils by allowing users to manipulate pressure distributions and observe the resulting aerodynamic effects.
- **MPOLAR:** Similar to MSES, it sweeps over a range of specified parameter values to analyze the effects of varying these parameters on the airfoil's performance. This is particularly useful for sensitivity analysis and optimization.
- **PPLOT:** This program plots the results of MPOLAR in standard drag-polar form. It provides a visual representation of the aerodynamic performance across a range of conditions.
- **LINDOP:** Combines the parameter-sensitivity output from MSES to perform single-point or multi-point airfoil optimization. It allows for the optimization of airfoil designs based on a variety of built-in or user-specified objective functions and constraints.

The summary of the programs, data files, and the connection between the primary and supporting programs are shown in Fig. 3.4.

3.4.3 Verification and validation

This section presents verification and validation studies for MSES. The verification is carried out using the CFD results presented in [7]. The CFD framework developed in [7] was

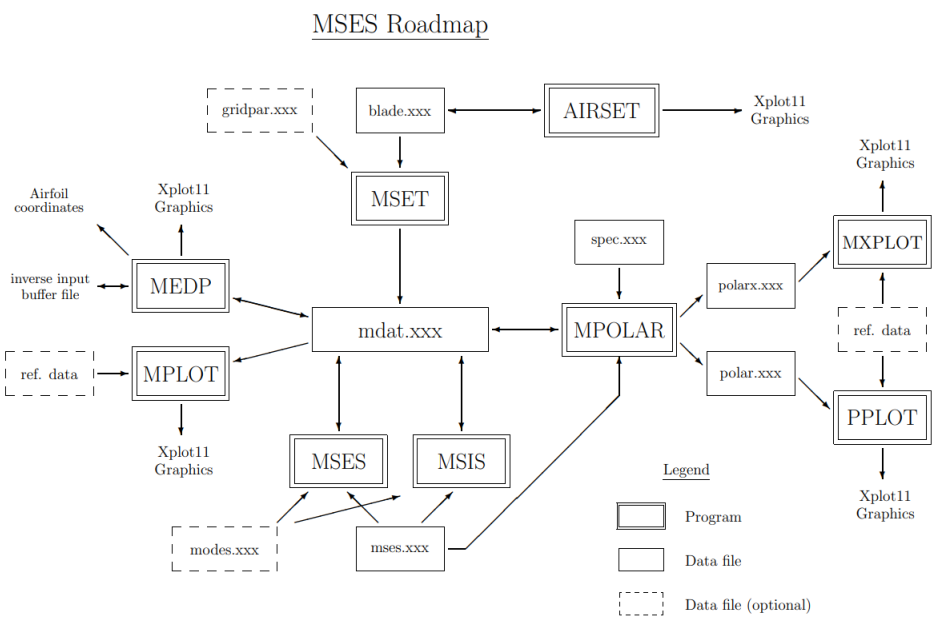

Figure 3.4: A diagram showing primary and supporting programs with necessary input files [6].

validated against experimental data. In order to reach higher altitudes, the study examined novel aircraft designs for improving aerodynamic efficiency, particularly at moderate Reynolds numbers. To increase the lift-to-drag ratio, closed-coupled biplanes were considered, where the geometric properties of biplanes such as stagger-to-chord and gap-to-chord ratio were modified.

The case considered for verification, as shown in Fig.3.5, is a "close-coupled" biplane with a gap-to-chord ratio of 0.5 and a stagger-to-chord ratio of 0.9. The Reynolds number is $Re = 3 \times 10^6$ in which the characteristic length is the chord length of the upper airfoil. In addition, the chord ratio between the upper and lower chord lengths is set to 2, which means that the upper airfoil has the chord length twice as the lower airfoil. Fig. 3.6a shows the variation of the lift coefficient as a function of angle of attack. As seen, the results from MSES are in good agreement with CFD results from [7] – the maximum relative error is about 8%, which is acceptable for optimization and preliminary design. Figure 3.6b shows

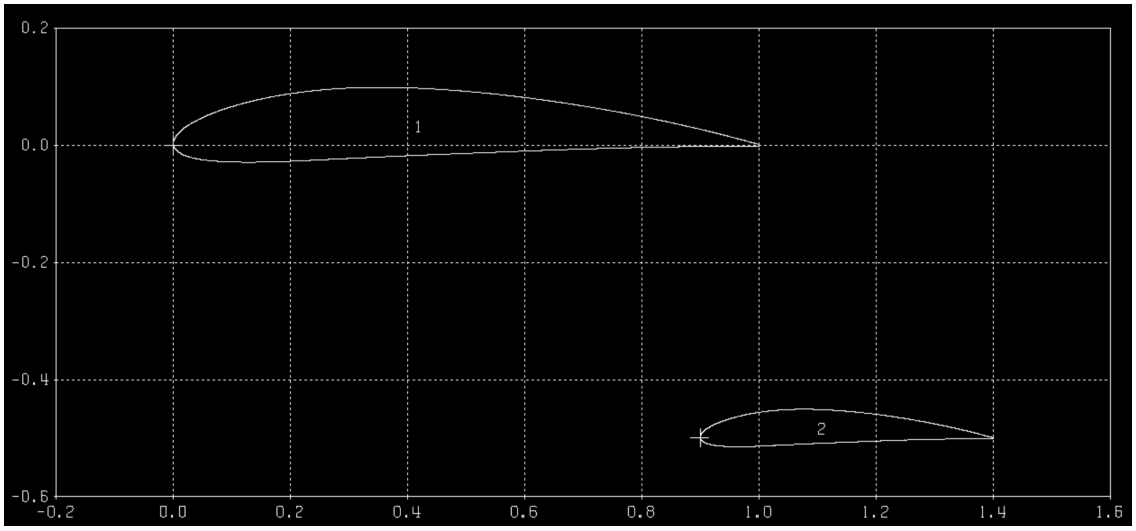

Figure 3.5: Selected case of the boxwing for verification study with a gap-to-chord ratio of 0.5 and stagger-to-chord ratio of 0.9 available in this study [7].

the variation of the drag coefficient as a function of the angle of attack. As seen, in this case, the agreement between MSES and CFD results is poor, with MSES underestimating the drag. Similar observations were reported in [42] and [57].

For the validation, the experimental results presented in [8] are used, where a biplane configuration with a gap-to-chord ratio of 0.025 and a stagger-to-chord ratio of 1 was considered. The Reynolds number was $Re = 4.1 \times 10^6$ in which the chord length of the forward wing is utilized as the characteristic length.

The comparison of the lift coefficient variation as a function of the angle of attack between MSES and the experiment is presented in Fig. 3.7a. A good agreement is observed between the two sets, where the maximum relative error is 12%. On the other hand, Fig. 3.7b shows the drag polars obtained numerically from MSES and experimentally. As seen, the agreement is not as good as that for the lift coefficient. For a given lift coefficient, MSES underestimates the drag coefficient. Interestingly, the difference between MSES and experimental results decreases as the lift coefficient (or the angle of attack) is increased.

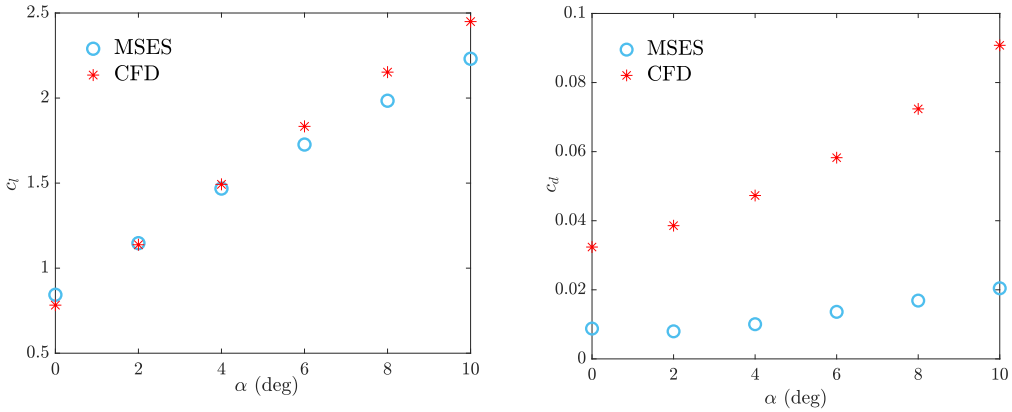

(a) (b)

Figure 3.6: Variation of (a) lift coefficient as a function of angle of attack, and (b) drag coefficient as a function of angle of attack for the configuration with a gap-to-chord ratio of 0.5 and a stagger-to-chord ratio of 0.9. The CFD results are taken from [7].

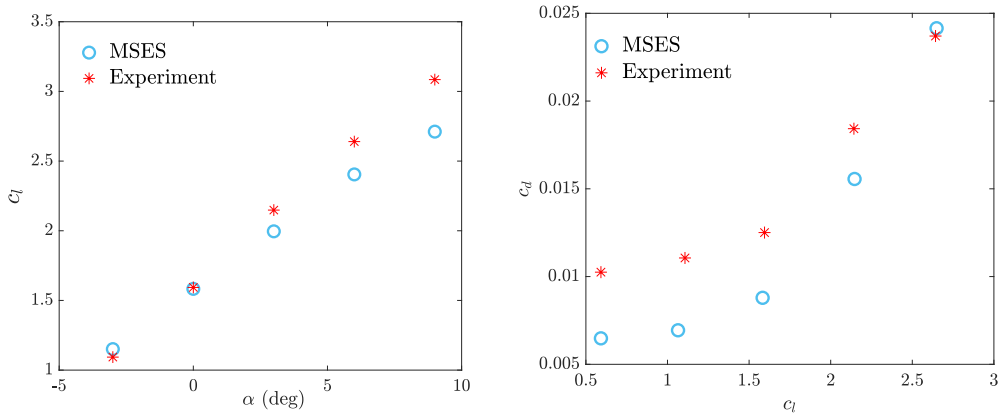

(a) (b)

Figure 3.7: Variation of (a) lift coefficient as a function of angle of attack, and (b) drag coefficient as a function of lift coefficient for the configuration with the gap-to-chord ratio of 0.025 and stagger-to-chord ratio of 1. The experimental results are available in [8].

From the results presented in this section, one may conclude that using MSES, the lift coefficient of a 2-D biplane can be obtained with reasonable accuracy while MSES predictions of the drag coefficient are generally inaccurate, and thus, the results should be taken with a grain of salt.

3.5 Computational Fluid Dynamics (CFD)

3.5.1 CFD simulation setup

In the present thesis, two-dimensional Reynolds-averaged Navier-Stokes (RANS) equations [58] for compressible flows are solved computationally. The purpose of these simulations is to verify the aerodynamic results obtained via XFOIL for the optimal airfoils (see Chapter 4). The equations for the conservation of mass and that of the linear momentum are written as follows, where the parameters with overbar and tilde are time-averaged and density-weighted averaged, respectively:

$$\frac{\partial \overline{\rho}}{\partial t} + \frac{\partial (\overline{\rho}\widetilde{u_i})}{\partial x_i} = 0, \tag{3.1}$$

$$\frac{\partial (\overline{\rho}\widetilde{u_i})}{\partial t} + \frac{\partial (\widetilde{u_j}\overline{\rho}\widetilde{u_i})}{\partial x_j} = -\frac{\partial p}{\partial x_i} + \frac{\partial \bar{t}_{ij}}{\partial x_j} + \frac{\partial (\overline{\rho}\tau_{ij})}{\partial x_j}, \tag{3.2}$$

where $\widetilde{u_i}$ $(i = 1, 2)$ are the mean (or mass-averaged or Favre-averaged) flow velocity components in the x_i direction; ρ and p represent the fluid flow density and pressure; t denotes time, and μ represents the dynamic viscosity; τ_{ij} represents the specific Reynolds stress tensor which is symmetric and adds six unknowns as a result of Reynolds averaging; also, $\bar{t}_{ij}$ represents the viscous stress tensor which is written as

$$\bar{t}_{ij} = 2\mu \overline{S}_{ij}, \tag{3.3}$$

in which $\overline{S}_{ij}$ denotes the mean strain rate tensor and is given as:

$$\overline{S}_{ij} = S_{ij} - \frac{1}{3}\frac{\partial \widetilde{u}_k}{\partial x_k}\delta_{ij}, \tag{3.4}$$

with δ_{ij} being Kronecker's delta.

Furthermore, $\overline{\rho}\tau_{ij}$ can be obtained as:

$$\overline{\rho}\tau_{ij} = 2\mu_T \overline{S}_{ij} - \frac{2}{3}\overline{\rho}k\delta_{ij} \tag{3.5}$$

where μ_T and k are the eddy viscosity and turbulent kinetic energy terms in the RANS equation.

The present study simulations were performed using a RANS flow solver in Ansys Fluent, closed by Menter's [59] shear-stress transport (SST) turbulence model, commonly known as the $k-\omega$ SST turbulence model. Menter's [59] model uses the modified form of Wilcox's [60] turbulence model (i.e., the standard $k-\omega$ model) in the inner region of the boundary layer while it switches to the standard $k-\epsilon$ model in the outer region of the flow. Compared to other turbulence models, the $k-\omega$ SST turbulence model has widely been used (e.g., [61–64]) for CFD simulation of wind turbines as it performs reasonably well in predicting adverse pressure gradient flows which typically occur over the blades of wind turbines.

To minimize the computational run-time, in the present study, the steady-state flow analysis is adopted. The coupled algorithm is selected for the pressure-velocity coupling. The spatial discretization is set to the second-order upwind scheme. The solution convergence is ensured by monitoring the residuals in the continuity, momentum, and energy (k and ω) equations, all set at 10^{-6}, as well as axial and normal force coefficients, set at 10^{-7} and 10^{-6}, respectively.

Figure 3.8 shows the two-dimensional simulation domain. A C-shape domain with a radius of $20c$ (c being the chord length of the airfoil) is created upstream of the airfoil while a rectangular domain with $20c \times 40c$ (length $\times$ width) is created its downstream. The flow inlet includes the C-shape portion and the upper and lower sides while the outlet of the domain is the right side of the domain. Also, the airfoil profile has been considered as wall

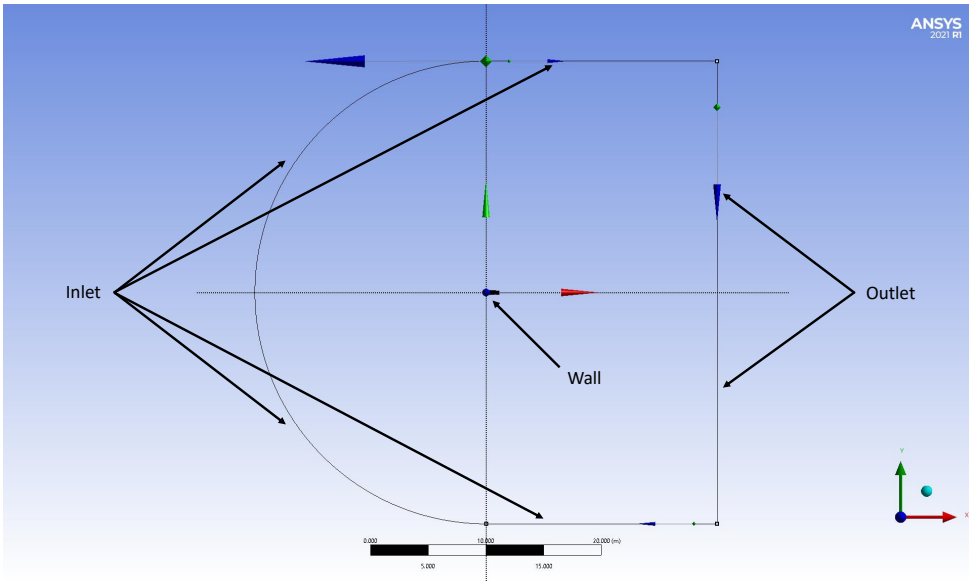

Figure 3.8: Schematic of the two-dimensional solution domain showing the airfoil, and the inlet and outlet of the flow domain.

with the no-slip boundary condition.

3.5.2 Grid convergence study

When performing CFD simulations, a mesh convergence study is essential for determining the number of cells required for a solution with acceptable accuracy. The error will reduce as the mesh is refined for a consistent CFD scheme. However, this will be at the expense of increasing computational cost. Hence, a reasonable number of cells is to be chosen for the desired accuracy.

The flow parameters around an object of interest are influenced by the gradients presented in the NS equations. It has been observed from experiments and CFD simulations that, for airfoils in subsonic flows, high-gradient regions are close to the leading edge and trailing edge. In other words, there will be a sharp change in pressure and shear stress on the airfoil surface in these regions. On the other hand, the changes over the middle part of the

airfoil will be comparatively less. Thus, each side of airfoil's profile is divided into three segments: leading-edge, middle, and trailing-edge segments. This allows for independent mesh refinement over each segment. The mesh is to be refined, particularly over the leading- and trailing-edge segments, to achieve better results. This is achieved by creating more divisions in the respective segments and also by implementing bias factors. Bias factors ensure the generation of approximately similar cell sizes when the transition happens from the leading edge toward the middle of the airfoil and from there toward the trailing edge and from the surface of the airfoil toward computation boundaries, i.e., inlet and outlet. In the present study, a bias factor of 10^5 has been adopted for the second application. In addition to the refinement over the leading- and trailing-edge segments, the wake region downstream of the airfoil is also refined. This is particularly crucial for accurate computation of the drag coefficient. In addition, since the $k-\omega$ SST turbulence model is adopted when generating the mesh, it was always ensured that $y^+ < 1$ using the bias factor value mentioned above.

Following the mesh generation strategy discussed above, six structured meshes, called Mesh 0 to Mesh 5, were created in Ansys Fluent, for a typical airfoil obtained from the present optimization study (the optimal airfoil in Sec. 4.2.2 with $\tau_{max} = 20\%$ and assuming $AR = 12$). Figure 3.8 shows 4 snapshots taken from each mesh. The snapshots show the entire simulation domain, the region in the vicinity of the airfoil, and the regions close to the leading and trailing edges. As observed, moving from Mesh 0 to Mesh 5, the mesh is refined, primarily around the leading and trailing edges as well as in the wake region. This refinement is expected to improve the accuracy of the numerical results but will also result in the overall increase of the total number of cells and thus increased computational cost. Table 3.1 gives the total number of quadrilateral cells for each mesh. To assess these meshes, simulations were performed at $Re = 6 \times 10^6$ at three angles of attack α = -5, 0 and 5 deg, and the lift and drag coefficients were obtained. Figure 3.9 shows the variation of c_l and c_d

as the mesh is refined. Also, Table 3.2 gives the numerical values. As seen, c_l and c_d values are generally sensitive to the mesh refinement, particularly for $\alpha = 5$ deg. Nevertheless, by further refining the mesh beyond Mesh 3, c_l and c_d change insignificantly; the relative change in c_l and c_d between Mesh 3 and Mesh 4 (except for c_d at $\alpha = -5$ deg) is less than 1%. This confirms achieving mesh convergence, and Mesh 3 appears to be suitable for CFD simulations in the present study.

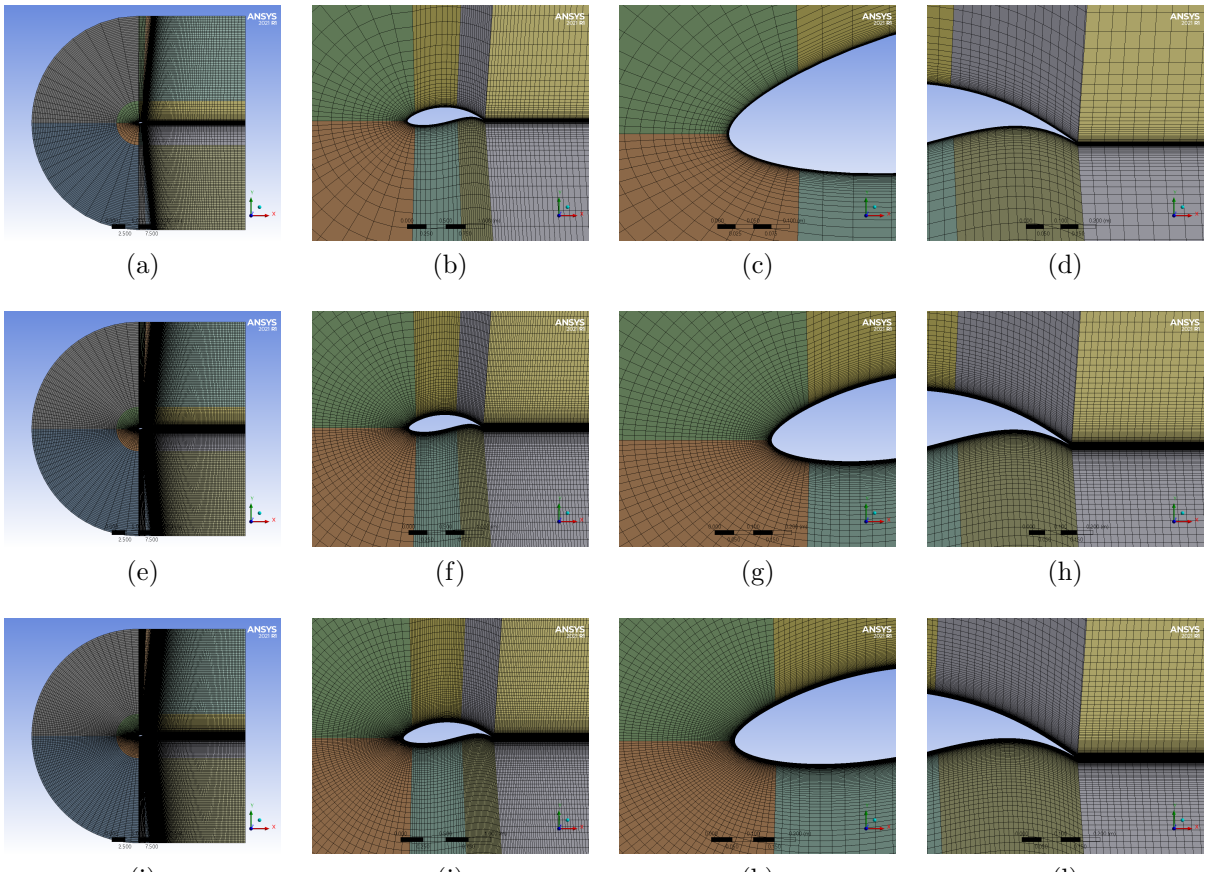

(a) (b) (c) (d)

(e) (f) (g) (h)

(i) (j) (k) (l)

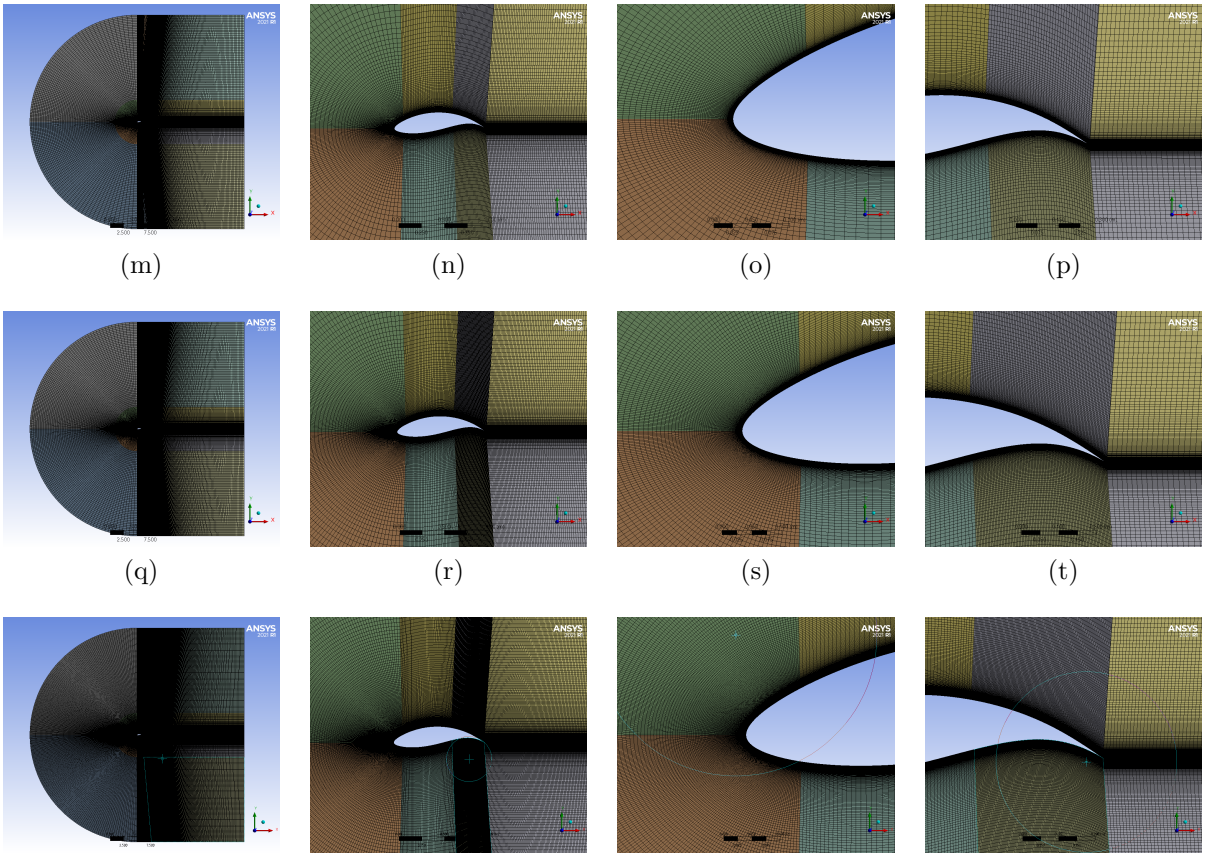

(m) (n) (o) (p)

(q) (r) (s) (t)

(u) (v) (w) (x)

Figure 3.8: Snapshots taken from six different meshes: Mesh 0 (first row) to Mesh 5 (last row). The first column shows the snapshots of the entire simulation domain, the second column shows the snapshots of the region in the vicinity of the airfoil, the third column shows the mesh in the proximity of the leading edge, and the last column the mesh in the proximity of the trailing edge.

Table 3.1: Number of cells corresponding to each mesh.

Mesh #	0	1	2	3	4	5
Number of cells	31300	86200	121725	165250	261329	585450

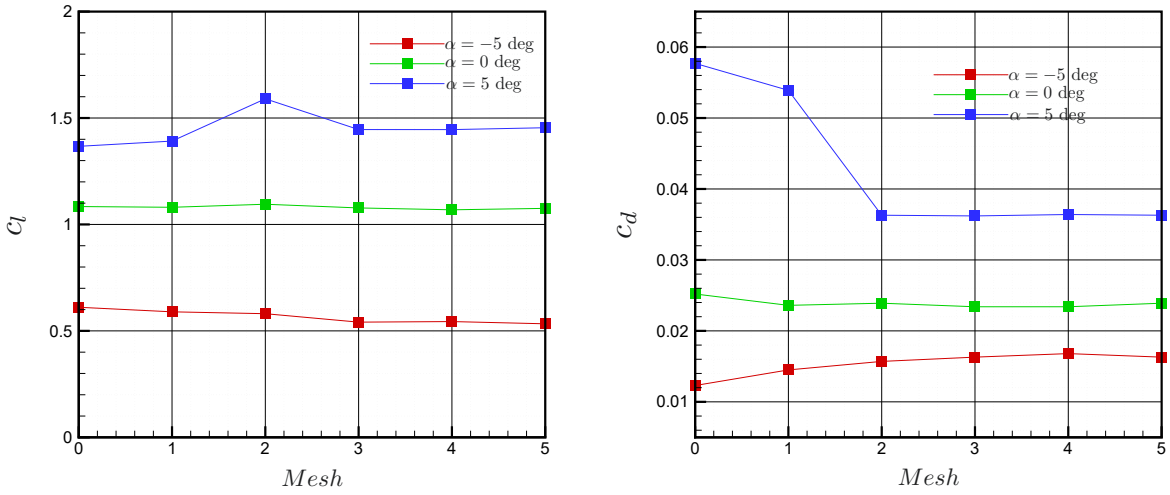

(a) (b)

Figure 3.9: Variation of (a) lift coefficient and (b) drag coefficient with respect to the mesh refinement (from Mesh 0 to Mesh 5). The numerical values of the coefficients are provided in Table 3.2.

Table 3.2: Lift and drag variations as a function of angle of attack for different meshes.

	Mesh 0		Mesh 1		Mesh 2	
α (deg)	c_l	c_d	c_l	c_d	c_l	c_d
-5	0.6110	0.0123	0.5895	0.0145	0.5808	0.0157
0	1.0841	0.0252	1.0806	0.0236	1.095	0.0239
5	1.3670	0.0577	1.3917	0.0537	1.5902	0.0363
	Mesh 3		Mesh 4		Mesh 5	
α (deg)	c_l	c_d	c_l	c_d	c_l	c_d
-5	0.5411	0.0163	0.5438	0.0168	0.5333	0.0163
0	1.0776	0.0234	1.0688	0.0234	1.0755	0.0239
5	1.4458	0.0362	1.4456	0.0364	1.4543	0.0363

3.5.3 Validation of the CFD modelling

Wind tunnel results for a supercritical airfoil [9] at $Re = 4.02 \times 10^6$ are used to validate the CFD modeling approach (including the mesh) adopted in the present study. The rationale for choosing such an airfoil is that the stall behavior and pressure distribution over the airfoils obtained from the present optimization are reminiscent of supercritical airfoils. Following the simulation set-up described in section 3.5.1 and the meshing strategy discussed in section 3.5.2, the CFD simulations are performed. Figure 3.10 shows various snapshots of the mesh, including a close-up view of the mesh in the vicinity of the leading edge. The lift and drag coefficients are obtained for a range of angle of attack between $\alpha = 0$ and $\alpha = 10$ deg with the step of 2 deg.

Figure 3.11a shows the variation of c_l versus α, obtained computationally, and the corresponding experimental data. As seen, the agreement between CFD results and experimental data is excellent. Figure 3.11b shows the variation of c_d as a function of α. As shown, the CFD results and experimental data are generally in good agreement. As the angle of attack increases, the error between CFD and experiment increases; however, they tend to remain below an acceptable threshold ($< 10\%$).

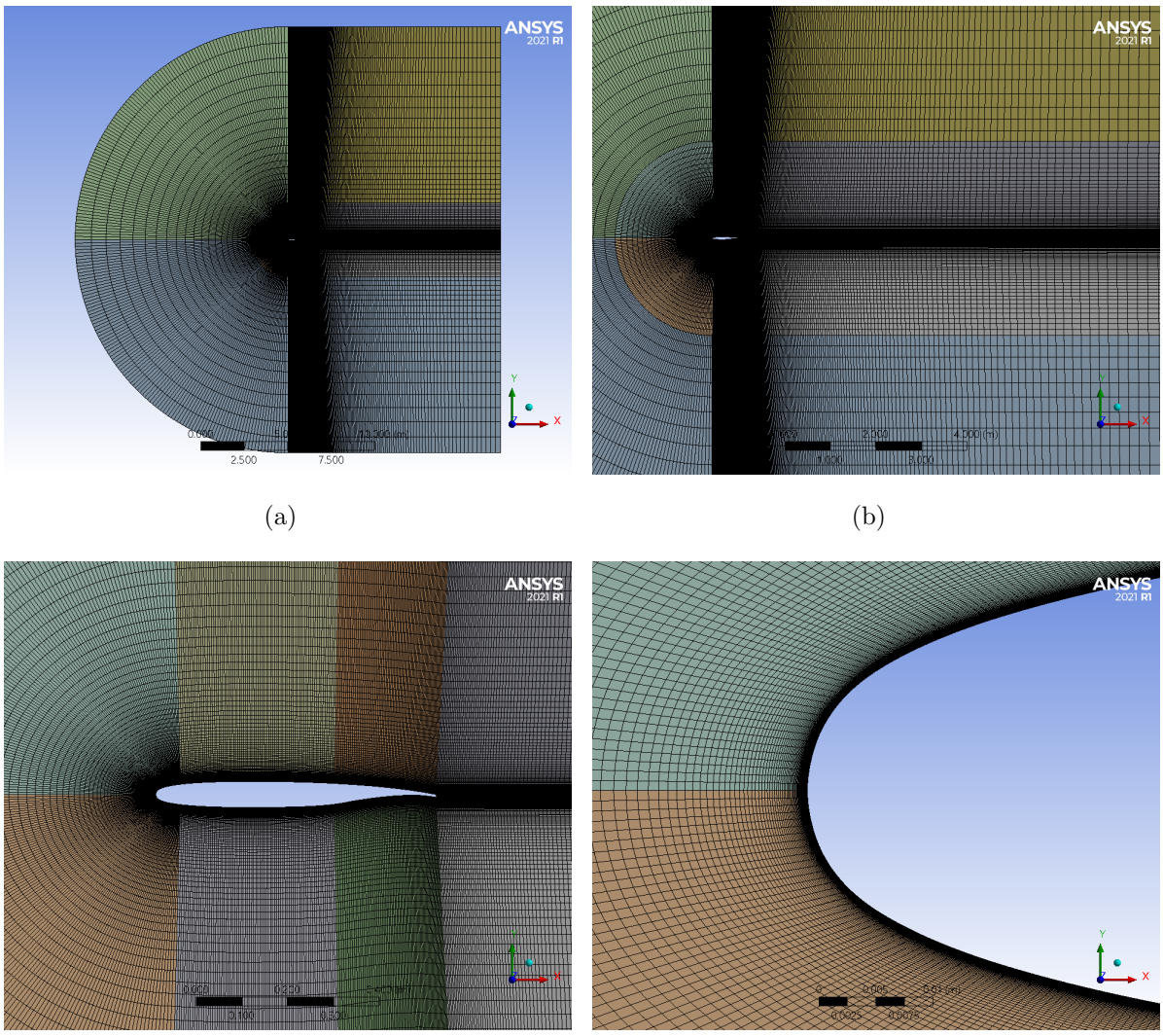

Figure 3.10: 2-D airfoil CFD simulation setup: (a) the solution domain includes a C-shape of the radius of 20 m upstream and a rectangle of the length of 20 m and width of 20 m downstream of the airfoil, (b) wake region behind the airfoil, which has been refined to capture vortex shedding from the airfoil, (c) mesh around the airfoil section (supercritical airfoil in study [9], chord: 1.0 m, Max. thickness: 0.20 m), and (d) a close-up view showing the boundary layer mesh close to the leading edge (Bias factor:10^5).

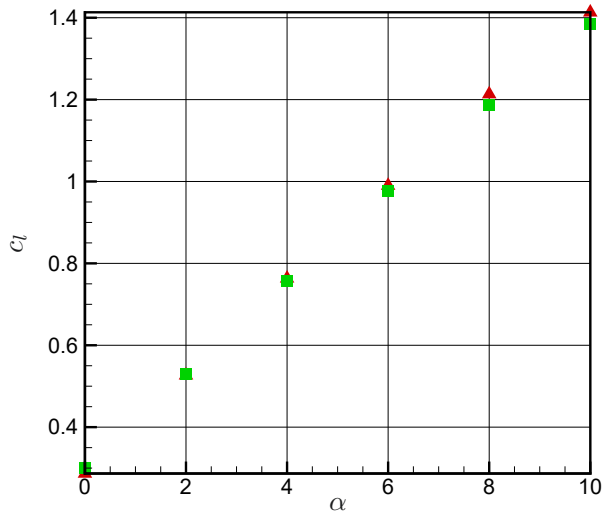

(a)

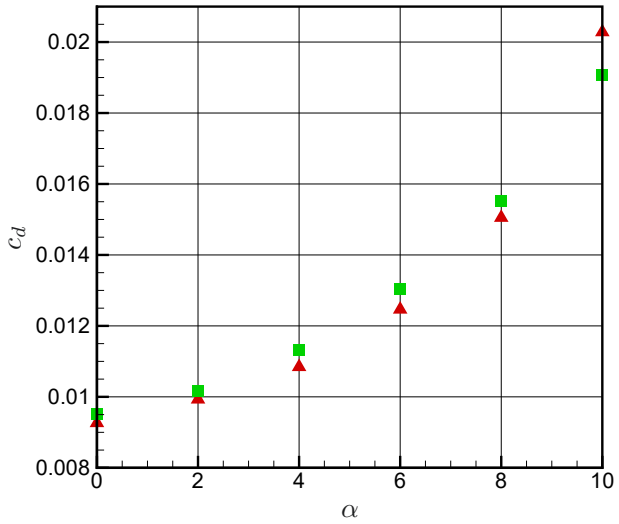

(b)

Figure 3.11: Comparison between CFD and experimental results for the supercritical airfoil (Figure 3.10): (a) c_l versus α, and (b) c_d versus α; [■] CFD (present study) and [▲] experiment (Ref. [9]).

1

Chapter 4

Airfoil optimization

4.1 Methodology

4.1.1 Airfoil geometry creation

The geometric description of airfoils is done with mathematical equations. Typically, an airfoil is a closed curve that has an infinity slope at the leading edge and a variation of curvature on the surface. Thus, multiple variables are required to define the shape of the airfoil. In past decades, various geometric representation methods have been developed in order to characterize and show the geometry of airfoils or other arbitrary aerodynamic objects.

Most methods use splines and have multiple control points in the space to control the shape of the object. The geometric definition of an object is crucial because the number of variables in its mathematical representation can significantly impact the computational time required for optimization or design tasks [10]. Typically, these methods utilize a mathematical approach with the minimum number of design variables.

Some of the well-known "constructive" methods available in the literature are B-spline

curves [11], CST [10], PARSEC parameterization [65] and free-form airfoil representation [66]. The constructive term refers to the methods where the airfoil geometry will be created without any base geometry to alter. The "deformative" methods, on the other hand, are the ones in which the airfoil geometry will be constructed by altering the shape of a base airfoil such as the Hicks-Henne bump function or Radial Basis Function Domain Element. Since the focus of this research was on constructive methods, we describe the mathematical equations of this category.

In the B-spline method, the polynomial curves and basis functions are determined by a set of control points in the space. Parameterization of the airfoil is done with the following general relation:

$$C(u) = \sum_{i=0}^{n-1} N_{i,p}(u) P_i, \tag{4.1}$$

in which $n = m - p$ for the basis functions of order p and p are less than or equal to the number of control points and will be defined as

$$N_{i,0}(u) = \begin{cases} 1 & u_i \leq u \leq u_{i+1} \\ 0 & otherwise \end{cases} \tag{4.2}$$

$$N_{i,p}(u) = \frac{u - u_i}{u_{i+p} - u_i} N_{i,p-1}(u) + \frac{u_{i+p+1} - u}{u_{i+p+1} - u_{i+1}} N_{i+1,p-1}(u), \tag{4.3}$$

and $u \in U$ where $U = [u_0, ..., u_m]$ and $u_i \leq u_{i+1}$.

In the CST method, the mathematical function consists of two parts, i.e., "class" and "shape" functions. This function was developed by Kulfan [10] and the method builds the upper and lower surface of the airfoil separately:

$$z_{upper} = C_{N1}^{N2}(x) S_{upper}(x) + x \Delta z_{upper}. \tag{4.4}$$

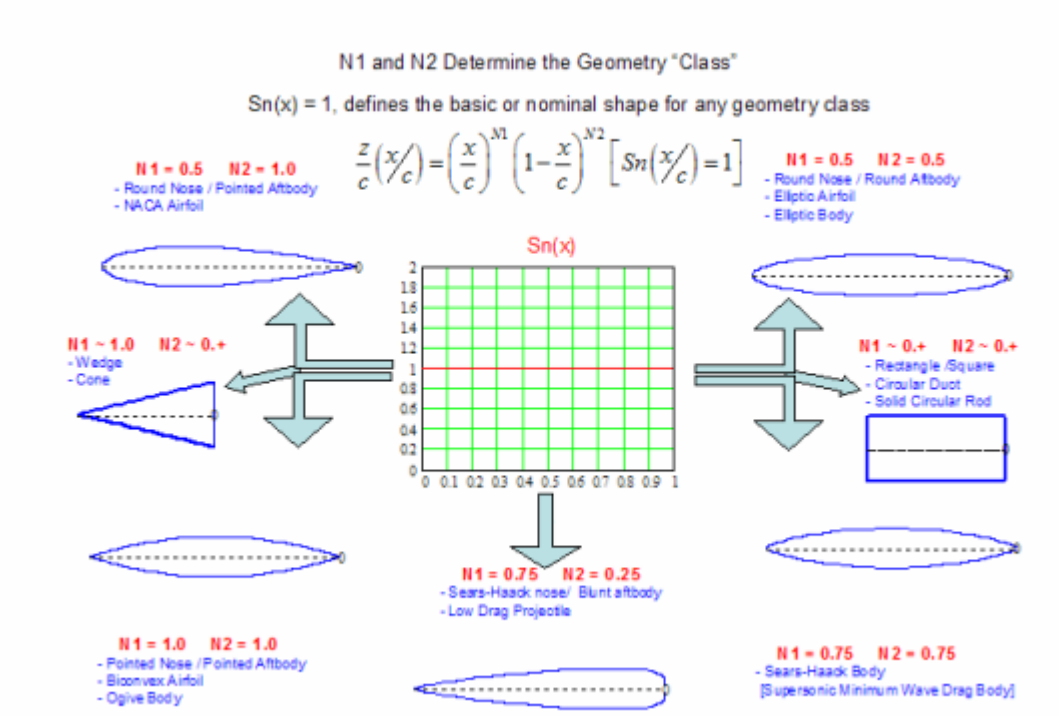

Figure 4.1: Different types of class in Class-shape transformation (CST). This image is taken from [10].

$$z_{lower} = C_{N1}^{N2}(x)S_{lower}(x) + x\Delta z_{lower}. \tag{4.5}$$

Equations 4.4 and 4.5 describe the upper surface and lower surfaces of the airfoil in which C_{N1}^{N2} shows the class function and S shows the shape function.

The Class function can be defined as

$$C_{N1}^{N2} = x^{N1}.(1-x)^{N2}. \tag{4.6}$$

where $N1$ and $N2$ are determined based on the shape of the object. For example, $N1 = 0.5$ and $N2 = 1.0$ correspond to the NACA type pointed aft and round nose shape, and $N1 = 0.5$ and $N2 = 0.5$ correspond to the round nose and round aft airfoil class.

The PARSEC method uses more physically significant properties to describe the airfoil

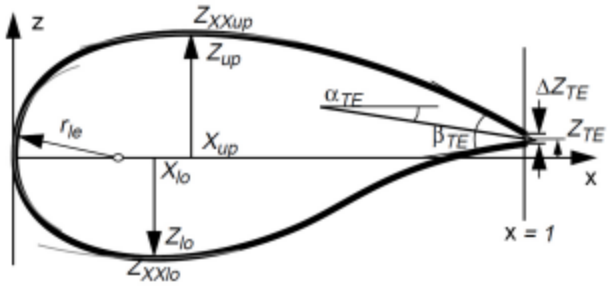

Figure 4.2: Schematic diagram showing the 12 parameters used for generating airfoils based on the PARSEC method [11].

shapes. It was proposed by Sobieczky [65], in which the upper and lower surfaces of the airfoils can be described by 6th-order polynomials as

$$z_{up}(x) = \sum_{i=1}^{6} a_i x^{i-0.5}, \tag{4.7}$$

$$z_{lo}(x) = \sum_{i=1}^{6} b_i x^{i-0.5}. \tag{4.8}$$

There are 12 equations in which the solution will be obtained using 12 parameters. Fig. 4.2 shows these variables including upper and lower (1,2) leading edge radius, (3,4) crest point, (5,6) the position, and (7,8) curvature of crest point, (9) trailing edge offset, (10) thickness, (11) angle, and (12) boat-tail angle.

Recent advances in computer technology and increased computational power have significantly accelerated the optimization process. Despite these improvements, researchers continue to seek ways to reduce the number of design variables. Furthermore, it is useful to establish methods in which design variables have a direct connection with the physical properties of airfoils. A newly developed method is Improved Geometry Parameter (IGP) airfoil parameterization which uses only 8 design variables to construct the airfoil geometry.

The IGP method for airfoil parameterization was introduced by [12]. The choice of airfoil

parameterization is pivotal, as it dictates the extent of the design space, and the number of design variables involved in the optimization problem, and ultimately influences the speed of the optimization process. In a study by Kroon [13], the CST method [10] was employed. However, the CST method is associated with a drawback, involving a high number of design variables lacking physical significance, leading to prohibitive computational costs dependent on the polynomial order applied.

In contrast, the IGP method brings an advantageous attribute by significantly reducing the CPU time. This method employs only 8 design variables, all of which are geometrically tangible, and it effectively decouples the camber and thickness of the airfoil. The IGP method achieves this by combining cubic Bézier curves with a thickness function, providing a constructive approach to airfoil parameterization. The resulting benefit is a more efficient and physically meaningful representation of the airfoil geometry. The thickness function is inspired by the NACA airfoil thickness function.

$$\begin{cases} \eta_c = 3s(1-s)^2 c_1 + 3(1-s)s^2 c_2 + s^3, \\ \zeta_c = 3s(1-s)^2 c_3 + 3(1-s)s^2 c_4, \end{cases} \tag{4.9}$$

where η_c and ζ_c are the dimensionless $x-$ and y-coordinates of the points on the camber, respectively; c_1 to c_4 are design variables (c_1 and c_2 are the central points on the abscissa, and c_3 and c_4 are the control points on the ordinate of the camber line), and $0 \leq s \leq 1$ is the curvilinear coordinate.

The NACA-inspired thickness function is written as follows

$$\tau(\eta) = \tau_1 \eta^{0.5} + \tau_2 \eta + \tau_3 \eta^2 + \tau_4 \eta^3 + \tau_5 \eta^4, \tag{4.10}$$

where τ_1 to τ_5 are additional design variables.

Using Eqs. 4.9 and 4.10, the x- and y-coordinates of the points on the upper surface of the airfoil can be found, respectively, from

$$\begin{cases} \eta_u = \eta_c, \\ \zeta_u = \zeta_c + \frac{1}{2}\tau(\eta_c), \end{cases} \tag{4.11}$$

and those on the lower surface of the airfoil from

$$\begin{cases} \eta_l = \eta_c, \\ \zeta_l = \zeta_c - \frac{1}{2}\tau(\eta_c), \end{cases} \tag{4.12}$$

respectively.

Considering c_1 to c_4 and τ_1 to τ_5, in total, 9 design variables are involved in the optimization framework. However, since the thickness at the trailing edge is assumed to be 0, i.e. $\tau(1) = 0$, then $\tau_1 + \tau_2 + \tau_3 + \tau_4 + \tau_5 = 0$ reduces the number of design variables to 8. Lu et al. [12] tested 2199 airfoils to find the accuracy of the IGP method and to find the limits for the design variables. With few exceptions, the following limits were found applicable for the tested airfoils, and as a result, they are adopted in the present study. It should be noted that here some limits have been modified from the original values provided in Ref. [12] to allow for a broader design space. The control points of the camber line can be defined as below:

$$\begin{cases} c_1 \in [0.010, 0.970] \\ c_2 \in [0.020, 0.970] \\ c_3 \in [-0.14, 0.247] \\ c_4 \in [-0.20, 0.206] \end{cases} \tag{4.13}$$

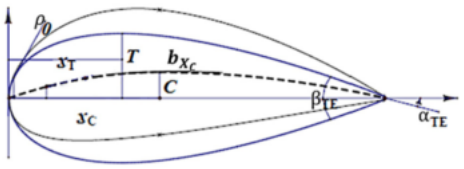

Figure 4.3: Illustration of geometric variables in IGP parameterization [12].

Also, the design variables in the thickness function can be introduced as follows:

$$\begin{cases} \tau_{max} \in [0.07, 0.45] \\ \eta_{\tau_{max}} \in [0.2002, 0.4813] \\ \overline{\rho_0} = \dfrac{\rho_0}{(\tau_{max}/\eta_{\tau_{max}})^2} \in [0.1750, 2.5] \\ \overline{\beta_{TE}} = \dfrac{\beta_{TE}}{\tan^{-1}(\dfrac{\tau_{max}}{1-\eta_{\tau_{max}}})} \in [0.1452, 4.8724] \end{cases} \tag{4.14}$$

where τ_{max} is the maximum thickness ratio, $\eta_{\tau_{max}}$ is the dimensionless x-coordinate of the location of the maximum thickness, ρ_0 is the radius of the leading edge and β_{TE} is the boat-tail angle; also, $\overline{\rho_0}$ and $\overline{\beta_{TE}}$ are the normalized counterparts of ρ_0 and β_{TE}, respectively. As a result, the 8 design variables are $c_1,\ c_2,\ c_3,\ c_4,\ \tau_{max},\ \eta_{\tau_{max}},\ \overline{\rho_0},$ and $\overline{\beta_{TE}}$ and are used in the optimization framework here for the airfoils. Some of the definitions introduced above are shown in Fig. 4.3.

4.1.2 Optimization method

In this study, a Matlab implementation of NSGA-II [67] was used. The NSGA-II setting parameters used in this study are summarized in Table 4.1. The values of the parameters were obtained from previous studies such as [13] and by trial and error. Interested readers

find the NSGA-II description in Chapter 2.

Table 4.1: NSGA-II setting parameters used in the present study.

Parameter	**Value**
Population size	200
Number of generations	100
Mutation probability	0.05
Crossover index	10
Distribution index	10

4.1.3 Objective functions

In this section, the objective functions implemented in the optimization framework are reported. For an infinite span wing, which corresponds to a very high aspect ratio, the induced drag is negligible, and thus the airfoil drag, c_{d_0} is the main contribution in the drag term. With this assumption, we are considering different scenarios by adding the effect of induced drag and tether drag and implementing them in their respective sections.

Multi-objective optimization algorithms need the presence of two or more conflicting objective functions. The optimizer must minimize multiple objective functions simultaneously while achieving higher performance in one objective will lead to worse performance in the other. After incorporating a multi-objective algorithm, we had to devise two conflicting objective functions. One should reflect the aerodynamic performance, while the other should illustrate the structural aspect of the airfoil.

The post-processor function sequentially acquires and saves aerodynamic data in a vector. The data will then be filtered using MATLAB's regexp function. This technique looks for a regular expression in a character vector, where c_l and c_d are kept as characters. The final part of the code will be utilized to filter the linear region of c_l vs. α and save them with their corresponding c_d in another matrix to calculate the aerodynamic objective function later.

The aerodynamic efficiency term, $\chi = c_l(\frac{c_l}{c_d})^2$ presented in 1.4.1, will be used in aerodynamic objective function. Also, the maximum thickness introduced as one of the design variables in 4.14 will be implemented in the structural objective function. The justification for selecting this variable is that the chord length of the airfoils is set to 1m. As a result, the length of the abscissa remains constant, while the maximum length on the ordinate, or maximum thickness, represents the airfoil's structural criteria.

Baseline system

Two objective functions are presented to show the kite's aerodynamic and structural characteristics. In the baseline airfoil study, the aerodynamic and structural objective function is $1000/f_P$ and $-f_T$, respectively. f_P and f_T are introduced in Eq.4.15 and Eq.4.16. The range of c_l values studied here allows for the impacts of gusts and turbulence, which can cause the angle of attack to change. Weights, w_i, are chosen based on research on conventional wind turbines.

$$f_P = \sum_{i=1}^{8} w_i c_{l_i} (\frac{c_{l_i}}{c_{d_i}})^2, \tag{4.15}$$

$$f_T = max(\tau) \quad 0 \leq \eta \leq 1. \tag{4.16}$$

In Eq.4.15, w_i are the weights corresponding to c_{l_i} as shown in Table 4.2.

Table 4.2: Range of lift coefficients and corresponding weights considered in numerical studies in Sections 4.2.1

Parameter	$i = 1$	2	3	4	5	6	7	8
$c_{l,i}$	0.5	0.6	0.7	0.8	0.9	1	1.1	1.2
w_i	0.05	0.1	0.1	0.1	0.1	0.15	0.2	0.2

The effects of kite aspect ratio

To consider the effect of the aspect ratio on the airfoils of crosswind kites, we added the induced drag of an elliptical distribution, where Oswald efficiency factor is $e = 1$, to the drag term in the denominator of the f_P as shown in the Eq. 4.17. The reason that we chose $e = 1$ is for the simplicity of the analysis. In Eq. 4.17, ${c_{d_i}}^{induced} = c_{l_i}^2/(\pi AR)$ is the induced drag coefficient and AR are the aspect ratios considered for various types of the flying objects, these values will be introduced in their respective section. Furthermore, the discretized aerodynamic efficiency function, f_P for this section is calculated by utilizing Table 4.3

$$f_P = \sum_{i=1}^{8} w_i c_{l_i} (\frac{c_{l_i}}{c_{d_i} + {c_{d_i}}^{induced}})^2, \tag{4.17}$$

The effects of tether's area ratio

Next, to describe the effect of tether drag, we include the contribution of the tether drag into the total drag. To better observe the effects of tether drag, the induced drag is kept as zero for this section. The drag coefficient term in the aerodynamic efficiency is modified as follows to include the tether drag effects in the optimization framework:

$$f_P = \sum_{i=1}^{8} w_i c_{l,i} (\frac{c_{l,i}}{c_{d,i} + \frac{1}{4}\overline{A} c_{d_t}})^2, \tag{4.18}$$

Table 4.3: Range of lift coefficients and corresponding weights considered in numerical studies in Sections 4.2.2 and 4.2.3.

Parameter	$i = 1$	2	3	4	5	6	7	8
$c_{l,i}$	1	1.1	1.2	1.3	1.4	1.5	1.6	1.7
w_i	0.05	0.1	0.1	0.1	0.1	0.15	0.2	0.2

where $\overline{A}$ is the ratio between the projected area of the tether (i.e., tether length times tether diameter) and the kite planform area, i.e., $\overline{A} = \frac{A_t}{A_k}$; and c_{d_t} is the normal flow drag coefficient which is commonly taken as 1.0 [22] as described in this section 1.4.1. Table 4.3 is used for calculating the f_P in this section.

4.1.4 Aerodynamic solver

XFOIL [55] is used to obtain the lift and drag coefficients of the airfoils throughout a broad range of angles of attack, specifically from $\alpha = -10$ to 25 degrees. The aerodynamic computations are performed at $Re = 6 \times 10^6$ (based on the airfoil chord length) which is within the typical range of Reynolds numbers for crosswind kites and a Mach number of $M = 0.257$. Also, $Ncrit = 9$ is taken, which represents the condition in an "average wind tunnel" and also corresponds to the standard "e^9 method" of transition prediction. For more information on XFOIL, interested readers are referred to Chapter 3.

According to the typical wind turbines, the tip speed of the blade is roughly $60m/s$ [13]. In addition, the wind velocity in the operational height of the wind turbine is around $10m/s$. The resultant velocity is around $61m/s$. However, The crosswind kite operates at a greater height and has a higher gyration radius [28]. This gives an idea of having a higher resultant velocity for a crosswind kite. Combining Reynolds and Mach numbers yields a velocity of $87m/s$, which is consistent with the earlier study [28].

4.1.5 Solution process

To initiate the optimization process, an initial population (i.e., a series of airfoils) is generated randomly based on the user-provided ranges for design variables. A Matlab code was developed to generate a text file that contains the commands to execute XFOIL, such as that for reading airfoil coordinates, determining the type of solver (viscous or inviscid),

determining the Reynolds number, etc. After each execution, XFOIL outputs are stored in a text file which is then accessed by a post-processor in Matlab. The post-processor identifies the linear range of the $c_l - \alpha$ curve of the airfoil and computes the objective functions defined in Section 4.1.3. The numerical values of the design variables and the objective functions are then passed to the optimizer. In the optimizer, the next generation of the initial population is created using genetic operators, such as crossover and mutation. This process is shown in Fig. 4.4.

4.2 Numerical results

Here, We report the numerical results of the optimization problem for the Airborne wind energy application. The sections are as follows: First, we present the numerical results of the baseline system (4.2.1), the system in which we only take into account the airfoil drag in the

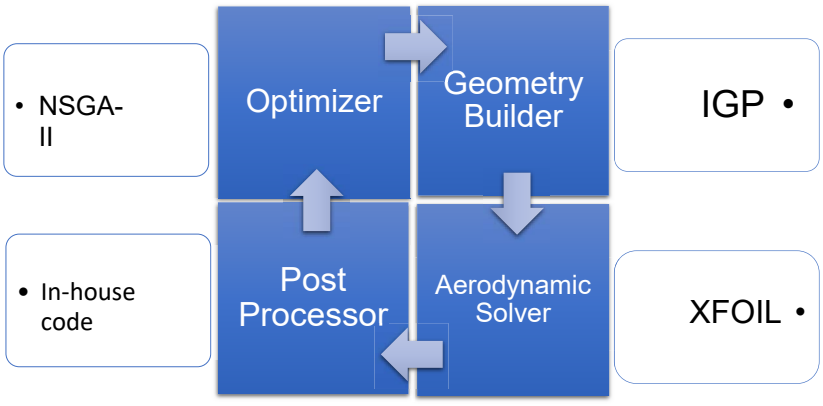

Figure 4.4: The working blocks are creating the airfoil optimization framework. It consists of four blocks working as a series of events including an optimizer, geometry builder, aerodynamic solver, and a post-processor

of the kite's aspect ratio (4.2.2), and lastly the system where the effects of the tether's area ratio are taken into account (4.2.3) in the optimization framework. The computational fluid dynamics findings, which were used as a means to relatively compare the XFOIL aerodynamic results against them, will be presented in their corresponding sections.

4.2.1 Optimal airfoils for the baseline system

Figure 4.5 shows the optimal Pareto front from the present study (asterisk) in which the IGP method was implemented in the optimization framework and that from [13] (circle) in which the CST method was used. Comparing these results, the former shows marginal improvement, compared to the latter, for $f_T \leq 0.35$ and noticeable improvements for thicker airfoils. It should be reminded that for a given maximum thickness ratio f_T, a solution (i.e., airfoil) is superior if it has a higher f_P and thus has a lower $1000/f_P$ on the Pareto front. From the figure, it is also seen that the present Pareto front is well distributed over a wide

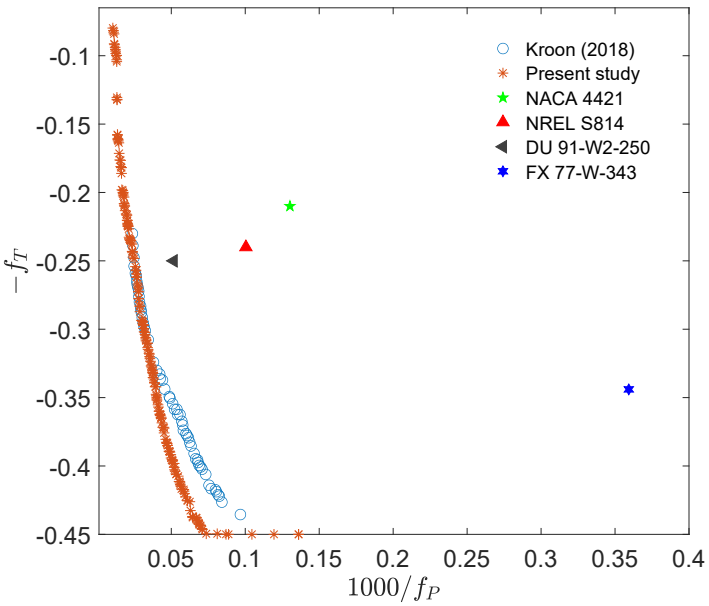

Figure 4.5: Pareto-optimal fronts from the present study and that from Ref. [13].

range of f_T, offering solutions for both very thin and very thick airfoils. On the other hand, no solution was reported for $f_T < 0.2$ in [13].

For comparison purposes, numerical results for the NACA 4421, NREL S814, DU 91-W2-250, and FX 77-W-343 airfoils were also obtained using XFOIL and are presented in Fig. 4.5. These airfoils are commonly employed in wind turbine blades, and their maximum thickness ratio ranges from 21% to approximately 34%. As shown in the plot, all four airfoils are positioned on the right-hand side of the Pareto optimal front. This suggests that, compared to the optimal airfoils with the same maximum thickness ratio, these airfoils are aerodynamically less efficient.

Furthermore, as an example to represent the change in the power production, the potential power augmentation is approximately 66%, when the maximum thickness changes from $f_T = 40\%$ to 30%. This is a crucial finding as this amount is significant in the scales present in the wind energy industry.

To confirm that the superiority of the solutions from the present Pareto front is not due to differences between XFOIL (used in this study) and RFOIL (used in [13]), c_l and c_d for two optimal airfoils ($\tau_{max} = 35\%$ and 40%) from Kroon's study [13] were obtained using XFOIL and compared with those reported by Kroon using RFOIL.[1] The plots are shown in Fig. 4.6. Figures 4.6a and 4.6c show the variation of lift coefficient as a function of angle of attack for the airfoils with $\tau_{max} = 35\%$ and 40%, respectively. Two different behaviors can be observed in the range where the angle of attack is changing from $\alpha = -10$ to 20 degrees. In the regions where large flow separation is expected (i.e., for high positive/negative α), the results from the two aerodynamic solvers, i.e., XFOIL and RFOIL, drastically differ from each other. On the other hand, in the linear range of the $c_l - \alpha$ curve, where no major

[1]The airfoils from Kroon's study were digitized, and through curve fitting, the polynomial coefficients used in the CST parameterization method were obtained, which then were used to create smooth airfoil profiles. Also, the lift coefficient as a function of angle of attack and drag polar were digitized from the data provided in their study.

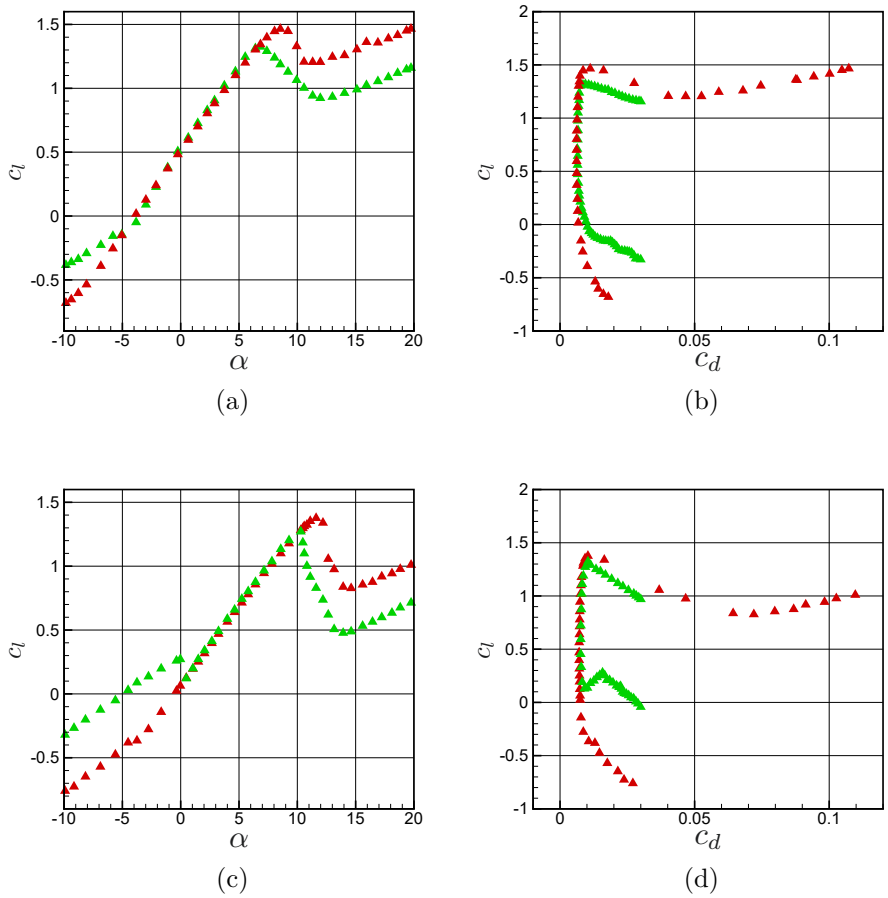

Figure 4.6: Variation of (a,c) lift coefficient as a function of angle of attack, and (b,d) lift coefficient as a function of drag coefficient for the airfoils with $\tau_{max} = 35\%$ (first row) and 40% (second row), respectively, in [13]: XFOIL[▲] and RFOIL[▲].

flow separation is expected, the two curves are almost coincident. A similar behavior can be observed from the drag polar shown in Figs. 4.6b and 4.6d. Thus, one may conclude that since the results from XFOIL and RFOIL are almost identical over the linear range of $c_l - \alpha$ (which is employed in the optimization process), the difference shown in Fig. 4.5 has its roots in different airfoil parameterization methods adopted here and in [13].

Next, Fig. 4.7 shows the profile of the airfoils with the maximum thickness ratio of $\tau_{max} = 25\%,\ 30\%,\ 35\%$ and 40%, obtained from the present optimal Pareto front. An

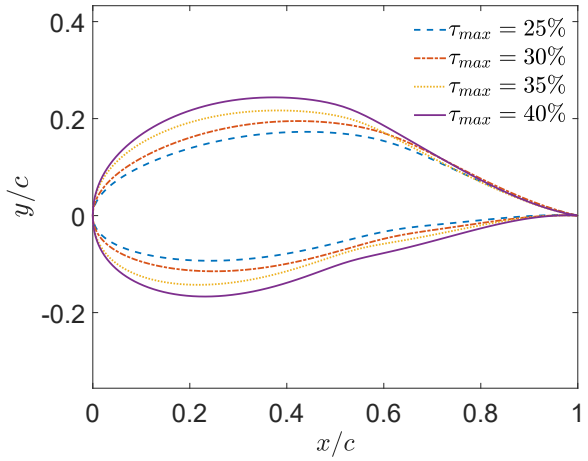

Figure 4.7: Selected optimal airfoils from the present study Pareto front (Fig.4.5), with $\tau_{max} = 25\%$, 30%, 35% and 40%.

unusual change of curvature appears close to the trailing edge on the pressure (i.e. lower) side. This waviness, which is more visible on the airfoil with $\tau_{max} = 40\%$, appears to be slightly reducing the pressure drag at higher angles of attack and thus is aerodynamically beneficial. However, for practical reasons, smooth surfaces are desirable. Nevertheless, for example, for the optimal airfoil with $\tau_{max} = 35\%$, the difference between f_P for the original (i.e., non-smooth) optimal airfoil and that for the smoothed version was found to be below 1%.

Computational fluid dynamics results

Some computational fluid dynamics (CFD) simulations are performed for the optimal airfoil with $\tau_{max} = 25\%$, the results of which are used to compare with XFOIL results. The CFD mesh convergence study and the validation of the CFD framework are presented in Chapter 3. All the CFD simulations performed in this study follow the same mesh and solver settings as those presented in Chapter 3.

Figure 4.8a shows the variation of the lift coefficient as a function of the angle of attack.

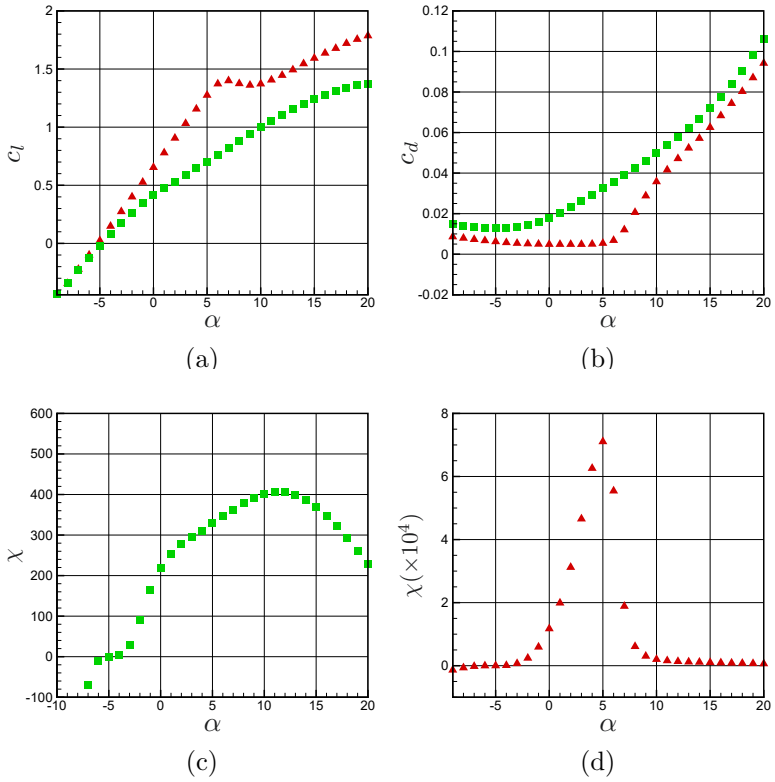

Figure 4.8: Variation of the (a) lift coefficient, (b) drag coefficient, (c)power coefficient obtained from CFD, and, (d)power coefficient obtained from XFOIL as a function of the angle of attack for the selected optimal airfoil ($\tau_{max} = 25\%$): XFOIL[▲] and CFD[■].

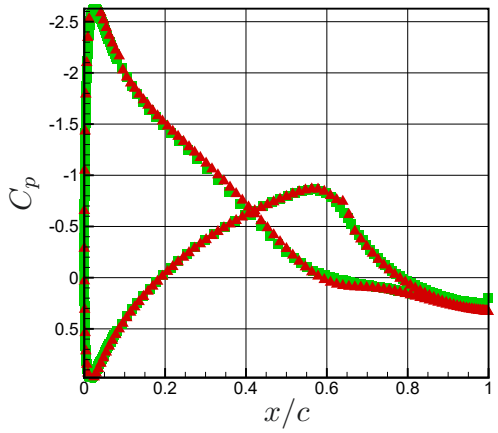

(a)

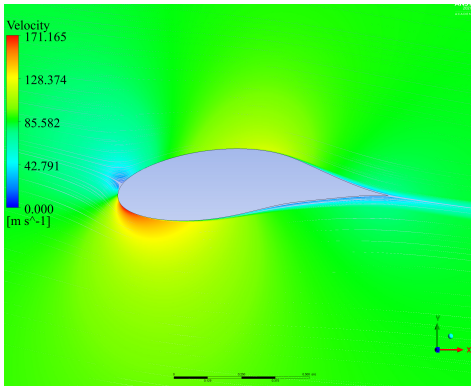

(b)

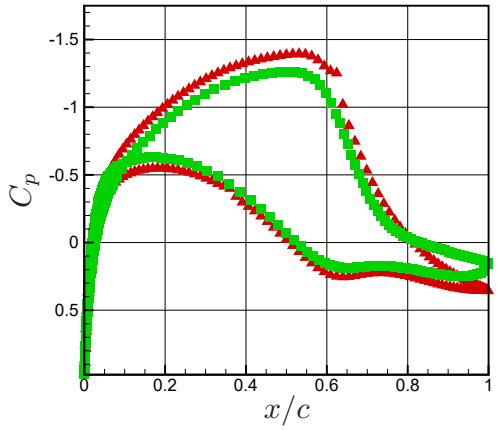

(c)

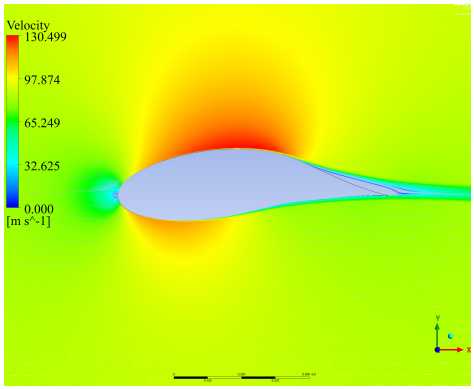

(d)

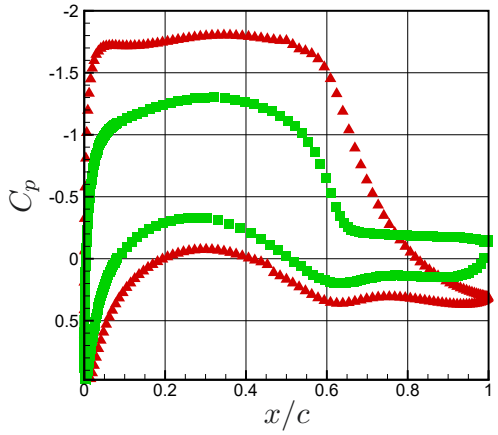

(e)

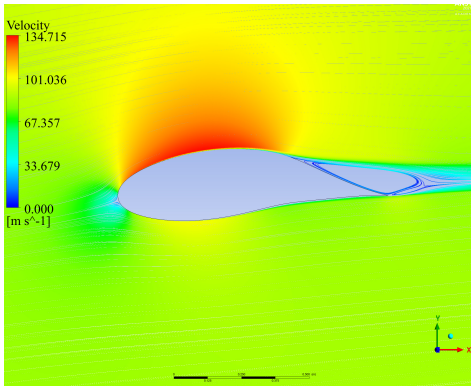

(f)

Figure 4.9: Distribution of C_p over the suction and pressure sides of the optimal airfoil ($\tau_{max} = 25\%$) and the corresponding streamlines at (a,b) $\alpha = -9°$, (c,d) $\alpha = 0°$, and (e,f) $\alpha = 6°$: XFOIL[▲] and CFD[■].

As seen from the figure, XFOIL and CFD results match quite well over $\alpha \leq -5$ deg while for $\alpha > -5$ deg and by increasing the angle of attack, the difference between the two sets of results generally increases. The maximum difference occurs in the stall region predicted by XFOIL ($5 \leq \alpha \leq 7$ deg), and XFOIL always overestimates c_l values. From CFD results, no reduction of the lift coefficient is observed up to $\alpha = 20$ deg. Figure 4.8b shows the variation of c_d as a function of α, obtained by XFOIL and CFD for the optimal airfoil with $\tau_{max} = 25\%$. As seen, XFOIL underestimates c_d over the entire range of the angle of attack.

Finally, the aerodynamic efficiency curves obtained from Fig. 4.8c CFD and d XFOIL are presented. As seen from the two curves, χ increases with the angle of attack, reaches a maximum, and then decreases with further increasing the angle of attack. The maximum value of χ occurs approximately at $\alpha = 12$ deg based on the CFD curve while it occurs at $\alpha = 5$ deg based on the XFOIL curve. As seen, the aerodynamic efficiency values obtained from XFOIL are several orders of magnitude higher than those from CFD. This is, however, very much expected since XFOIL overestimated c_l while underestimated c_d.

Figure 4.9 shows the distribution of the pressure coefficient over the optimal airfoil with $\tau_{max} = 25\%$, obtained from XFOIL and CFD, and the corresponding streamlines obtained from CFD at $\alpha = -9, 0$, and 6 deg. As seen from Fig. 4.9a, at $\alpha = -9$ deg, where no major flow separation occurs, as confirmed from Fig. 4.9b, the two distributions match quite well. At $\alpha = 0$ (Fig. 4.9c), some discrepancies can be observed over the suction side (i.e., negative values of C_p), particularly close to the trailing edge. The C_p distribution obtained from CFD indicates an adverse pressure gradient and consequently flow separation from the upper side of the airfoil, at $x/c \approx 0.8$ while no major separation is captured by XFOIL. The flow separation from the suction side of the airfoil and the formation of a small recirculation region close to the trailing edge can be confirmed from Fig. 4.9d. At $\alpha = 6$ deg (Fig. 4.9e), although, for the most part, the two distributions are similar in the overall

trend, the magnitudes are evidently different. A major flow separation is captured by CFD at $x/c \approx 0.6$ whereas no separation is seen from XFOIL distribution. The discrepancy can be confirmed by taking a closer look to the streamlines in Fig. 4.9f. A recirculation region over the last 40% of the airfoil chord length can be observed; however, the circulation region appears to be stable, and therefore, stall does not occur at this angle of attack.

It was shown in the above that XFOIL fails to provide accurate results when large flow separations are expected to occur. This may be attributed to the limited accuracy of viscous flow modeling in XFOIL. More precisely, the lagged dissipation integral boundary layer formulation and the e^N formulation combined with the incompressible potential flow solution are used for limited flow separation and may not be suitable for growing region of flow separation [56, 68]. In addition, a first-order upwind scheme has been implemented in XFOIL for regions with sharp changes while a second-order upwind discretization method was implemented in the CFD solver to resolve flow properties. Previous studies have also highlighted the discrepancies between XFOIL and CFD results. For example, in the study by [68], at a Reynolds number and a Mach number close to this study, i.e., $Re = 5.2 \times 10^6$ and $M = 0.28$, the results from CFD (OVERFLOW) and XFOIL differ from each other in transition and highly separated regions. Therefore, for scenarios with no or minor flow separation, which typically occur over the linear/quasi-linear range of $c_l - \alpha$ curve, XFOIL results can be trusted. This is, for the most part, the range considered in the present optimization studies.

4.2.2 Optimal airfoils for the modified system: the effects of kite aspect ratio

Here, the effects of including the induced drag from a finite aspect ratio kite on the optimal Pareto front and the corresponding airfoil profiles are examined. It is noted that the numerical results in this section and Section 4.2.3 were obtained with a range of lift coefficients different from those used for the baseline system (Table 4.2). Inclusion of the induced drag and/or tether drag results in a significant increase of the total drag, leading to a considerable reduction of f_P. To compensate for this reduction and thus obtain competitive airfoils for the modified system, it is inevitable to sweep over higher values of the lift coefficient, as given in Table 4.3. A similar strategy was previously used by [13].

Three aspect ratios were selected for numerical studies based on existing crosswind kite prototypes: $AR = 4$ corresponding to low-aspect-ratio kites, particularly soft kites, $AR = 12$ corresponding to kites with moderate aspect ratios, and $AR = 20$ corresponding to high-aspect-ratio kites, typically rigid-wing kites, such as Makani's M600 kite [69].

Figure 4.10 shows the Pareto fronts with (i.e., modified system) and without (i.e., baseline system) aspect ratio considerations. As expected, for a given airfoil thickness, f_P is higher for the wing with a higher aspect ratio. As seen from the figure, by increasing the aspect ratio, the Pareto front for the modified system approaches that of the baseline system. This is particularly evident for $AR = 20$ and larger f_T values. However, for thinner airfoils (i.e., smaller f_T), the deviation of the Pareto front of the modified system from that of the baseline system becomes larger. This may be attributed to the fact that for kites with thinner airfoils, the induced drag becomes dominant over the profile drag. Consequently, the aspect ratio has a more significant impact on the power output objective function f_P, leading to a more pronounced difference.

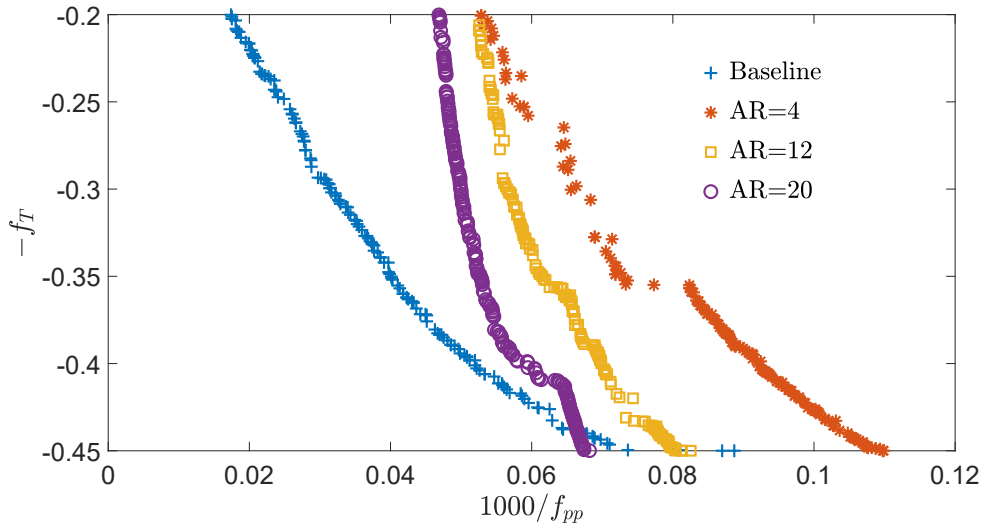

Figure 4.10: Pareto fronts obtained from the optimization framework where the effects of kite aspect ratio have been included.

This behavior seems to be true for $AR = 12$ and 20. For $AR = 4$, on the other hand, the induced drag appears to be the dominant part of the total drag, even for thicker airfoils, which might explain seeing a different Pareto front. As also seen from Fig. 4.10, over a small range of large values of f_T ($0.44 \leq f_T \leq 0.45$), seemingly superior airfoils may be obtained for the modified system with $AR = 20$. This unexpected outcome may be explained by the fact that greater values of c_l (and thus potentially larger f_P) were considered for the modified system, for the reasons discussed above (cf. Tables 4.2 and 4.3). Figures 4.11a to c show the optimal airfoils with $\tau_{max} = 20\%$, 30% and 40%, respectively. As seen, the airfoil profiles for $AR = 12$ and 20 are quite similar, particularly for $\tau_{max} = 20\%$ and 30%. The optimal airfoils, particularly those obtained with $AR = 20$, have a cusp at their trailing edge. For the cases with $AR = 4$ and $AR = 12$, as the τ_{max} increases from 20 to 30, the location of τ_{max} will shift toward the leading edge and from 30 to 40, this location shifts toward the trailing edge. For the case with $AR = 20$, as the τ_{max} increases, the location of τ_{max} will shift toward the trailing edge.

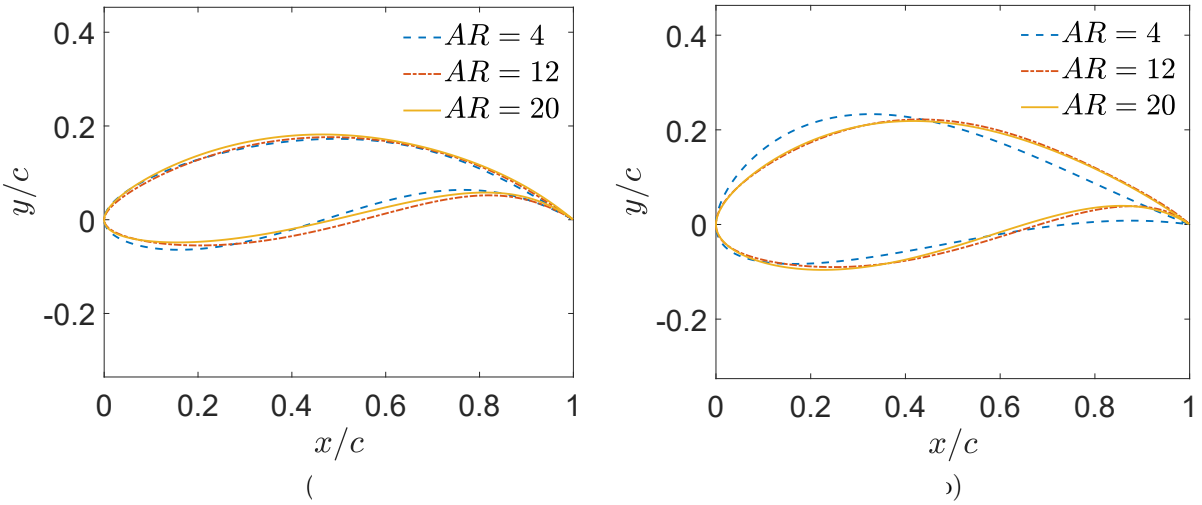

(

)

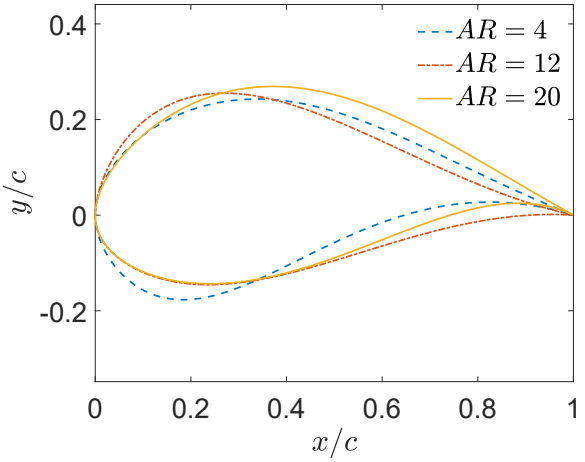

(c)

Figure 4.11: Selected optimal airfoils with aspect ratio consideration: (a) $\tau_{max} = 20\%$, (b) $\tau_{max} = 30\%$ and (c) $\tau_{max} = 40\%$.

Computational fluid dynamics results

Some CFD simulations were performed for the optimal airfoil with $\tau_{max} = 20\%$ and considering $AR = 12$. The goal is to further examine the aerodynamic behavior of this airfoil since thinner airfoils are generally more appealing due to their greater potential for power generation, as evidenced by the Pareto fronts presented in Fig. 4.10. In addition, the CFD

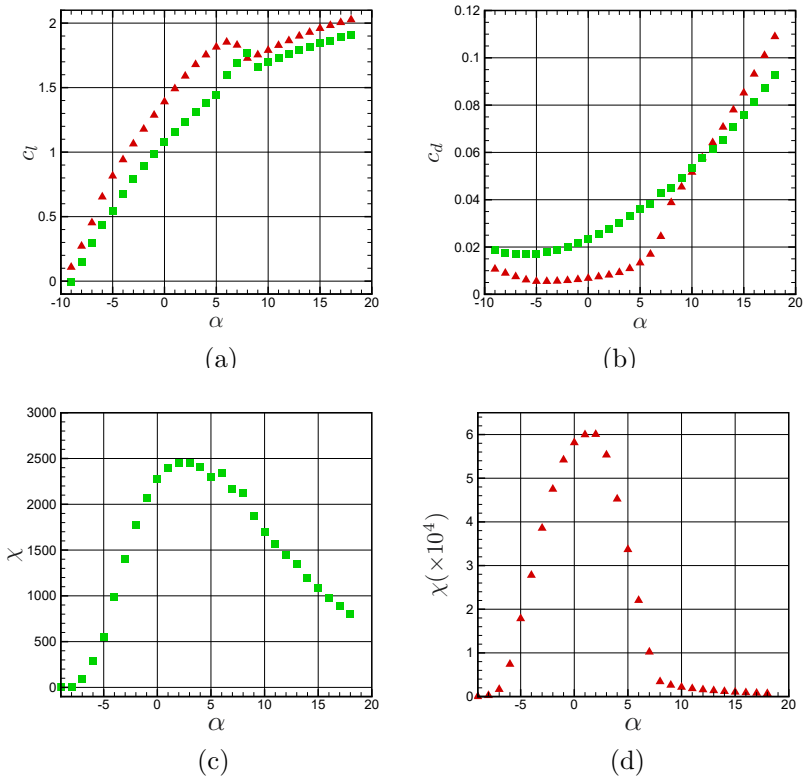

Figure 4.12: Variation of the (a) lift coefficient, (b) drag coefficient, (c) corresponding power coefficient obtained from CFD, and (d) power coefficient obtained from XFOIL as a function of angle of attack for the selected optimal airfoil ($\tau_{max} = 20\%$, $AR = 12$): XFOIL[▲] and CFD[■].

results are used for comparison against XFOIL results.

As seen from Fig. 4.12a, despite differences in numerical values, the c_l curves obtained from CFD and XFOIL are quite similar. The lift coefficient increases quasi-linearly with α until reaching stall, and after a small reduction, it increases with α in the post-stall regime. The stall angle of attack is approximately $\alpha = 6$ deg based on XFOIL and $\alpha = 8$ deg based on CFD results. From Fig. 4.12b, it is seen that, for $\alpha > 11$ deg, XFOIL overestimates the c_d values. This, however, occurs in the post-stall regime where XFOIL results are not generally accurate due to large flow separations. From Figs. 4.12c and d, it is again seen that the χ values obtained from CFD are several orders of magnitude smaller than those

obtained from XFOIL. The maximum χ is reached at approximately $\alpha = 1$ deg (XFOIL) and $\alpha = 2$ deg (CFD). Comparing these α values with those corresponding to the maximum c_l and maximum c_l/c_d shows that from XFOIL, $c_{l_{max}}$ occurs at $\alpha = 6$ deg and $(c_l/c_d)_{max}$ at $\alpha = -1$ deg while from CFD, $c_{l_{max}}$ occurs at $\alpha = 8$ deg and $(c_l/c_d)_{max}$ at $\alpha = 0$ deg.

Finally, C_p plots and the streamlines at $\alpha = -9, 0$ and 6 deg are shown in Fig. 4.13. As seen from the C_p plots (the left column), by increasing α, the pressure distribution over the upper side obtained by XFOIL increasingly deviates from that obtained by CFD. In Fig. 4.13a, the two distributions are almost identical. However, as seen from Figs. 4.13c and 4.13e, in addition to the differences in C_p values, the flow separation region (indicated by a plateau close to the trailing edge) length over the upper side of the airfoil is underestimated by XFOIL. As seen from Fig. 4.13b, the flow separation, caused by large adverse pressure gradients, is observed from both lower (at $x/c \approx 0.5$) and upper (at $x/c \approx 0.9$) sides of the airfoil at $\alpha = -9$ deg. At $\alpha = 0$ and 6 deg, Figs. 4.13d and 4.13f confirm that flow separates from the suction side of the airfoil close to the trailing edge.

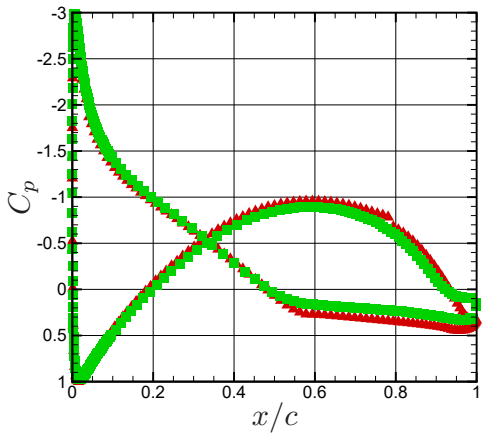

(a)

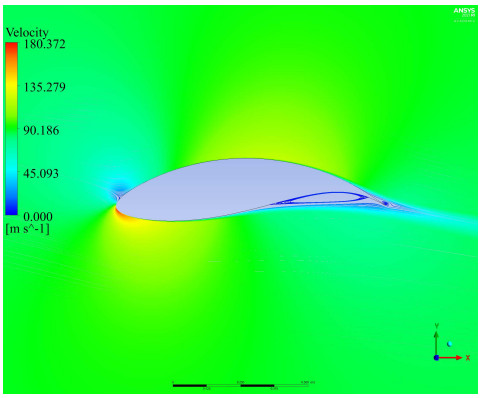

(b)

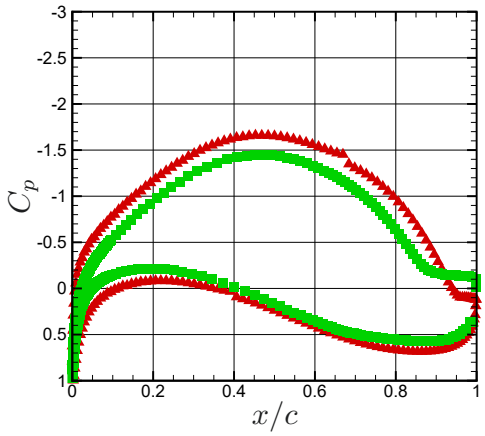

(c)

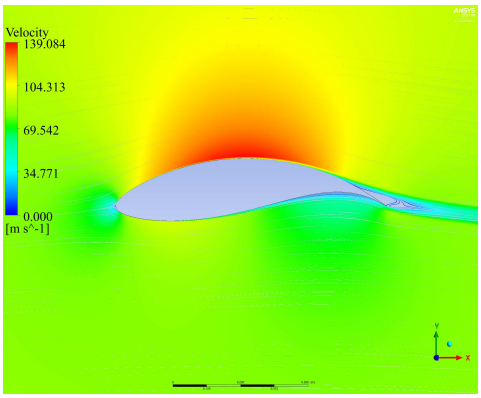

(d)

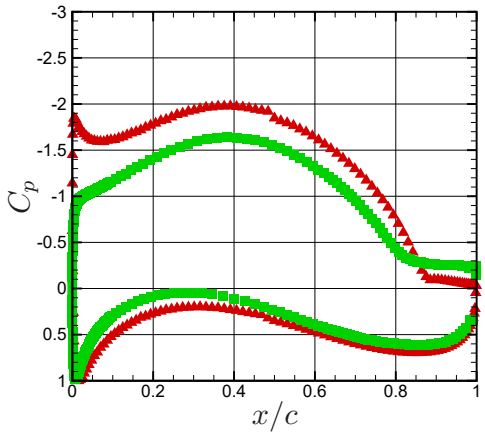

(e)

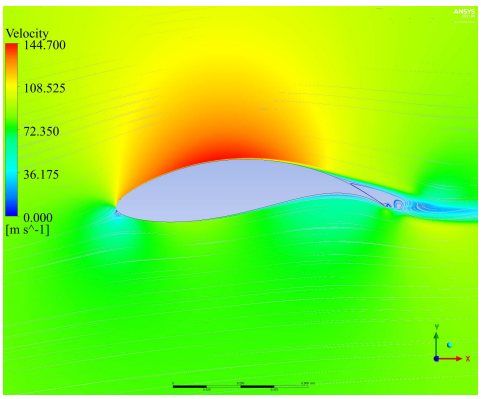

(f)

Figure 4.13: Distribution of C_p over the suction and pressure sides of the optimal airfoil ($\tau_{max} = 20\%$, $AR = 12$) and the corresponding streamlines with at (a,b) $\alpha = -9°$, (c,d) $\alpha = 0°$, and (e,f) $\alpha = 6°$: XFOIL[▲] and CFD[■].

4.2.3 Optimal airfoils for the modified system: effects of tether's area ratio

Figure 4.14 shows the Pareto fronts when the tether drag effects are included. Four area ratios $\overline{A} = 0.1$, 0.33, 0.5, and 0.7 were selected for numerical studies considering the existing kite systems. For example, Ampyx Power's AP-3 (i.e., a rigid-wing kite) is estimated to have an area ratio of approximately 0.33 [70, 71] while SKS PN-14 (i.e., a soft kite) from Skysails has an area ratio between approximately 0.06 and 0.12, if the laid-out surface area is used for the calculation [72].

As expected, by increasing the area ratio (and thus increasing the tether drag), the Pareto front shifts more to the right – lower power values. Interestingly, for lower values of $\overline{A}$, like $\overline{A} = 0.1$, optimal airfoils with very different thickness ratios but similar power values can be achieved. However, by increasing $\overline{A}$, Pareto fronts spread over a wider range of $1000/f_P$.

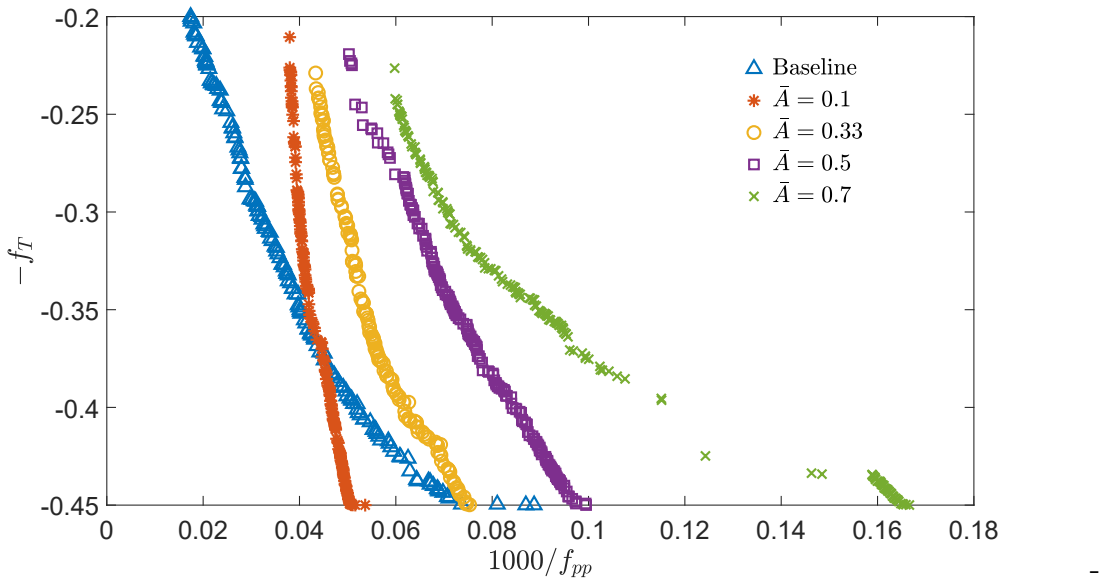

Figure 4.14: Pareto fronts obtained from the optimization framework where the effects of the area ratio have been included.

In other words, the sensitivity of the power output to the thickness ratio increases with the increase in $\overline{A}$. For example, for $\overline{A} = 0.1$, the abscissa varies approximately between 0.04 and 0.05 while for $\overline{A} = 0.5$, it varies between 0.05 and 0.1 over almost the same range of f_T. This, however, seems a counter-intuitive outcome since it is expected that the contribution of the tether drag becomes more and more dominant in the total drag when $\overline{A}$ is increased, thus making it as the main driving factor of the aerodynamic design.

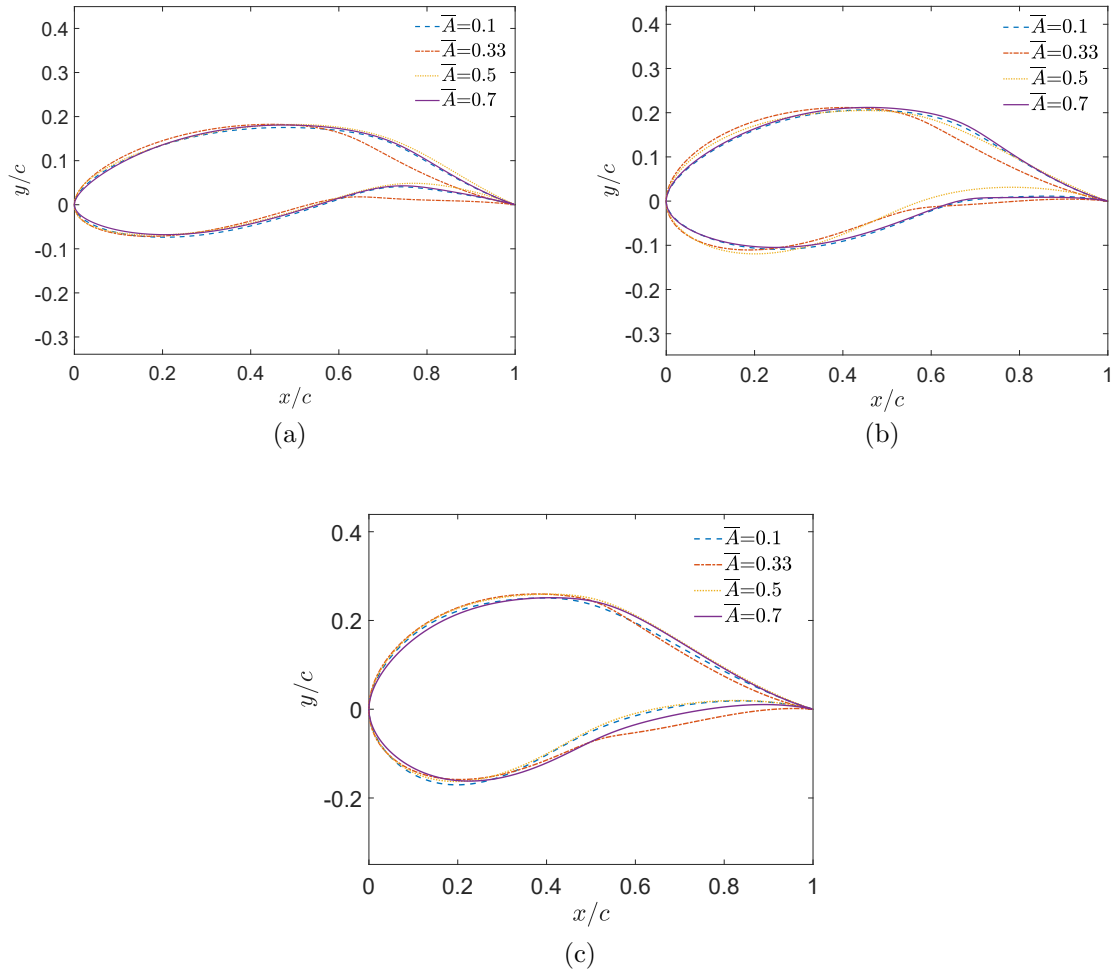

Figure 4.15: Selected optimal airfoils with area ratio consideration: (a) $\tau_{max} = 22\%$, (b) $\tau_{max} = 30\%$, and (c) $\tau_{max} = 40\%$.

As also seen from the figure, for the modified system with $\overline{A} = 0.1$, over $f_T > 0.38$, seemingly superior airfoils are obtained compared to the baseline system. This might be again because c_l is swept over greater values during the optimization, when including tether drag effects (cf. Tables 4.2 and 4.3).

Figures 4.15a-c show the optimal airfoils with $\tau_{max} = 22\%$, 30% and 40%, respectively.[2] As seen from the figures, close to the trailing edge, a noticeable change of curvature, particularly over the lower side of the airfoils, is observed. The resulting shape is reminiscent of a flap. This is mostly evident from the profiles shown in Fig. 4.15a and particularly for $\overline{A} = 0.33$. It appears that to accommodate large c_l values considered in the optimization (Table 4.3) and to compensate for large drag coefficients due to the inclusion of tether drag, the optimization algorithm pushes the design toward a flapped-like airfoil, particularly more visible at lower τ_{max} values. This appears to be in agreement with Makani's conclusion of the need to use two-element airfoils [69] as well as other efforts, e.g., by [30, 42, 73] to design and optimize multi-element airfoils.

Computational fluid dynamics results

In this section, CFD simulation results for the optimal airfoils ($\tau_{max} = 22\%$) with $\overline{A} = 0.1$ and 0.33 are presented.

Figure 4.16 shows the comparison between XFOIL and CFD results for $\overline{A} = 0.1$. As seen from Fig. 4.16a, the two c_l curves are quite different. According to XFOIL, the maximum c_l occurs at $\alpha = 5$ deg, whereas CFD results show that the maximum c_l is achieved at a significantly higher angle of 16 degrees. Despite this difference in the angle of attack, the values of $c_{l_{max}}$ obtained from XFOIL and CFD are comparable. As expected, the c_d curves also differ, with XFOIL's c_d values remaining relatively constant up until the stall point.

[2]It should be noted that no solution was found for $\tau_{max} < 22\%$ with the NSGA-II parameters considered in this study (see Table 4.1).

From CFD results, the optimal aerodynamic efficiency occurs at approximately $\alpha = 9$ deg where $c_l \approx 1.3$ is achieved. However, from Fig. 4.16d which shows the results from XFOIL, the optimal value of χ is achieved at $\alpha = 5$ deg. Here also, XFOIL predicts χ values several orders of magnitude higher than those obtained from CFD. The sharp drop of χ in the post-stall regime is also noticeable. From CFD results, the optimal aerodynamic efficiency occurs at approximately $\alpha = 9$ deg where $c_l \approx 1.3$ is achieved. However, from Fig. 14d, the optimal value of χ is achieved when $\alpha = 5$ deg. Here also, XFOIL predicts χ values several orders of magnitude higher than those by CFD. The sharp drop of χ in the post-stall regime is also noticeable.

Figure 4.17 shows the distribution of C_p over the optimal airfoil and the corresponding streamline plots at (a) $\alpha = -9$ deg, (b) $\alpha = 0$ deg, and (c) $\alpha = 5$ deg. As seen from the Cp plots, the distributions obtained from XFOIL and CFD match quite well at $\alpha = -9$ deg, except for the second half of the chord on the lower side of the airfoil. A significant adverse pressure gradient is present over nearly the first half of the chord length on the lower side of the airfoil, causing flow separation. This phenomenon is captured by both XFOIL and CFD analyses. Figure 4.17b shows flow separation and the formation of a recirculation region beneath the concave part of the lower side. By increasing the angle of attack, C_p values obtained via XFOIL and CFD become noticeably different. According to the CFD results, flow separation from the upper side of the airfoil occurred over the last 25-30% of the chord length while for reasons discussed previously, as seen from the C_p plot, no flow separation was captured by XFOIL. Figures 4.17d and 4.17f, clearly show the recirculation region near the trailing edge.

Figure 4.18 shows the comparison between XFOIL and CFD results for $\overline{A} = 0.33$. As seen from Fig. 4.18a, the two c_l curves are almost identical for $\alpha < 0$ while they become noticeably different at higher values of α. As with previous comparisons, XFOIL also tends

to overestimate the c_l values in this case. Figure 4.18b shows a dramatic increase of c_d past $\alpha \approx 7$ deg (from XFOIL) and $\alpha \approx 2$ deg (from CFD), suggesting the occurrence of stall whereas c_l shows little or no reduction around those angles of attack. As also seen previously, the aerodynamic efficiency plots obtained via CFD (Fig. 4.18c) and XFOIL (Fig. 4.18d) are different by several orders of magnitude. Based on CFD results, the maximum of χ is achieved at $\alpha \approx 1$ deg ($c_l \approx 0.9$) while based on XFOIL results, the maximum occurs at $\alpha \approx 7$ deg ($c_l \approx 1.7$).

Figure 4.19 shows the distribution of C_p as well as the flow field around the optimal airfoil with $\tau_{max} = 22\%$ at (a) $\alpha = -3$ deg, (b) $\alpha = 0$ deg, and (c) $\alpha = 3$ deg. At $\alpha = -3$ and 0 deg, no major flow separation occurs, as evidenced by the flow fields shown in Figs. 4.19b and d, which explains very good agreement between XFOIL and CFD C_p distributions, shown in Figs. 4.19a and c. At $\alpha = 3$ deg, on the other hand, flow separates from the upper side of the airfoil, as seen from Fig. 4.19f, which then explains the different C_p distributions obtained from CFD and XFOIL (Fig. 4.19e).

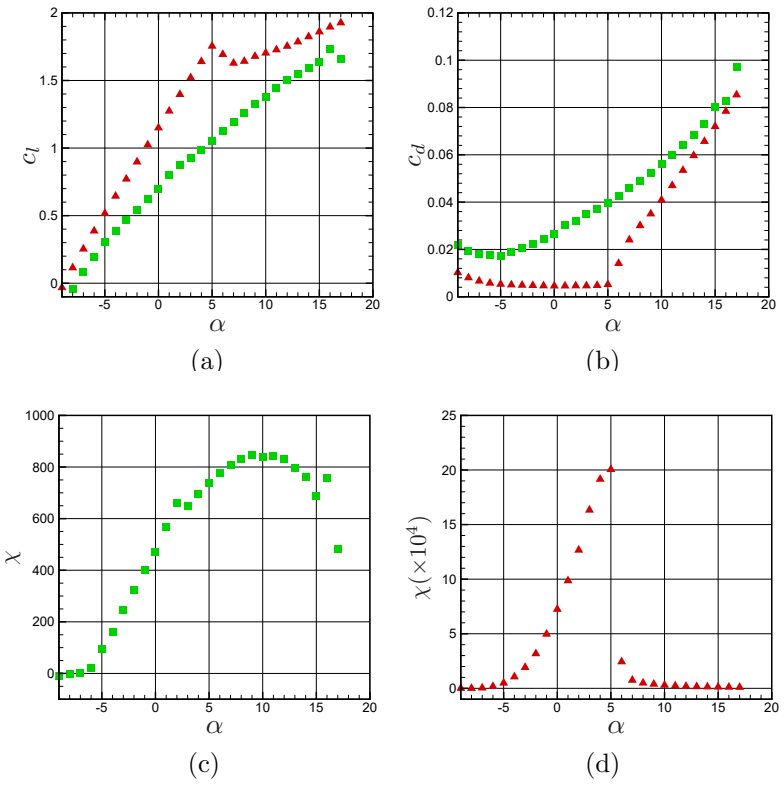

Figure 4.16: Variation of the (a) lift coefficient, (b) drag coefficient, (c)power coefficient obtained from CFD and (d)power coefficient obtained from XFOIL as a function of angle of attack for the selected optimal airfoil($\tau_{max} = 22\%$, $\overline{A} = 0.10$): XFOIL[▲] and CFD[■]

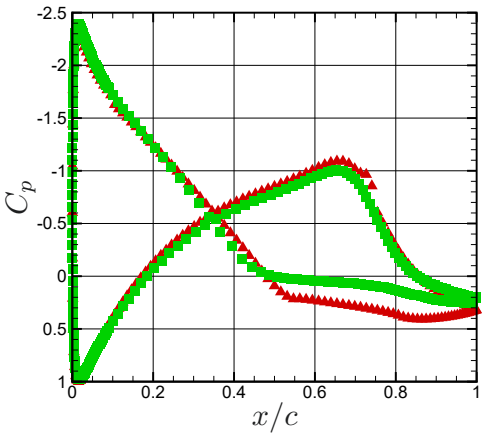

(a)

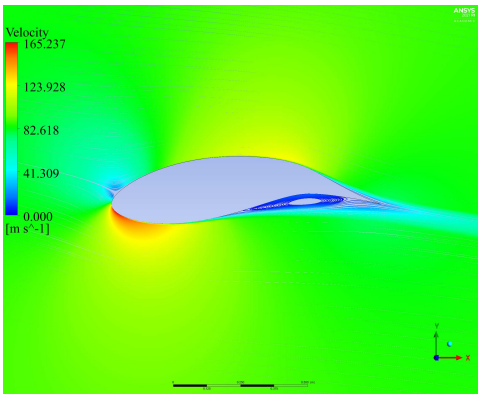

(b)

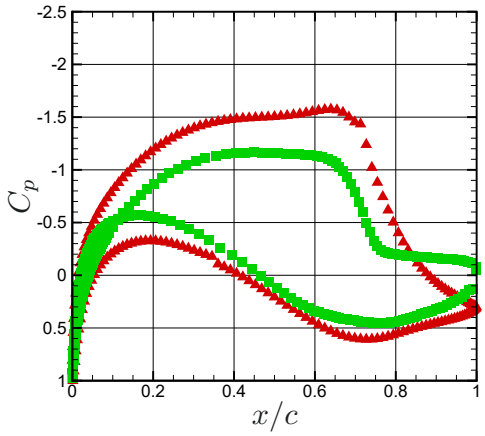

(c)

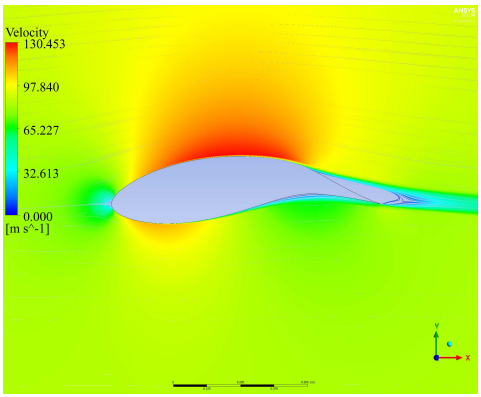

(d)

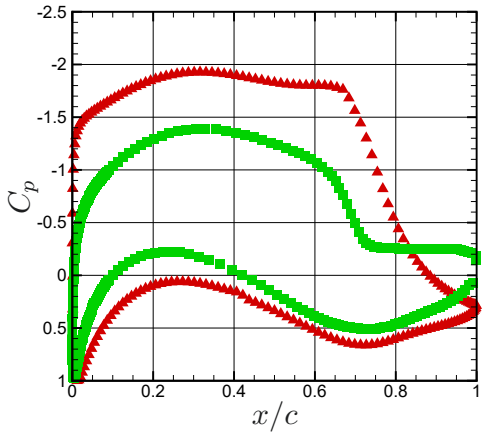

(e)

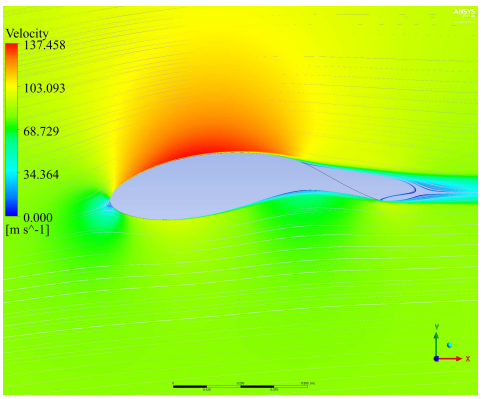

(f)

Figure 4.17: Distribution of C_p over the suction and pressure sides of the optimal airfoil and the corresponding streamlines with ($\tau_{max} = 22\%$, $\overline{A} = 0.10$) at (a,b) $\alpha = -9°$, (c,d) $\alpha = 0°$, and (e,f) $\alpha = 5°$: XFOIL[▲] and CFD[■].

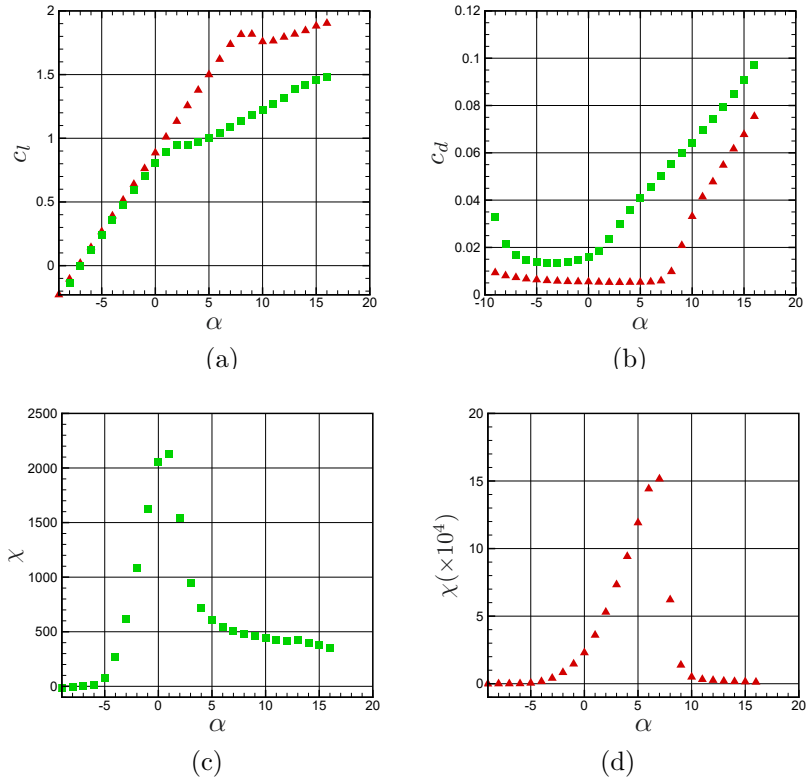

Figure 4.18: Variation of the (a) lift coefficient, (b) drag coefficient, (c) power coefficient obtained from CFD and (d) power coefficient obtained from XFOIL as a function of angle of attack for the selected optimal airfoil($\tau_{max} = 22\%$, $\overline{A} = 0.33$): XFOIL[▲] and CFD[■].

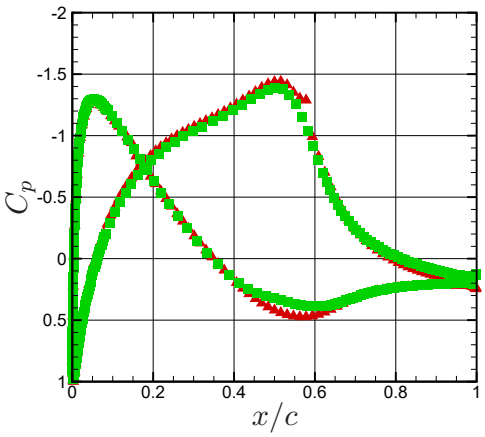

(a)

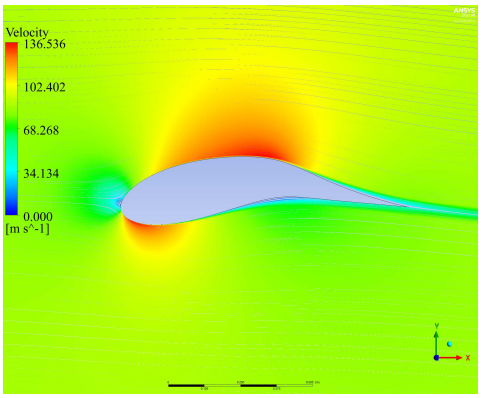

(b)

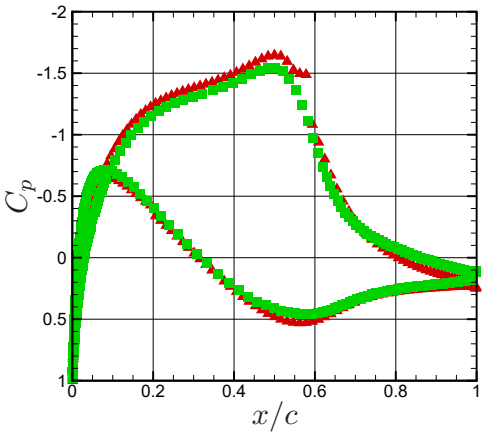

(c)

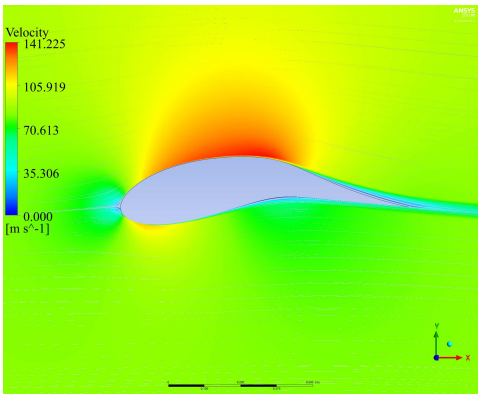

(d)

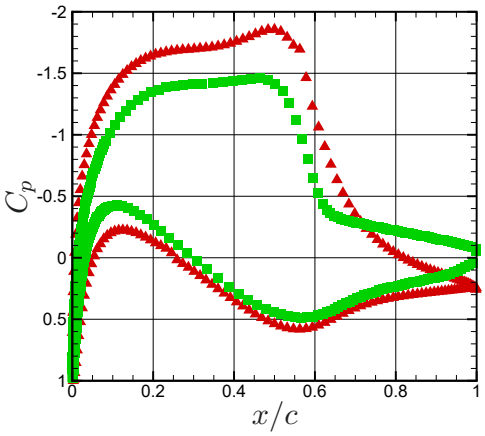

(e)

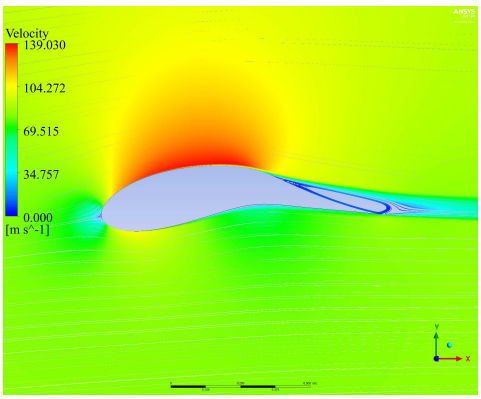

(f)

Figure 4.19: Distribution of C_p over the suction and pressure sides of the optimal airfoil and the corresponding streamlines with ($\tau_{max} = 22\%$, $\overline{A} = 0.33$) at (a) $\alpha = -3°$, (b) $\alpha = 0°$, and (c) $\alpha = 3°$: XFOIL[▲] and CFD[■].

4.3 Conclusion

Here in this chapter, we presented the optimization framework of airfoils applicable to airborne wind energy. The framework has four working blocks including, an optimizer, geometric builder, aerodynamic solver, and post-processor. Each section's responsibility is elaborated and the results were obtained. Three cases have been investigated with drag term modification. First, the results obtained where the drag term only includes viscous drag from XFOIL. The results show a significant improvement for thick airfoils compared to the ones in similar studies. This improvement owes to the airfoil parameterization.

Subsequently, we explored the impact of the kite aspect ratio on airfoil performance. Our analysis revealed that airfoils with sharp trailing edges facilitate sustained flow attachment, leading to improved aerodynamic performance. Computational Fluid Dynamics (CFD) simulations highlighted a recirculation region, reflected in C_p plots, contributing to higher lift coefficients. This phenomenon is similar to this study [74] where a recirculation region is created by utilizing a gurney flap to enhance the aerodynamic performance of the airfoil.

Leveraging our framework, we generated airfoils exhibiting superior power output potential, surpassing previous studies at equivalent maximum thickness ratios. This strategic design approach aims to mitigate induced drag, particularly evident in thin airfoils.

Furthermore, our investigation into the influence of tether drag unveiled airfoils featuring a flap-like trailing edge. Incorporating tether drag, a primary component of modified total drag, led to the development of these airfoils. Their design facilitates high lift coefficients, offsetting the drag induced by the tether. This underscores the potential of integrating multi-element airfoils within the optimization framework for future endeavors.

Chapter 5

Wing planform optimization

5.1 Introduction

Previous research on wing planform optimization has focused on refining the shape of the aircraft wing to enhance its aerodynamic performance. This process is iterative; starting with an initial wing shape, it involves modifying the design to improve the aerodynamic performance while ensuring that the final configuration meets the constraints. In aerodynamic analysis, designs are usually evaluated using high-fidelity and low-fidelity approaches within optimization frameworks. This level of aerodynamic solution refinement dictates the choice between multi-objective and single-objective optimization methods.

Aero-structural wing design optimization is performed by considering flexible wings and coupling aerodynamic forces and structural displacements. This approach allows for the simultaneous optimization of the external shape of the wing and the wing box structure, finding compromise between aerodynamic and structural performance. Candade et al. [75] developed an aero-structural model of a carbon composite wing without incorporating the fuselage. They investigated the preliminary design of kites, particularly considering the

bridle line system and its effects on the aeroelastic behavior of the wing. The computational model used in the study was sufficiently efficient for weight optimization during the early design stages, highlighting the potential for considerable improvements in airborne wind energy systems through structural optimization.

While aero-structural optimization is typically done for aircraft wing and crosswind kite power systems (CKPSs), some researchers also took control into account while optimizing wing planforms. Optimizing the wing planform in crosswind kite power systems involves with complex interactions between unsteady flow, flexible structure, and control. As a result, some researchers use high-fidelity tools to resolve these interactions [76].

Gusts and unsteadiness during CKPS flight make control systems a critical component. Conventional control surfaces, particularly present in drag mode kites, and changing the reel-in speed, particularly in lift mode kites, are two general solutions for controlling the kite in an unsteady flight. One novel concept was presented by Fasel et al. [29] who implemented the shape morphing wings to fulfill the control criteria of the kites. During the flight, the wing and airfoil shapes are altered to optimize the performance across different flight conditions. This approach leverages compliant structures and active gust load alleviation through morphing, which results in a lighter wing and an expanded flight envelope, thereby increasing the power production of AWE systems.

5.2 Methodology

Here, a similar methodology used in the airfoil optimization study (Chapter 4) is adopted to find the optimal wing planforms; see Fig. 5.1. The optimization framework consists of four blocks. The geometry builder is the OpenVSP geometry definer, while the aerodynamic solver is VSPAERO. The post-processor utilized here to calculate the objective functions

and to pass them to the optimizer is similar to the one used previously in Chapter 4.2.

Two objective functions are employed to consider the structural and aerodynamic aspects of the wing. These objective functions are inherently conflicting, meaning that an improvement in one of the objective functions typically results in the degradation of the other.

In Chapter 4, airfoil's maximum thickness was used as the objective function to represent the structural aspect of the airfoil. However, in this chapter, three-dimensional wings involving multiple structural variables, such as wing area and span, are considered. A key variable that links these two variables is the wing aspect ratio which is selected as the structural objective function. The wing aspect ratio is a suitable candidate for this purpose as it inherently reflects the three-dimensional nature of the wing. There are two primary ways to change the aspect ratio of a wing: varying the wing span and/or the chord length. While increasing the aspect ratio, as outlined below, can enhance aerodynamic performance, it also

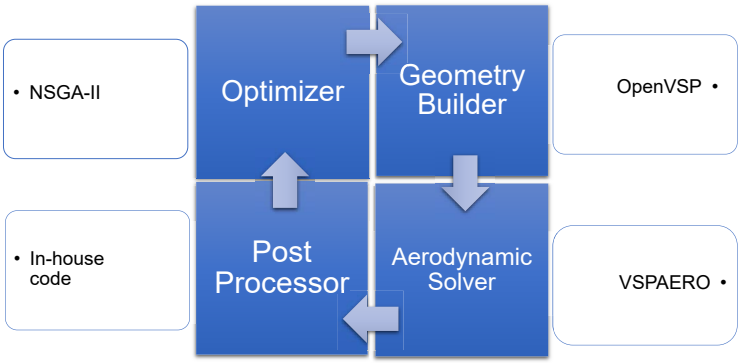

Figure 5.1: Schematic of optimization framework including four major components. The names of the codes or software are shown in each block.

has structural implications. A higher aspect ratio can lead to greater bending moments on the wing, making it more susceptible to structural stress. Additionally, an increased aspect ratio raises the moment of inertia, which in turn can reduce the wing's maneuverability.

The total drag of the wing consists of two major contributions, i.e., profile drag c_d and induced drag C_{D_i}:

$$C_D = c_d + C_{D_i}, \tag{5.1}$$

where the profile drag includes form drag (i.e., drag due to the shape of the airfoil) and skin friction drag (i.e., drag due to viscosity of the flow traveling over the surface of the wing).

Here, the interference drag, which is due to interactions between different parts of the kite, is not considered as the focus is solely on a single wing. The skin friction drag is approximated by the flat plate definition and form drag by the factor equation available in OpenVSP. Similarly, the induced drag is obtained using Eq. 5.2, where aspect ratio, AR, and Oswald span efficiency, e, are directly involved.

$$C_{D_i} = \frac{C_L^2}{\pi ARe}. \tag{5.2}$$

The shape of the wing planform will be dictated by the aspect ratio and Oswald span efficiency. The Oswald span efficiency is linked to the lift distribution over the wing:

$$e = \frac{1}{1+\delta}, \tag{5.3}$$

where $\delta = \sum_{n=2}^{N} n \left(\frac{A_n}{A_1}\right)^2$. The A_n coefficients are from the general circulation distribution, where it is assumed this distribution is a Fourier sine series. Interested readers are referred to [77].

Now, the two objective functions to be implemented in the optimization framework are

outlined. As mentioned earlier, one objective function should represent the aerodynamic performance of the kite while the other objective function, which conflicts with the first one, should represent the structural aspect of the wing. For the first objective function, the inverse of the aerodynamic efficiency of the kite is selected since the optimizer needs to minimize the objective function. Thus, the first objective function is considered to be $1000/f_P$, where f_P has a similar definition as the one used in Chapter 4 airfoil and is given in Eq. 5.4; however, note the difference between lift and drag coefficients for airfoils and wings. The wing aspect ratio is also selected as the second objective function.

$$f_P = \sum_{k=1}^{8} w_k C_{L_k} \left(\frac{C_{L_k}}{C_{D_k}} \right)^2, \tag{5.4}$$

$$f_S = AR. \tag{5.5}$$

.

The conflicting nature of the two objective functions is explained as follows. An increase in the wing aspect ratio, increases f_S while decreases the induced drag and thus the total drag. The reduction of the total drag is beneficial and is expected to increase f_P and in turn reduces $1000/f_P$. Thus the increase in the one objective function decreases the other one.

5.3 Verification

5.3.1 Objective functions

It is well-known that, among all planforms, elliptic wings have the minimum induced drag and thus maximum glide ratio, C_L/C_D, for a given C_L. This fact is used to verify the wing planform optimization framework presented in the previous section. The glide ratio is

Table 5.1: Range of lift coefficients and corresponding weights considered in the verification of the wing planform optimization framework.

Parameter	$k=1$	2	3	4	5	6	7	8
$C_{L,k}$	0.5	0.6	0.7	0.8	0.9	1	1.1	1.2
w_k	0.05	0.1	0.1	0.1	0.1	0.15	0.2	0.2

obtained over a range of lift coefficients which correspond to different flight conditions:

$$f_G = \sum_{k=1}^{8} w_k \left(\frac{C_{L_k}}{C_{D_k}} \right), \tag{5.6}$$

where C_{L_k} and w_k are provided in Table 5.1.

Considering a minimization problem, the first objective function is defined as $100/f_G$.

The second objective function is defined as the wing aspect ratio:

$$f_S = AR. \tag{5.7}$$

For simplicity, no sweep or twist is considered along the wing, and NACA 2412 is assumed to be the airfoil section, from the root to the tip. Since the airfoil is kept the same along the span, the zero-lift drag contribution remains constant, and drag minimization is determined by the induced drag.

5.3.2 Geometrical definition of the wing

The wing is characterized by 9 design variables as shown in Fig. 5.2. The chord length is determined at 5 stations, including the root, c_r, three in the middle, c_2, c_3, and c_4, and the tip of the wing, c_t. Additionally, the wing span is divided into 4 segments with lengths b_1,

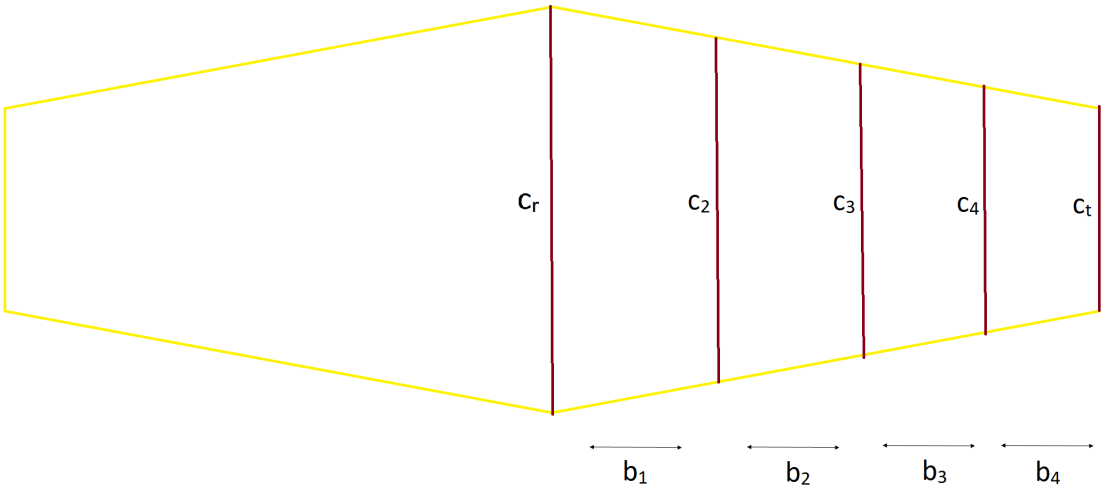

Figure 5.2: Variables used to define the geometry of the wing planform.

b_2, b_3, and b_4. Equation 5.8 lists these variables with their lower and upper bounds.

$$\begin{cases} c_r \in [0.001, 0.1289] \\ c_2 \in [0.001, 0.1289] \\ c_3 \in [0.001, 0.1289] \\ c_4 \in [0.001, 0.1289] \\ c_t \in [0.001, 0.1289] \\ b_1 \in [0.05, 0.95] \\ b_2 \in [0.05, 0.95] \\ b_3 \in [0.05, 0.95] \\ b_4 \in [0.05, 0.95] \end{cases} \tag{5.8}$$

For clarity and consistency, all the variables were normalized with respect to the half-span $b/2$, b being the tip-to-tip wing span. Small non-zero values were considered for the lower bounds of the variables to avoid zero chord lengths or spans. The upper bound for b_1 to b_4 was set to 95% of the half-span. It is also evident that $b_1 + b_2 + b_3 + b_4 = b/2$. In addition, to sweep over a sufficiently wide design space, the wing span was set to be in the range 24 m $< b <$ 36 m.

5.3.3 Flow conditions

The flow condition that has been utilized is adopted from similar studies on CKPSs [28]. The freestream Reynolds number was set to $Re = 6 \times 10^6$ which with a constant density of $\rho = 1.225$ kg/m^3 and viscosity of $\mu = 1.7894 \times 10^{-5}$ N·s/m^2 yields a freestream velocity of $V_\infty = 87.6$ m/s. Also, the reference surface area, the one used in the definition of lift and drag coefficients, is equal to the total surface area of the wing. The surface area is calculated from the parameters defined as the input design variables in the OpenVSP code separately.

5.3.4 NSGA-II settings

A summary of the optimizer settings is shown in Table 5.2. The number of population is set to 40 and the number of generations is set to 200. The selection function is set to be "tournament," and the crossover fraction is 0.4. Given the constraint on the total span of the wing, a constraint-based mutation is utilized. Additionally, the Pareto front population fraction is set to 0.4.

Moreover, the *SaveOut* function has been developed and integrated into the optimization framework to save the last generation. This approach is adopted for instances where results may not be returned to MATLAB via the command window, necessitating a restart of the optimization framework. Utilizing the saved results from *SaveOut* as the initial population

will lead to enhanced computational efficiency.

Table 5.2: NSGA-II setting parameters used in the verification of the wing optimization framework.

Parameter	**Value**
Population size	40
Number of generations	200
Tournament size	2
Crossover fraction	0.4
Pareto front fraction	0.45

5.3.5 Results

Figure 5.3 shows the Pareto optimal front. The population distribution covers a range of aspect ratios, spanning from typical values for conventional aircraft ($12 < AR < 20$) to high and very high aspect ratios ($AR > 20$), which are suitable for rigid crosswind kites.

As an example, Fig. 5.4 shows the wing planforms for aspect ratios of $AR = 17.45$, 21.47, and 25.82. These aspect ratios were selected based on the present study's focus on crosswind kites. Visually speaking, the planforms obtained from the optimization framework (called 'Verification') closely resemble the corresponding elliptic planforms. As seen, the chord length is monotonically decreasing from the root to the tip, suggesting a trapezoidal wing planform. Also, the results show that the span of middle sections is comparatively smaller than those at the root or tip.

In addition, a parameter is defined to quantitatively measure the resemblance between the planform obtained from the optimization framework and the corresponding elliptic planform:

$$E_s\% = \frac{|S_{trap} - S_{elliptical}|}{S_{elliptical}} \times 100, \tag{5.9}$$

where S_{trap} represents the surface area of the trapezoidal wing obtained from the optimization faramework, and $S_{elliptical}$ is the surface area of the elliptic wing with the same span.

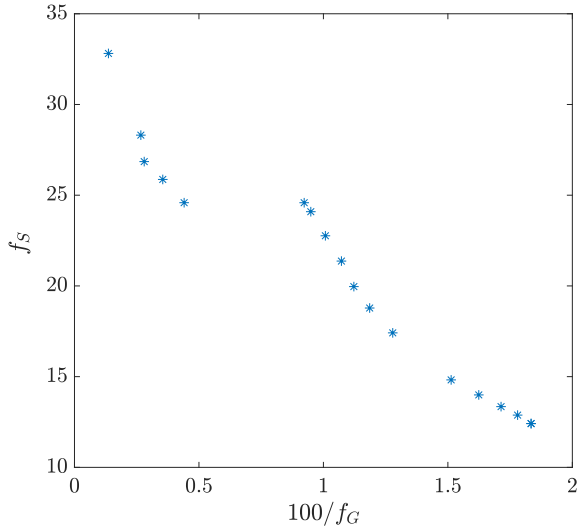

Figure 5.3: Pareto optimal front obtained from optimization framework where two objective functions are as follows: $100/f_G$ and $f_S = AR$.

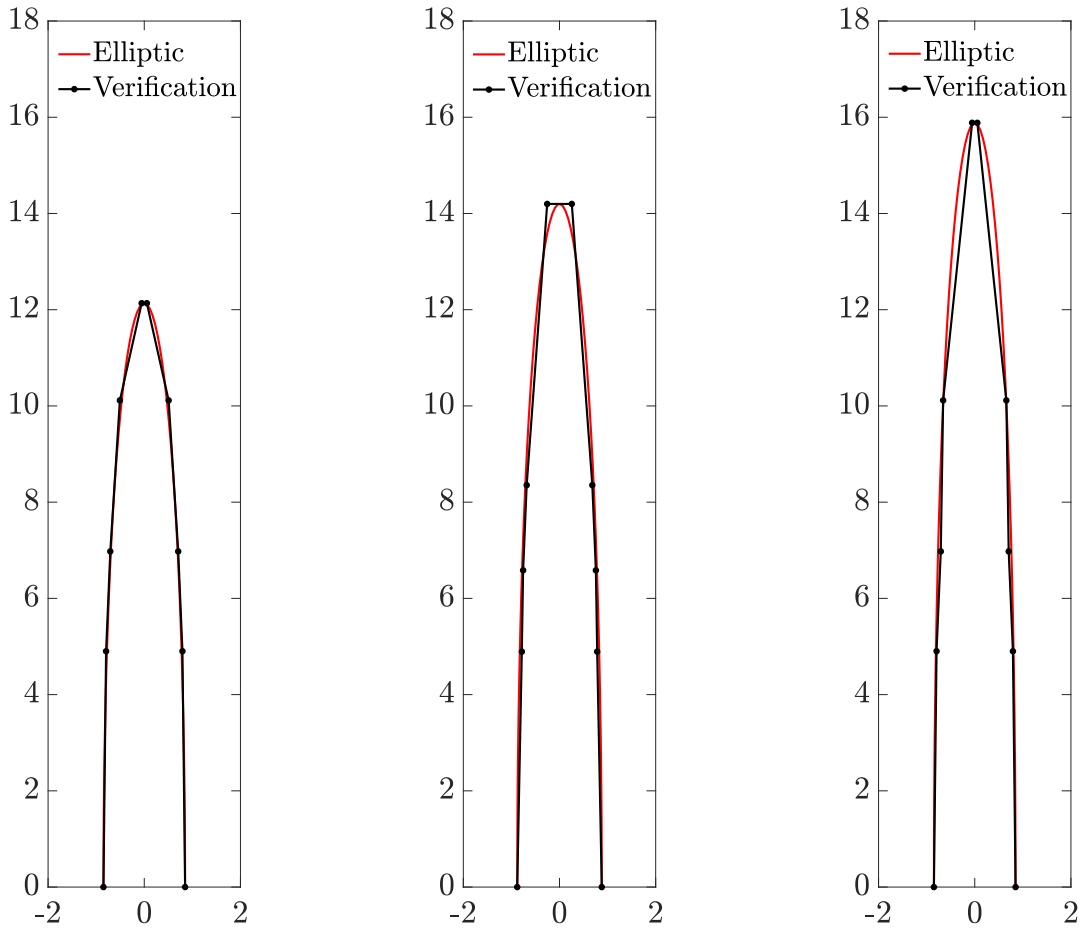

(a) $AR = 17.45$ (b) $AR = 21.47$ (c) $AR = 25.82$

Figure 5.4: Comparison of the wing planforms obtained from optimization, intended for the verification of the framework, with elliptic wings with the same total span. All the values are in meters.

Table 5.3: Numerical values of the variables (i.e., chords and spans) used for defining wing planforms for the wings shown in Fig. 5.4 and the corresponding values of E_s.

AR	c_r	c_2	c_3	c_4	c_t	b_1	b_2	b_3	b_4	E_s
17.45	0.113	0.105	0.094	0.087	0.007	0.326	0.138	0.209	0.134	4.32
21.47	0.117	0.104	0.101	0.091	0.034	0.326	0.112	0.118	0.389	4.25
25.82	0.113	0.106	0.094	0.088	0.007	0.327	0.138	0.209	0.385	7.71

Table 5.3 provides the numerical values of the variables used for defining the wing planform and the corresponding values of E_s for the planforms shown in Fig. 5.4. As seen from the table, the relative error between the surface areas, E_s, is below 10% for all three planforms. The relative error generally increases with the aspect ratio. This trend may be attributed to the limited number of stations used to discretize the wing span, which may not accurately capture the lift distribution over the wing. On the other hand, increasing the number of stations will lead to a significant increase in computational costs, introducing a new challenge. Thus, the number of stations was limited to 4.

5.4 Numerical results

Following Section 5.3.1, design variables, flow conditions, and the optimizer setting are adopted to solve the optimization problem described in Section 5.2. Figure 5.5 shows the Pareto front obtained from the optimization framework. As expected, the increase in aspect ratio will lower $1000/f_P$, which means an increase in the aerodynamic efficiency, f_P. As seen, there are some regions where the optimizer was unable to find solutions. This may be attributed to the limited population size used in the optimization. It is expected that by increasing the population size, the Pareto front becomes well distributed. However, by increasing the population size, the computational cost increases prohibitively.

Figure 5.6 shows some sample wing planforms obtained from the Pareto optimal front. The wings have aspect ratio of $AR = 15.19$, 19.27, 23.47, and 29.37. As seen, the optimal planforms and the corresponding elliptical wing planforms are in good agreement. From

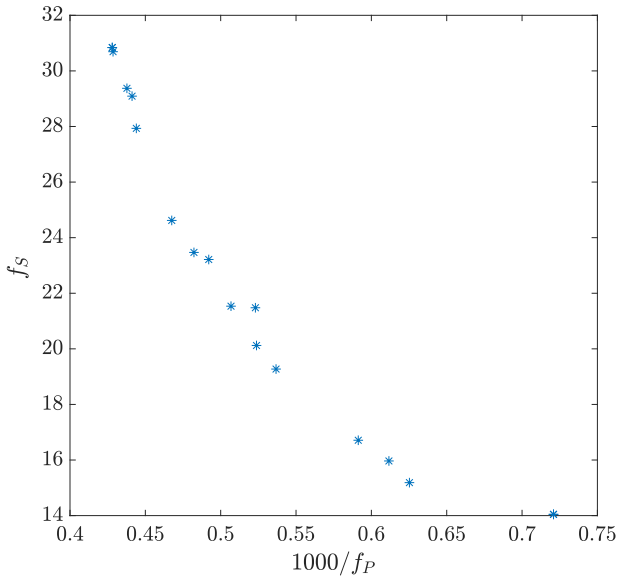

Figure 5.5: Pareto optimal front obtained from optimization framework where two objective functions are as follows: $1000/f_P$ and $f_S = AR$.

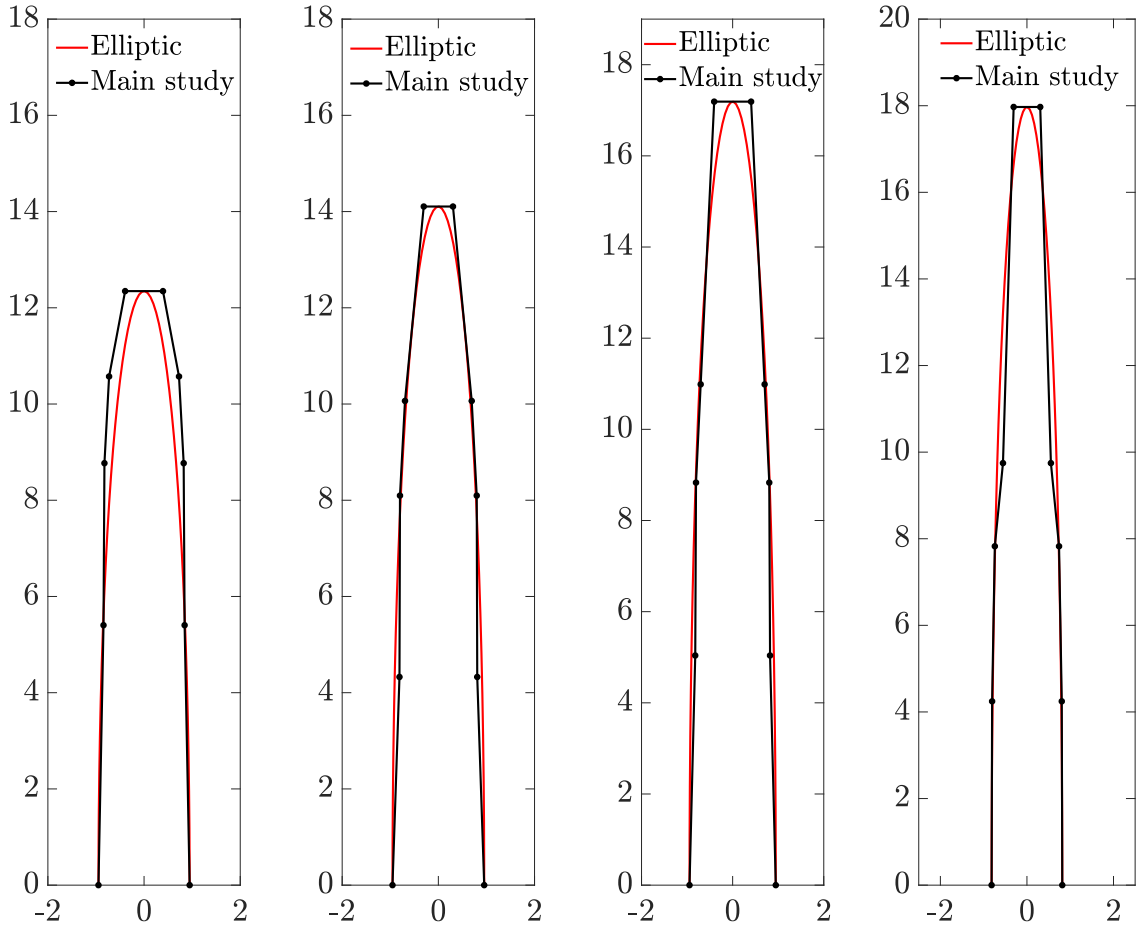

(a) $AR = 15.19$ (b) $AR = 19.27$ (c) $AR = 23.47$ (d) $AR = 29.37$

Figure 5.6: Comparison of the wing planforms obtained from optimization for the main study, comparing with the corresponding elliptic wing with the same total span. The values of c_r, c_2, c_3, c_4, c_t, b_1, b_2, b_3, and b_4 are dimensional.

Table 5.4, one can also confirm the agreement quantitatively. For the higher aspect ratio wings, the relative error of the surface area is below 5%.

One may attempt to explain the above observations analytically. Considering Eqs. 5.1, 5.2 and 5.4, $C_{L_k}(C_{L_k}/C_{D_k})^2$ can be re-written as

$$C_{L_k}(\frac{C_{L_k}}{C_{D_k}})^2 = \frac{C_{L_k}^3}{(c_d + \frac{C_{L_k}^2}{\pi ARe})^2}. \tag{5.10}$$

Table 5.4: Geometrical properties, distribution of the chords and span of each section, of the wing platform shown in Fig. 5.6. The parameter E_s 5.9 shows the difference in the surface area of the trapezoidal wing and the ideal elliptical wing.

AR	c_r	c_2	c_3	c_4	c_t	b_1	b_2	b_3	b_4	E_s
15.19	0.126	0.112	0.109	0.097	0.052	0.360	0.224	0.120	0.118	9.18
19.27	0.127	0.107	0.106	0.092	0.040	0.288	0.251	0.131	0.269	2.28
23.47	0.126	0.109	0.107	0.093	0.054	0.335	0.252	0.143	0.413	1.49
29.37	0.108	0.107	0.098	0.073	0.040	0.283	0.238	0.128	0.548	4.60

From Eq. 5.10, for given C_{L_k}, c_d (airfoil section), and AR, the efficiency factor is maximized when e is maximized. It is well-known that the maximum value of the Oswald efficiency factor e, i.e. $e = 1$, is achieved via the elliptic planform. In Eq. 5.6, the objective function is dependent on e^{-1} while in Eq. 5.10, it is dependent on e^{-2}. It is expected that the latter function approaches the minimum faster than the former.

5.5 Conclusion

In this chapter, a wing planform optimization framework was developed for AWE applications. The results in the verification section showed that for maximizing the lift-to-drag ratio, the wing planform would converge to an elliptical planform.

Next, the maximization of the aerodynamic efficiency was studied. Once again, both qualitatively and quantitatively, the optimal planforms resembled the elliptical planform. This was particularly evident for the wings with higher aspect ratios. A higher population size is expected to improve the quality of the results. However, this is deferred to a future study. Also, a more rigorous measure should be defined for quantifying the geometric similarity between an optimal planform and the corresponding elliptical planform.

Chapter 6

box-wing airfoil optimization

6.1 Introduction

This chapter explores the optimization of airfoils in box-wing configurations. Extensive research by scholars such as Munk [78], Prandtl [15], Gall and Smith [79], and Norton [80] has investigated the biplane concept and the influence of design parameters on its performance. The primary objective of the box-wing design is to minimize the induced drag of conventional wings, i.e., monoplane configuration due to vortex shedding in the wing tip at conventional wing designs. The box-wing, when viewed from the front, presents a shape resembling a box formed by the forward and aft wings. Detailed discussion of the design aspects related to box-wing will be addressed in Section 6.2.1.

The configuration of a box-wing has two wings connected via vertical fins at the wing tip section. The purpose of vertical fins is to stabilize the wing and reduce the impact of tip vortices. In contrast, a biplane can have wings that are either attached or separated and may include multiple wings with a more complex design. Although the box-wing concept is not extensively covered in existing literature, this study aims to investigate the airfoils located

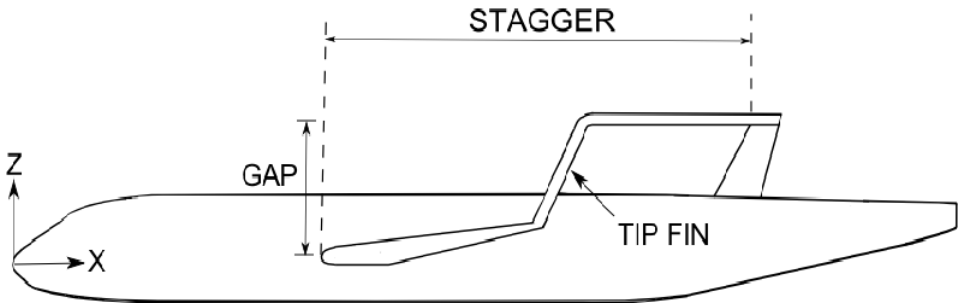

Figure 6.1: The schematic of box-wing from the side view showing the gap and stagger as two of the main variables in box-wing geometry [14].

in the mid-section of the box-wing applicable to AWE. To support this analysis, a review of the literature on biplane configuration will be beneficial as the fins effect are neglected.

Munk [78] carried out a study that closely evaluated the aerodynamic characteristics of biplane wings. The wing design characteristics and the related equations were thoroughly examined as a part of this investigation. A few examples were given, accounting for the effects of stagger, chord, decalage, and gap. In addition, the impact of three-dimensional flow was investigated by considering the lateral flow's movement. The longitudinal and vertical flows are discussed in this study. The box-wing geometrical parameters are shown in Fig.6.1. Munk [78] presented two important general laws regarding biplanes:

- Induced drag of any systems, does not depend on the longitudinal coordinates. This means wings with the same front view will experience the same total induced drag. This is true in an unstaggered system.

- The drag induced from wing 1 to wing 2 is equivalent to that induced from wing 2 to wing 1 in an unstaggered system.

Based on the results of this work, it becomes essential in biplane research to incorporate these two laws into the design and optimization process. These rules are regarded as simplifying hypotheses that facilitate the development of new concepts and designs.

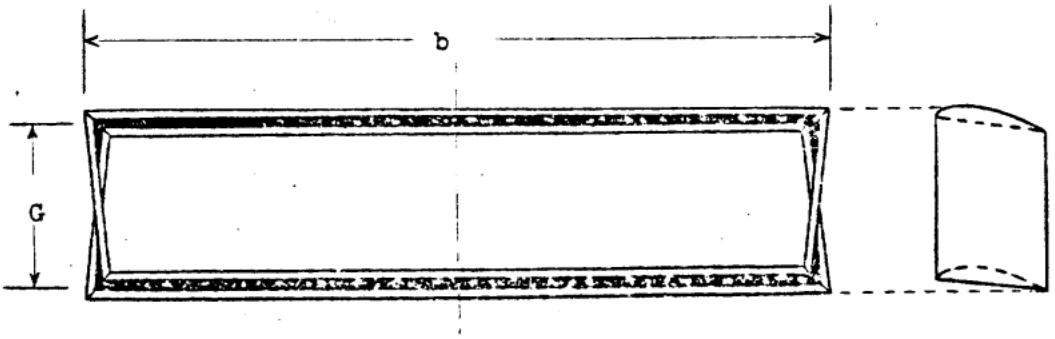

Figure 6.2: The schematic of the wing proposed by Prandtl in his study [15] as the best wing system.

Prandtl [15] developed the total drag produced by multiplane configurations and examined them in this study. After conducting research on the effects of the number of wings on drag, he determined that a biplane creates less drag than a monoplane. He emphasized that this is an accurate conclusion in cases where the wing span and overall load of the monoplane and biplane are equal. Finally, he proposed the biplane as the optimal wing configuration among the triplane, biplane, and monoplane options. The wing system proposed by Prandtl is shown in Fig.6.2.

Other studies like [80] investigate the effect of stagger on the aerodynamic performance of the biplane. They concluded that a positive stagger, i.e. the upper wing is placed in a forward position compared to the lower wing, causes an increase in aerodynamics efficiency, and the maximum lift coefficient, and pushes the center of pressure more forward.

In addition to early theoretical studies, there are some experimental studies concerning the design of biplanes. Gall and Smith [79] investigated the effect of adding winglets to the biplane configuration. They included theoretical and experimental methods to show that adding winglets can increase the aerodynamic efficiency and lift-to-drag ratio. Furthermore, the lift-curve slope and maximum lift coefficient are reported to increase with the presence of winglets. It is worth noting that adding winglets to a biplane resembles the shape of a

box-wing.

There are other studies related to box-wing; however, few of them apply to the Airborne Wind Energy (AWE) industry. For example, in the thesis by Eijkelhof et al., [41], an automated framework was developed where high-fidelity, i.e., Openfoam, and low-fidelity, i.e., APAME, aerodynamic solvers were utilized to study the box-wing implementation in AWE. Several parametric studies concerning the design feature of the box-wing were carried out including the sensitivity of the lift coefficient to the fore-wing area, wingspan, gap, stagger, and taper ratio of the wings were investigated through a series of parametric studies. Additionally, simple optimization research was conducted utilizing the parametric study results to determine the box-wing with the highest lift coefficient and lowest weight.

In conclusion, it seems that the aerodynamic optimization of the box-wing is crucial for maximizing the aerodynamic performance. Consequently, in this study, an optimization framework concerning the airfoils implemented in box-wing configurations applicable to the AWE industry is developed. In the following sections, the methodology, and results obtained from this optimization framework are presented. Furthermore, the validation and verification of the MSES with the application of box-wing are presented in Chapter 3.

6.2 Methodology

The methodology of the box-wing optimization is presented. The following subsections describe the framework's general background, objective functions, and different penalization methods.

6.2.1 General description

Here, the optimization framework is described in detail. Four major components make up the optimization framework, as shown in Fig. 6.3. The optimizer is the first working block. A geometry builder block will come next. The third block is an aerodynamic solver, and finally, a post-processor completes the optimization task. There are both differences and similarities between this framework and the one devised in the single airfoil optimization framework, which will be discussed in the relevant sections.

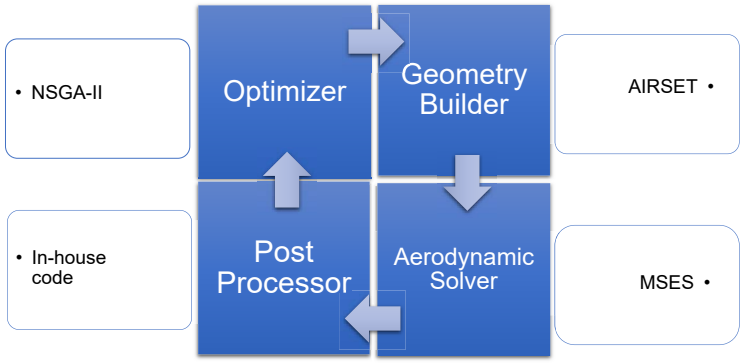

Figure 6.3: Schematic of working blocks in the optimization framework for the airfoils applicable to box-wing designs.

The NSGA-II code which is included in the optimizer block has been verified; the results are shown in Appendix A. The ability to identify the optimal population without requiring an exhaustive procedure is one of the major reasons for employing NSGA-II. While it is true that this kind of optimization method has a high computational cost, NSGA-II is among the most reliable techniques for resolving such challenging problems faced by NSGA-I. It is a suitable option for the primary optimizer since it can identify a decent population distribution and the optimal Pareto front without any need for special adjustments, like the one in NSGA-I, e.g., adjusting the sharing parameter which determines diversity among final results.

NSGA-II starts with a random population, created by MATLAB's random function, tailored to design variable bounds. The design variables that were selected randomly by NSGA-II are translated into a set of coordinates for the geometry builder. Rather than relying on some arbitrary parameters, which are seen in the Class-Shape Transformation (CST) function, the optimizer makes decisions based on a set of physical properties, which is inherently in the IGP method's definition. Afterward, these coordinates will be saved in a file ending in .dat, which can then be read by the aerodynamic solver.

The aerodynamic solver, MSES, is located in the third block. MSES comprises multiple sub-programs, outlined in Section 3.4, and are utilized in this aerodynamic analysis. The *AIRSET* program, which creates the blade file and determines airfoil locations, receives two airfoil files. The created blade file will be utilized next in *MSET*.

In *AIRSET*, the stagger-to-chord and gap-to-chord ratios are set to 0 and 1, respectively. Additionally, the chord lengths of the upper and lower airfoil are fixed at 1 m. These parameters are held constant throughout the optimization to avoid experiencing additional computational costs.

In *MSET*, the mesh for the aerodynamic solver will be created. First, the blade will be

automatically read. Next, the angle of attack at which the grid will be generated can be specified by entering "1" in the command window. Additionally, the streamlines surrounding the configuration are generated by selecting this option. Next, the grid around the airfoils will be initialized and the cell spacing will be generated using "2" from the menu. To smooth out the grid and eliminate all the kinks and overlaps, "3" will be selected from *MSET*'s menu.

Finally, entering "4", and "8" write the grid in files with *mdat* and *gridpar* prefixes where *mdat* file contains the grid coordinates and *gridpar* contains grid parameters, such as the angle of attack and grid spacing. The main solver will use these files to find the aerodynamic coefficients. In addition, the user can control the downstream and upstream distances from airfoil configurations.

The specification file should be created when the *MSET* instructions are finished. The list of angles of attack that *MPOLAR* is sweeping over are contained in *MSPEC*. To ensure that the lift coefficients shown in Table 6.1 can be obtained, a broad range of angles of attack should be chosen. However, caution should be exercised since MSES usually diverges at high angles of attack close to stall.

The angle of attack used in the optimization ranges from -6 to 10 degrees. This range was determined through iterative testing, ensuring that convergence issues were avoided. Since the standard *MSES* code cannot sweep over a specific range of angles of attack, it is not used. Alternatively, a sub-program named *MPOLAR* is utilized. *MPOLAR* can read both the blade file, the grid specification files, i.e., *mdat* and *gridpar*, and the flow specification file, created for MSES to sweep throughout the angle of attack range as indicated in the *MSPEC* file.

The flow specification, contained in a separate file needs to be changed before *MPOLAR* is executed. This file, for instance, looks like the one shown in Fig. 6.4. To learn more, interested readers can refer to [6], which contains the MSES user manual.

```
3 4 5 7 20
3 4 6 7 20
0.75    0.80   0.0    | MACH   CL     ALFA
 3      2             | ISMOM  IFFBC
5.0E6   9.0           | RE     ACRIT
0.1     0.1           | XTRS   XTRP
0.97    1.0           | MCRIT  MUCON
1       1             | ISMOVE ISPRES
6       0             | NMODN  NPOSN
```

Figure 6.4: Commands read by MSES in order to complete a simulation.

The values of the Reynolds number and Mach number are edited in each file of the flow specification. They are set to be $M_\infty = 0.257$ and $Re = 6 \times 10^6$. Furthermore, the N_{crit} criteria is set to be 9.0 and the flow transition type is set to be free. These values are in line 3 and 5 as shown in Fig. 6.4.

Next, *MPLOAR* will be executed from Matlab's command window. The aerodynamic results will be read and stored in a different file with a .txt extension so that the post-processor can examine them at a later time. The aerodynamic table that was acquired from *MPOLAR* will be read by the post-processor to compute the objective functions in the next step. Two basic penalization strategies are also taken into consideration (see Section 6.2.3). In the related section, the objective functions will be covered later. Due to time limitations, the results for removal penalization will be presented and the partial penalization needs more investigation.

After the post-processor finishes and generates the results, these results will be transferred to the optimizer block to do the crossover and mutation procedure to create the next generation. After creating the new generation, the procedure will be repeated as described above.

6.2.2 Objective functions

Here, similar to single airfoil optimization, two conflicting objective functions should be devised. As mentioned in Section 4.2, objective functions related to the aerodynamics and structure suit this purpose.

The structural objective function should consider both airfoils. The maximum thickness of one of the two airfoils may not be sufficient. Instead, the summation of the maximum thickness of the two airfoils is utilized:

$$f_T = \tau_{max_1} + \tau_{max_2} \tag{6.1}$$

where τ_{max_1} and τ_{max_2} represent the maximum thickness ratio of the first and second airfoil, respectively for their respective chord length which is $c = 1m$.

It is noted that, for simplicity, in the present optimization studies, the chord length of the two airfoils is kept fixed and equal. Since a minimization problem will be solved, the actual objective function will be $-f_T$.

The second objective function is the aerodynamic-related objective function. A similar objective function as utilized in the single airfoil optimization study (Chapter 4) is considered in the box-wing optimization study. However, a different range of lift coefficients should be considered because two airfoils are involved in the present optimization. It should be noted that in MSES, the total aerodynamic forces generated over a multi-element airfoil or multiple airfoils are normalized with respect to the chord length of one of the airfoil sections (not the summation of the chord lengths). For example, the overall lift coefficient of the box-wing is defined as

$$c_l = \frac{2L'}{\rho_\infty V_\infty^2 c}, \tag{6.2}$$

Table 6.1: Range of lift coefficients and corresponding weights considered in numerical studies in the box-wing optimization study.

Parameter	$i=1$	2	3	4	5	6	7	8
$c_{l,i}$	1	1.2	1.4	1.6	1.8	2	2.2	2.4
w_i	0.05	0.1	0.1	0.1	0.1	0.15	0.2	0.2

where L' is the total lift (per unit length) generated by the box-wing, and c is the chord length of the reference airfoil.

Thus, the second objective function, that is related to the aerodynamics of the box-wing, is defined as

$$f_P = \sum_{i=1}^{8} w_i c_{l_i} (\frac{c_{l_i}}{c_{d_i}})^2, \tag{6.3}$$

where the values of the lift coefficients c_{l_i} and the corresponding weights w_i are given in Table 6.1.

Since this objective function should also be set for the minimization, $1000/f_P$ is utilized.

6.2.3 Penalization methods

There are two types of penalization methods that affect aerodynamic results. We named them the removal penalization method and the partial penalization method. As it is evident the angles of attack were limited due to convergence difficulty in MSES. This indicates that the lift coefficient's lowest and maximum values might not fit the table's lower and upper bounds, as shown in Table 6.1. Furthermore, we found some impractical numbers in the order of 10^3, which suggests that the interpolation used in the internal code may have extrapolated the lift-to-drag ratio values inaccurately. Once more, the reason for this incorrect extrapolation procedure is that the lift coefficient's minimum and maximum values do not fall between the lower bound (which is $c_l = 1$) and the upper bound (which is $c_l = 2.4$). Two approaches can be proposed to address this problem and speed up the

optimization process.

First, a method for removal penalization can be developed. Under this procedure, the in-house code is in charge of determining whether the aerodynamic results' lowest lift coefficient value is less than $c_l = 1$ **and** whether its maximum value is more than $c_l = 2.4$. The removal procedure will be applied when the selected lift coefficients table does not fit the range of lift coefficients obtained from MSES, i.e., $c_{l_{max,t}} > 2.4$ and/or $c_{l_{min,t}} < 1$ where $c_{l_{max,t}}$, $c_{l_{min,t}}$ are maximum and minimum values of lift coefficient in the table. If this condition is met, we designate the objective functions as equivalent to 10. By using this approach, the Pareto front and the repository members—who are the potential members of the future population—will be free of these airfoils. Additionally, by allocating such large values, the NSGA-II will be able to generate the following population safely without taking these airfoils into account.

It is important to note that this kind of analysis takes into account both lower and upper bounds and does not interfere with the NSGA-II process. The NSGA-II has no issues when the distance is large enough to guarantee that the population's members are smaller than those that were eliminated by giving the fitness function large values because, as the results section will show, the majority of the population is located roughly between $-0.7 < -f_S < -0.3$ and $0.05 < 1000/f_P < 0.17$. This method is called removal penalization as "the out of the bound" members are eliminated from the Pareto front.

In addition to that, another part of the code is responsible for ensuring that the aerodynamic results fall within the linear range of lift coefficient vs. angle of attack which is done before assessing and penalizing the aerodynamic data. The poor solutions are treated similarly to the ones in [81].

Second, a method for partial penalization is devised. Four different scenarios might happen.

- 1) The upper and lower limit of the c_l table are greater than the maximum and minimum c_l obtained from MSES,
- 2) The upper and lower limit of the c_l table are smaller than the maximum and minimum c_l obtained from MSES,
- 3) The upper limit of the c_l table is greater than the maximum c_l obtained from MSES and the lower limit of the c_l table is smaller than the maximum c_l obtained from MSES,
- 4) the upper and lower limits of the c_l table are not a part of the c_l range obtained from MSES.

In the first three cases, the weights, w_i, available in Table 6.1 will be assigned to zero for members that are out of the designated table. This will not remove the member from the Pareto front and keeps it close to that as it might be altered by crossover and mutation. This might be beneficial as the members close to the Pareto front will be preserved to pass the elite chromosomes to the next population. In the fourth case, the member will be treated similarly to the ones in the removal penalization method.

Unlike the removal method, this method ensures that good chromosomes will be passed to the next generation. However, in the first place, this might be misleading as it will overshadow the optimization process. This method is more customary in the optimization research area. For example, interested readers can refer to [82] and [83].

For the verification and validation of MSES, please refer to Section 3.4.

6.3 Results

Table 6.2 provides the NSGA-II parameters used in the box-wing optimization study. Appendix A presents the NSGA-II code verification. By adding a repository population, the convergence of such an optimization scheme can be tracked down. This repository population is the current population in the optimizer, which is displayed against the Pareto front. The repository members can be identified in Appendix A with black dots. The program will terminate when the rank of the repository is 1 for every member. One indication of this kind of convergence criterion is the rank that appears in the code's output.

Because of the high computing cost of the optimization, 50 generations are chosen. For the same reasons, the population is fixed at 50. Other settings in this framework remain unchanged from those in Chapter 4 as it is found reliable.

Table 6.2: NSGA-II setting parameters used in the present study.

Parameter	**Value**
Population size	50
Number of generations	50
Mutation probability	0.05
Crossover index	10
Distribution index	10

Figure 6.5 shows the Pareto optimal front obtained from the optimization framework. The abscissa and ordinate show $1000/f_P$ and $-f_T$ which are the aerodynamic and structural objective functions, respectively. As discussed previously, the structural objective function is the negative value of the configuration's total maximum thickness. The definitions of f_P and f_T are given in Section 6.2.2.

As seen, the population of the Pareto front is covering the range between $f_T = 0.32$ and 0.9. In some regions, such as close to $f_T = 0.72$, an accumulation of members is observed while there are also some regions with no solutions. It is expected that a more

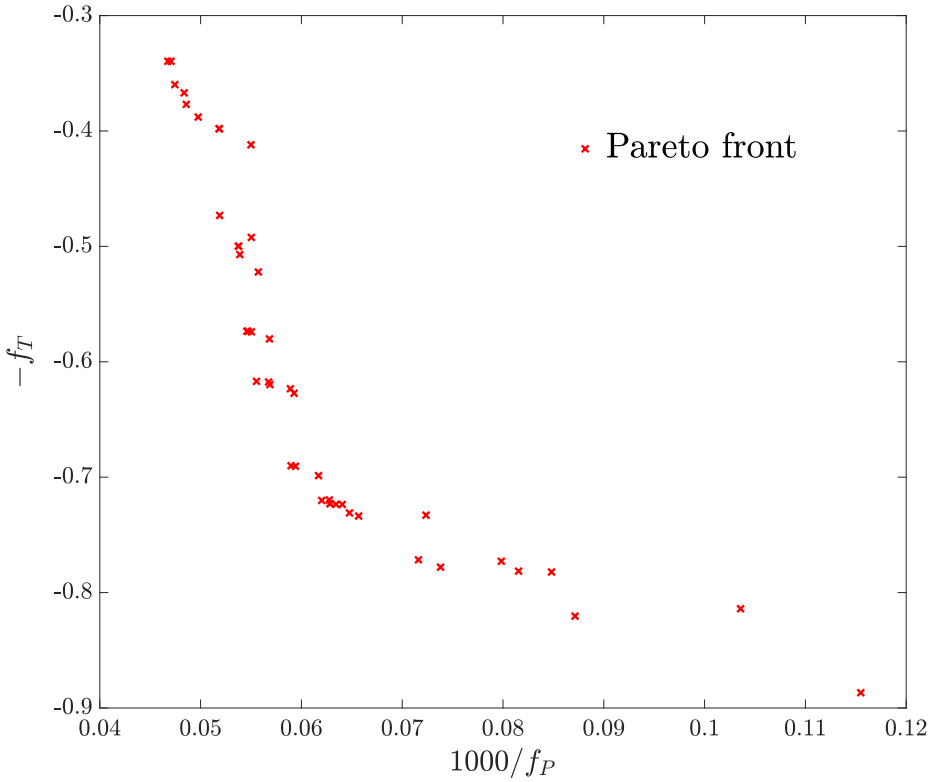

Figure 6.5: Pareto optimal front obtained from optimization framework with removal penalization technique.

uniformly distributed Pareto front will be obtained if a larger population size is employed. However, such trials are deferred to future works. As also observed from the Pareto front, over approximately $0.45 < f_T < 0.7$, $1000/f_P$ (or f_P) is weakly dependent on f_T.

The XFOIL code was utilized as the second solver to analyze the behavior of each airfoil. The reason for selecting XFOIL instead of MSES is that XFOIL can show the C_p plots for individual airfoils while MSES C_p plots are available only for an inverse design procedure where we edit the pressure contour and obtain the desired airfoil and cannot be written as an output as being one of the limitations.

Figure 6.6 shows the candidate airfoils with different total maximum thickness ratios.

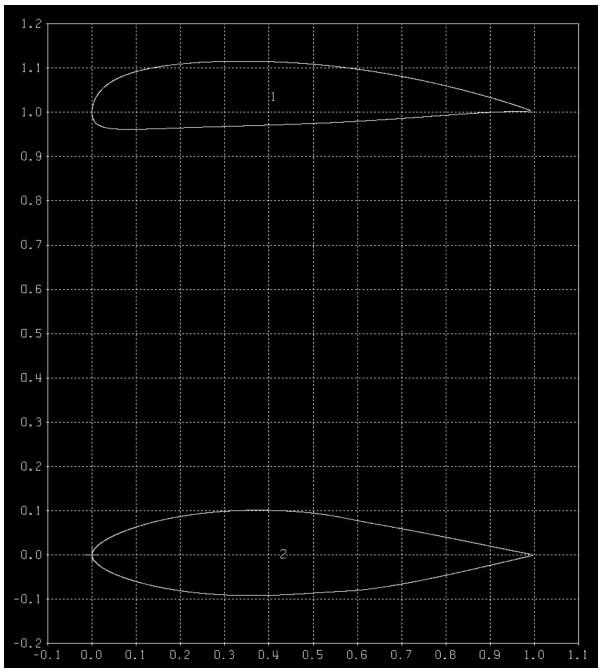
1.2
1.1
1.0
0.9
0.8
0.7
0.6
0.5
0.4
0.3
0.2
0.1
0.0
-0.1
-0.2
-0.1 0.0 0.1 0.2 0.3 0.4 0.5 0.6 0.7 0.8 0.9 1.0 1.1
1
2

(a)

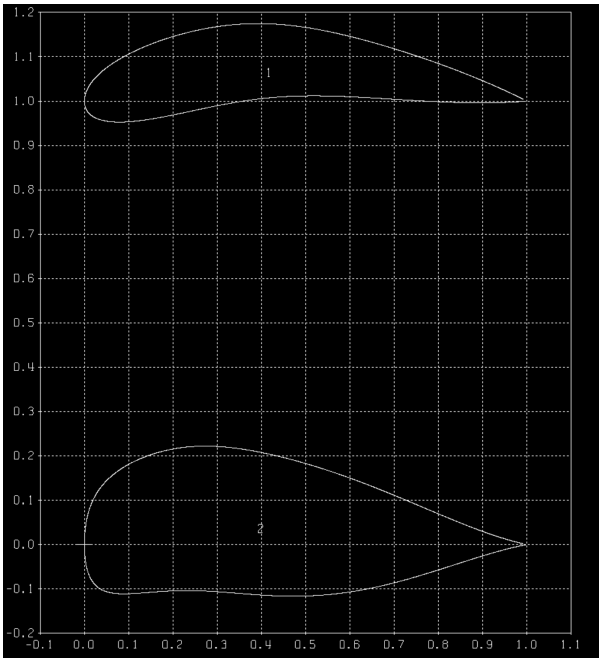
1.2
1.1
1.0
0.9
0.8
0.7
0.6
0.5
0.4
0.3
0.2
0.1
0.0
-0.1
-0.2
-0.1 0.0 0.1 0.2 0.3 0.4 0.5 0.6 0.7 0.8 0.9 1.0 1.1
1
2

(b)

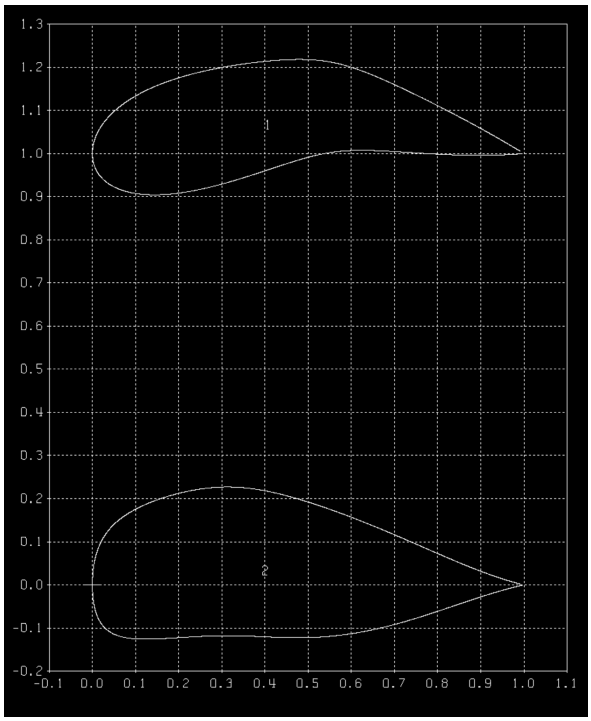

(c)

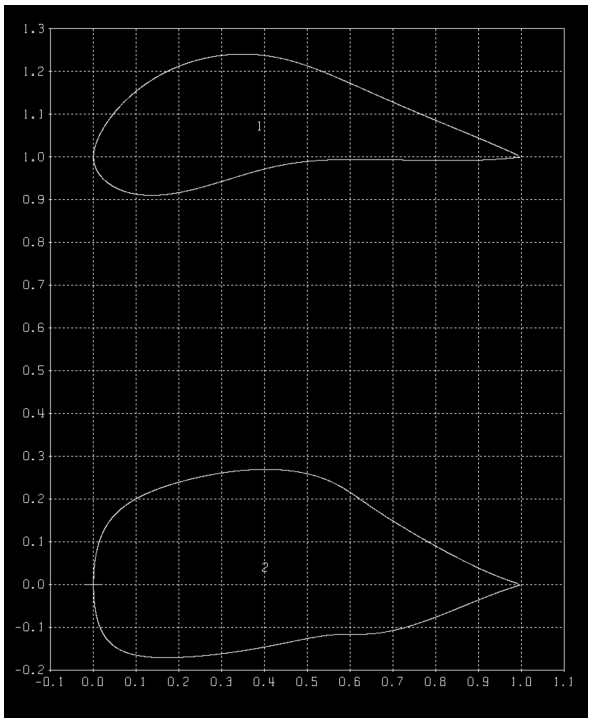

(d)

Figure 6.6: Candidate airfoils obtained from box-wing optimization framework with a total maximum thickness ratio of (a) 33.9%, (b) 50.7%, (c) 61.7%, and (d) 72.2%. The graphs are from *airset*.

The airfoil that is marked with 2 is the forward wing airfoil, acting as the main airfoil, and the airfoil marked with 1 is the aft wing airfoil, working as the supporting airfoil. For clarity, the main and auxiliary/supporting airfoils refer to airfoils 2 and 1, respectively.

Figure 6.6a shows the box-wing airfoils for $f_T = 33.9\%$. As seen, the main airfoil (the lower airfoil) is quite similar to symmetric airfoils while the auxiliary airfoil (the upper airfoil) is positively cambered and has a nearly flat lower side. The two airfoils feature a sharp trailing edge which aids in maintaining attached flow. Figure 6.6b shows the airfoils for $f_T = 50.7\%$, which are quite different from those observed earlier in Fig. 6.6a. Comparing the lower and upper airfoils, the lower airfoil is much thicker while the upper airfoil is more cambered. The lower airfoil has an unusually bluff nose and a nearly flat lower side. The upper airfoil, on the other hand, looks like a flapped airfoil. For larger thickness ratios, the optimal airfoils show similar but more pronounced features; for example, see Figs. 6.6c and 6.6d for $f_T = 61.7\%$ and 72.2%, respectively.

From the airfoil profiles shown above, a distinct role is observed between the two airfoils: the lower airfoil primarily maintains structural integrity while the upper airfoil predominantly ensures aerodynamic performance. This can be confirmed from the pressure coefficient (C_p) plots obtained via XFOIL for the lower and upper airfoils. It should be noted that these plots were obtained considering the lower and upper airfoils in isolation, which means possible aerodynamic interactions between the two airfoils were not included. This is because XFOIL can only perform aerodynamic analysis for single airfoils, and MSES is not equipped to provide C_p plots for multiple airfoils.

Figure 6.7 shows the C_p distribution over the lower airfoil in the box-wing configuration shown in Fig. 6.6a. The distributions are shown for three angles of attack $\alpha = 0$, 4 and 8 degrees. Figure 6.7a shows a negligibly small lift produced at $\alpha = 0$ over the lower airfoil, which is in agreement with an earlier observation regarding the symmetry of the airfoil profile. As the angle of attack is increased, a higher lift is generated although the contribution of the last 40% of the airfoil is negligible. Figure 6.8 shows the C_p plots for the upper airfoil in the configuration shown in Fig. 6.6a. In contrast to the lower airfoil, the upper airfoil generates a considerable amount of lift even at $\alpha = 0$. This is very much expected due to a positively cambered profile. As expected, lift increases by increasing α. Interestingly, an almost constant C_p is obtained over the lower side of the airfoil at $\alpha = 4$ and 8 degrees.

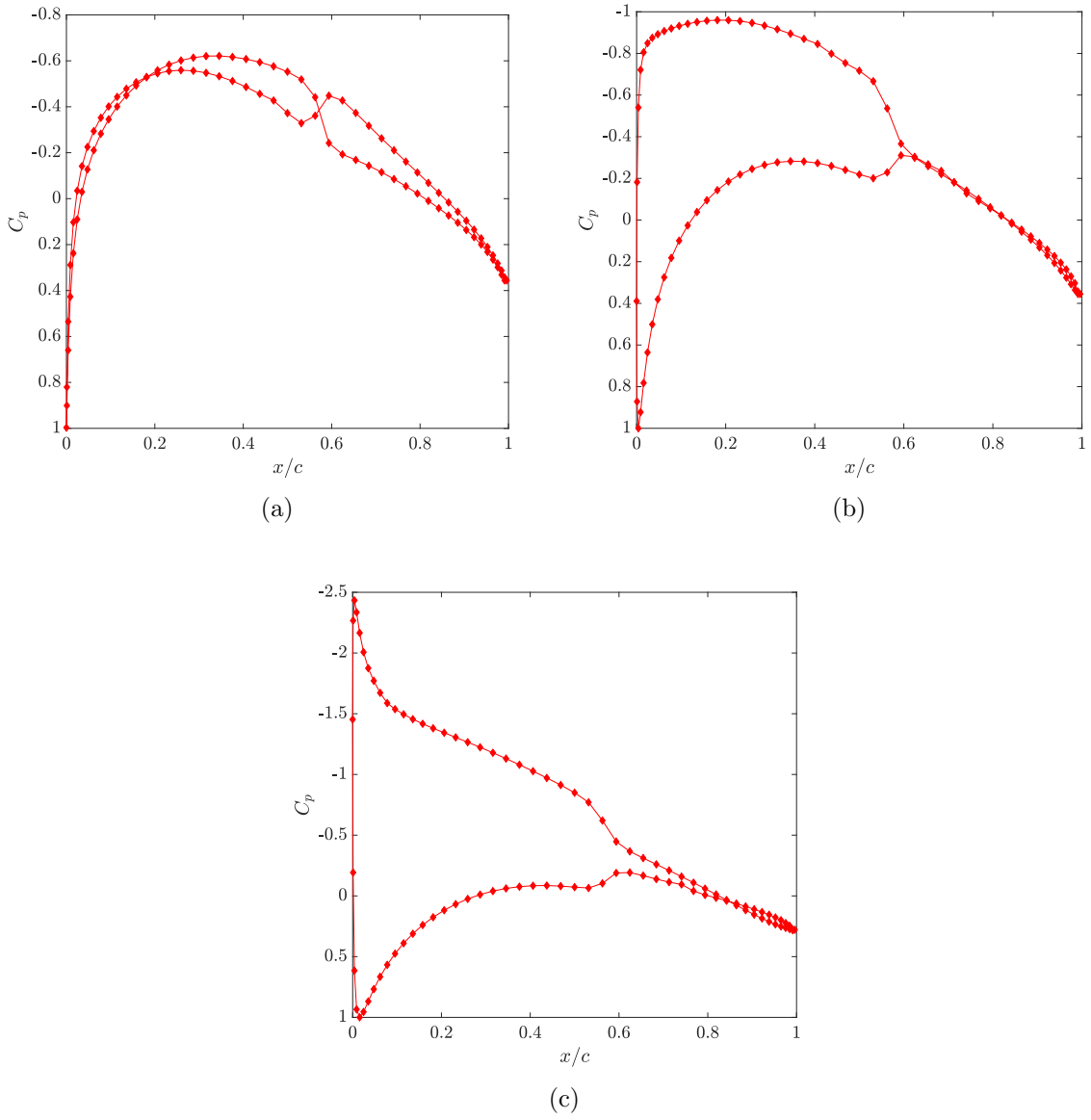

Figure 6.7: Pressure coefficient versus normalized chord length for the main airfoil obtained from XFOIL, airfoil marked with 2, shown in Fig.6.6a at angles of attack of (a) 0 deg, (b) 4 deg and (c) 8 deg.

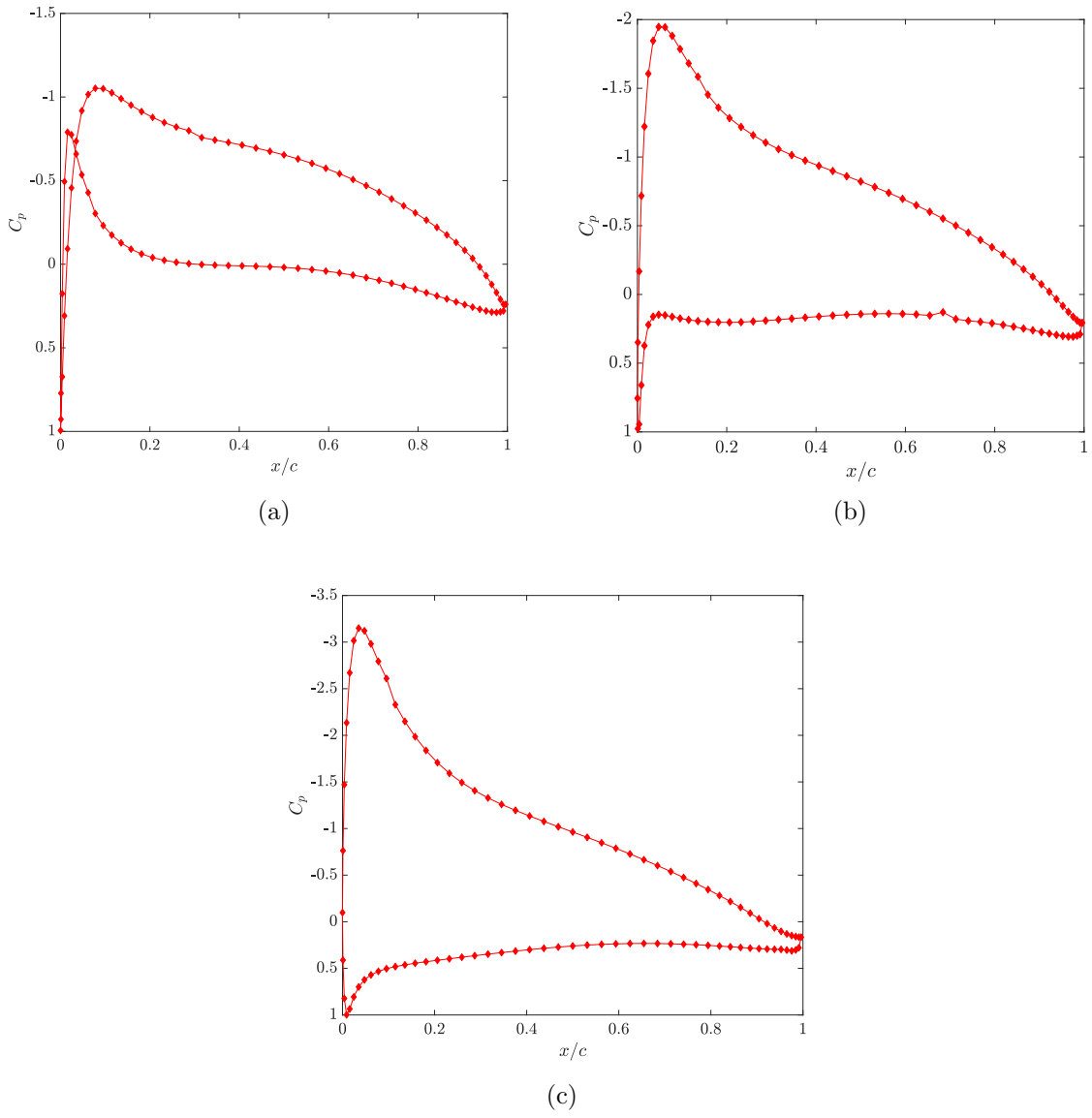

Figure 6.8: Pressure coefficient versus normalized chord length for the auxiliary airfoil obtained from XFOIL, airfoil marked with 1, shown in Fig.6.6a at angles of attack of (a) 0 deg, (b) 4 deg and (c) 8 deg.

Figures 6.9 and 6.10 show the C_p distributions over the lower and upper airfoils from the box-wing configuration with $f_T = 72.2\%$ (Fig. 6.6d). Comparing the C_p plots, it is also observed here that the upper airfoil is producing more lift than the lower airfoil – the aerodynamic role of the upper airfoil. Over the lower airfoil, similar to the observation made for $f_T = 33.9\%$, the last 40% of the chord length contributes only minimally to lift generation. The waviness of the pressure side (lower side) of the lower and upper airfoils is believed to be the source of fluctuating C_p over the pressure side.

A higher thickness ratio of the main airfoil has a structural significance in terms of 3-dimensional wing strength. Mock [84] considered the upper wing airfoil to have a higher lift which is proved by our optimization results. However, in biplane literature, the definition of the main and supporting wing is different where the upper wing is the main wing.

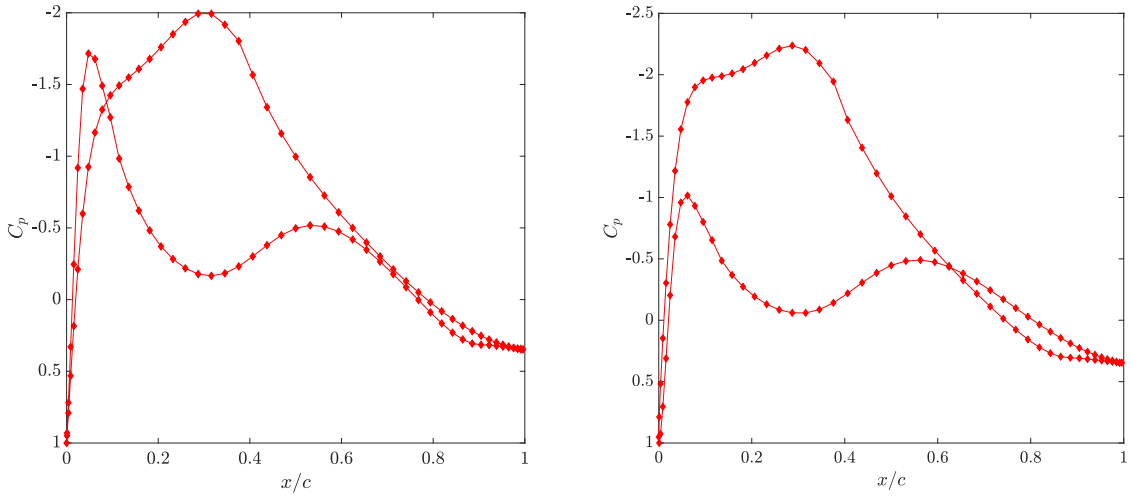

(a)

(b)

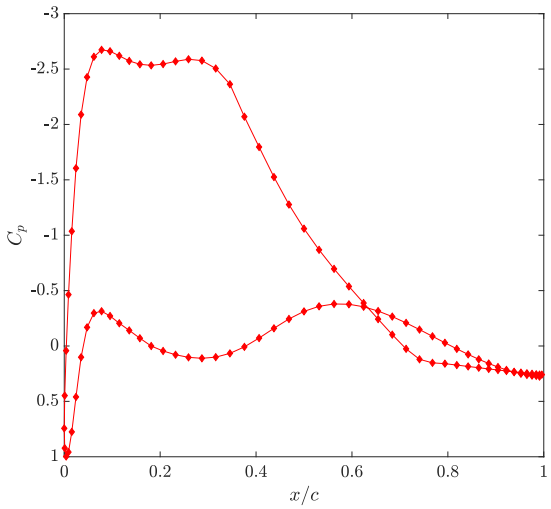

(c)

Figure 6.9: Pressure coefficient versus normalized chord length for the main airfoil obtained from XFOIL, airfoil marked with 2, shown in Fig.6.6d at angles of attack of (a) 0 deg, (b) 4 deg and (c) 8 deg.

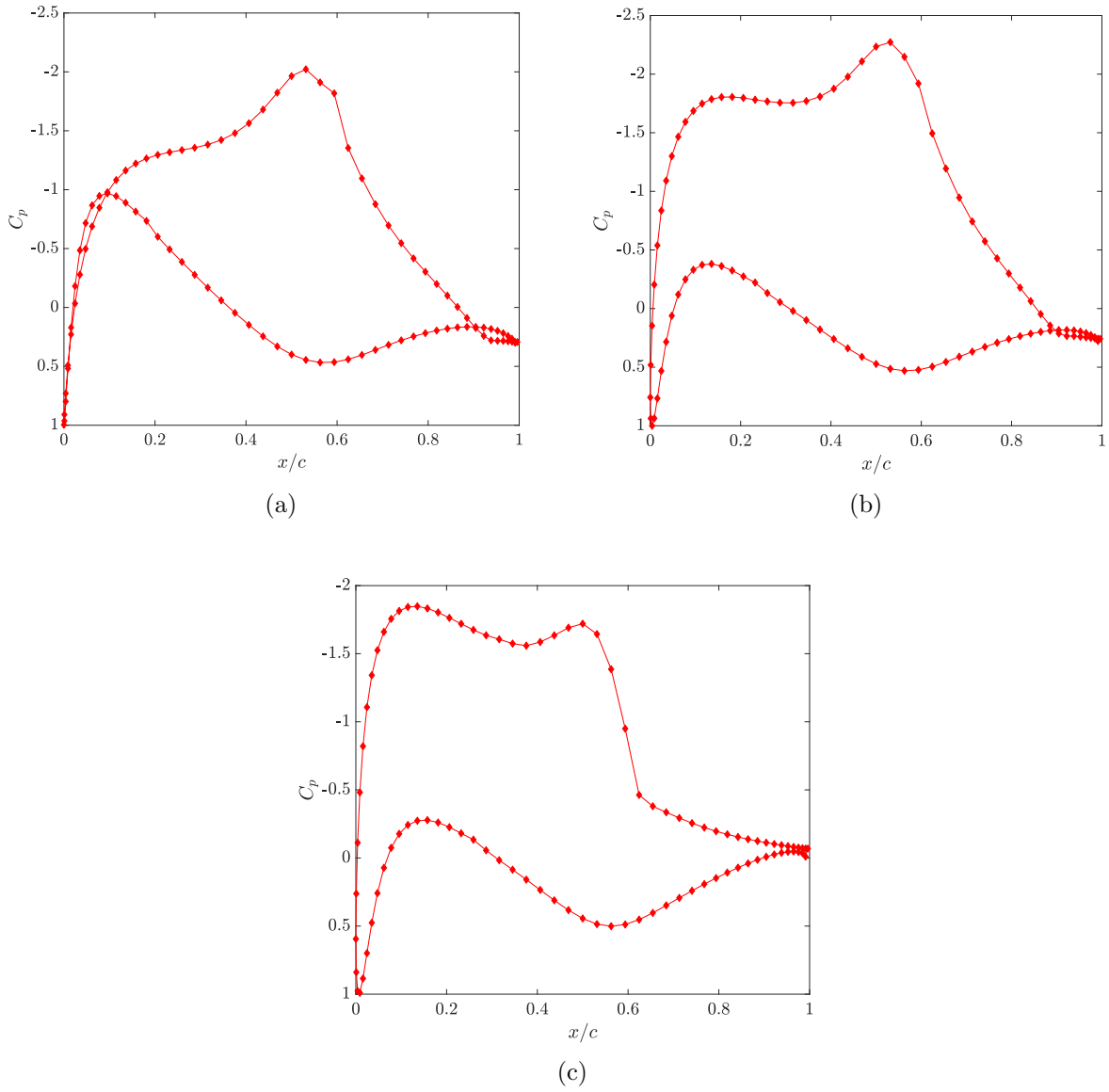

Figure 6.10: Pressure coefficient versus normalized chord length for the auxiliary airfoil obtained from XFOIL, airfoil marked with 1, as shown in Fig.6.6d at angles of attack of (a) 0 deg, (b) 4 deg and (c) 8 deg.

6.4 Conclusion

In this chapter, a framework for the optimization of box-wings was presented. The framework was kept limited to airfoils. The verification and validation of the aerodynamic solver, MSES, was presented in Chapter 3. Some numerical results were obtained for a box-wing configuration with zero stagger, zero decalage, a fixed gap, and fixed chord lengths. The results indicated that the lower airfoil's role is primarily structural while the upper airfoil is predominantly responsible to generate lift. This was more evident for lower thickness ratios. As the thickness ratio was increased, the lower airfoil's nose became more bluff and its lower side became wavier. The upper airfoil, on the other hand, looked like a flapped airfoil. More detailed studies including the use of CFD for aerodynamic solutions should be performed, which are deferred to future.

Chapter 7

Conclusion and future works

This research has focused on optimizing airfoils and wings for AWE systems. By improving the aerodynamic efficiency, the optimization leads to better power output, thereby reducing the levelized cost of energy (LCOE). This reduction in LCOE enhances the competitiveness of AWE systems compared to traditional wind turbines and other renewable energy sources. In Chapter 1, the theory concerning the performance, operation, and design of AWE systems is reviewed. This includes enhancing power output, refining control strategies, and improving the structural aspects of CKPSs. It also emphasizes the benefits of higher-altitude wind and lightweight designs. Chapters 2 and 3 discuss the building blocks of an aerodynamic optimization framework, detailing the background, parameters influencing the optimization process, and the specifics of each aerodynamic solver. Three low-fidelity codes—XFOIL, OpenVSP, and MSES—are briefly introduced, highlighting the strengths of each package.

Optimal airfoils for the rigid crosswind kite are designed using NSGA-II. Implementing a parameterization method alongside physical design parameters significantly reduces the decision-making time for selecting the optimal airfoil. Additionally, minimizing the number of design variables decreases the computational time required for the optimization framework.

The parametric study in Chapter 4 examines the effects of tether drag and induced drag on the kite. Tether drag is identified as the primary contributor to the total drag of the system. Airfoils designed with consideration of tether drag feature a flap-like trailing edge, which enhances lift to offset the additional drag introduced by the tether. Airfoils with sharp trailing edges are observed to reduce induced drag. The sharp trailing edge promotes flow attachment, thereby decreasing viscous drag. This also helps in mitigating turbulent wake effects during the operation of the kite. According to CFD analysis, the separation region over the airfoil alters the effective body shape, increasing the area under the C_p curve and resulting in a higher lift coefficient. Despite the lift coefficient table remaining constant, the optimizer seeks to achieve high lift coefficients for the airfoils, as illustrated in Table 4.3.

The wing planform optimization is detailed in Chapter 5. Verification of the optimization framework is demonstrated by showing that maximizing the lift-to-drag ratio results in a wing planform approaching an elliptical shape. Similarly, the wing platform optimized for AWE systems closely approximates an elliptical shape, with minor differences in chord placements and span lengths.

Chapter 6 discusses the airfoil optimization for the box-wing configuration. This configuration is approximated using two airfoils positioned vertically with a fixed gap-to-chord ratio. The results indicate that the airfoil of the main wing (forward wing) requires a thicker airfoil, while the auxiliary wing needs a more curved airfoil. The main wing provides both structural support and generates aerodynamic lift. The auxiliary wing generates the additional lift required to meet the aerodynamic performance criteria.

The optimization frameworks developed in this thesis can be further improved. Enhancements can also be made to the accuracy and feature space of the utilized packages. The list of prospective works is presented below:

- Adding a more comprehensive structural objective function to all three frameworks,

- Obtaining the partial penalization results presented in Chapter 6 for the airfoils in box-wing applicable to AWE,
- Performing Computational Fluid Dynamics (CFD) studies on the airfoils obtained in Chapter 6 to analyze the effect of airfoils on each other.
- Modifying the XFOIL code to incorporate wake interaction and thus the effect of rotation.
- Considering the consumption phase of the crosswind kites in the objective functions

References

[1] M. Kheiri, V. S. Nasrabad, and F. Bourgault, "A new perspective on the aerodynamic performance and power limit of crosswind kite systems," *Journal of Wind Engineering and Industrial Aerodynamics*, vol. 190, pp. 190–199, 2019.

[2] "Makani - x, the moonshot factory," https://x.company/projects/makani, accessed: 2022-10-30.

[3] S. Rao, *Engineering Optimization: Theory and Practice*. Wiley, 2019. [Online]. Available: https://books.google.ca/books?id=Xiq7DwAAQBAJ

[4] K. Deb, A. Pratap, S. Agarwal, and T. Meyarivan, "A fast and elitist multiobjective genetic algorithm: Nsga-ii," *IEEE Transactions on Evolutionary Computation*, vol. 6, no. 2, pp. 182–197, 2002.

[5] J. Stack, *Tests in the variable density wind tunnel to investigate the effects of scale and turbulence on airfoil characteristics*. National Advisory Committee for Aeronautics, 1931, vol. 364.

[6] M. Drela, "A user's guide to mses 3.05," *Massachusetts Institute of Technology (MIT), Cambridge*, 2007.

[7] L. Luo, C. Jiang, Z. Gao, and C. Lee, "Aerodynamic interference and reynolds number

effects of low-speed close-coupled biplanes," *Journal of Aerospace Engineering*, vol. 33, no. 4, p. 04020026, 2020.

[8] L. OLSON, W. JAMES, and P. MCGOWAN, "Theoretical and experimental study of the drag of multielement airfoils." [Online]. Available: https://arc.aiaa.org/doi/abs/10.2514/6.1978-1223

[9] E. Omar, T. Zierten, M. Hahn, E. Szpiro, and A. Mahal, "Two-dimensional wind-tunnel tests of a nasa supercritical airfoil with various high-lift systems. volume 2: Test data," NASA, Tech. Rep., 1977, available:https://ntrs.nasa.gov/api/citations/19800003805/downloads/19800003805.pdf.

[10] B. Kulfan and J. Bussoletti, *"Fundamental" Parameteric Geometry Representations for Aircraft Component Shapes.* [Online]. Available: https://arc.aiaa.org/doi/abs/10.2514/6.2006-6948

[11] D. A. Masters, N. J. Taylor, T. Rendall, C. B. Allen, and D. J. Poole, *Review of Aerofoil Parameterisation Methods for Aerodynamic Shape Optimisation.* [Online]. Available: https://arc.aiaa.org/doi/abs/10.2514/6.2015-0761

[12] X. Lu, J. Huang, L. Song, and J. Li, "An improved geometric parameter airfoil parameterization method," *Aerospace Science and Technology*, vol. 78, pp. 241–247, 2018.

[13] E. Kroon, "Airborne wind energy airfoils: Design of pareto-optimal airfoils for rigid wing systems in the field of airborne wind energy," 2018, available:http://resolver.tudelft.nl/uuid:dd976c1b-edda-4941-8b28-c28f87284a77.

[14] F. C. Ribeiro, A. A. de Paula, D. Scholz, and R. G. A. da Silva, "Wing geometric parameter studies of a box wing aircraft configuration for subsonic flight," 2017. [Online]. Available: https://api.semanticscholar.org/CorpusID:201706981

[15] L. Prandtl, "Induced drag of multiplanes," Tech. Rep., 1924.

[16] M. Diehl, "Airborne wind energy: Basic concepts and physical foundations," in *Airborne wind energy*, 2013, pp. 3–22.

[17] P. Warnke, K. Cuhls, U. Schmoch, L. Daniel, L. Andreescu, B. Dragomir, R. Gheorghiu, C. Baboschi, A. Curaj, M. Parkkinen, and O. Kuusi, "100 Radical Innovation Breakthroughs for the Future, Directorate-General for Research and Innovation, Luxembourg: Publications Office of the European Union," Tech. Rep., 2019.

[18] U. Ahrens, M. Diehl, and R. Schmehl, Eds., *Airborne Wind Energy*. Berlin: Springer, 2013.

[19] A. Cherubini, A. Papini, R. Vertechy, and M. Fontana, "Airborne wind energy systems: A review of the technologies," *Renewable and Sustainable Energy Reviews*, vol. 51, pp. 1461–1476, 2015.

[20] R. Schmehl, Ed., *Airborne Wind Energy*. Singapore: Springer, 2018.

[21] M. L. Loyd, "Crosswind kite power," *Journal of Energy (AIAA)*, vol. 4, no. 3, pp. 106–111, 1980, article No. 80-4075.

[22] A. Akberali, M. Kheiri, and F. Bourgault, "Generalized aerodynamic models for crosswind kite power systems," *Journal of Wind Engineering and Industrial Aerodynamics*, vol. 215, 2021.

[23] S. Hirshorn and S. Jefferies, "Final report of the nasa technology readiness assessment (tra) study team," Tech. Rep., 2016.

[24] European Commission, "Study on challenges in the commercialisation of airborne wind

energy systems, Directorate-General for Research and Innovation, Luxembourg: Publications Office of the European Union," Tech. Rep., 2018.

[25] M. De Lellis, R. Reginatto, R. Saraiva, and A. Trofino, "The Betz limit applied to airborne wind energy," *Renewable Energy*, vol. 127, pp. 32–40, 2018.

[26] I. Argatov, P. Rautakorpi, and R. Silvennoinen, "Estimation of the mechanical energy output of the kite wind generator," *Renewable Energy*, vol. 34, no. 6, pp. 1525–1532, 2009.

[27] M. Kheiri, F. Bourgault, V. S. Nasrabad, and S. Victor, "On the aerodynamic performance of crosswind kite power systems," *Journal of Wind Engineering and Industrial Aerodynamics*, vol. 181, pp. 1–13, 2018.

[28] M. Kheiri, S. Victor, S. Rangriz, M. M. Karakouzian, and F. Bourgault, "Aerodynamic performance and wake flow of crosswind kite power systems," *Energies*, vol. 15, no. 7, p. 2449, 2022.

[29] U. Fasel, D. Keidel, G. Molinari, and P. Ermanni, "Aerostructural optimization of a morphing wing for airborne wind energy applications," *Smart Materials and Structures*, vol. 26, no. 9, p. 095043, aug 2017. [Online]. Available: https://dx.doi.org/10.1088/1361-665X/aa7c87

[30] F. Bauer, R. M. Kennel, C. M. Hackl, F. Campagnolo, M. Patt, and R. Schmehl, "Drag power kite with very high lift coefficient," *Renewable Energy*, vol. 118, pp. 290–305, 2018.

[31] I. Castro-Fernández, R. Borobia-Moreno, R. Cavallaro, and G. Sánchez-Arriaga, "Three-dimensional unsteady aerodynamic analysis of a rigid-framed delta kite applied to airborne wind energy," *Energies*, vol. 14, p. 8080, 2021.

[32] J. Oehler and R. Schmehl, "Aerodynamic characterization of a soft kite by in situ flow measurement," *Wind Energy Science*, vol. 4, pp. 1–21, 2019.

[33] R. v. d. Vlugt, A. Bley, M. Noom, and R. Schmehl, "Quasi-steady model of a pumping kite power system," *Renewable Energy*, vol. 131, pp. 83–99, 2019.

[34] U. Fechner, R. van der Vlugt, E. Schreuder, and R. Schmehl, "Dynamic model of a pumping kite power system," *Renewable Energy*, vol. 83, pp. 705–716, 2015.

[35] H. Li, "Power limit of crosswind kites," 2019.

[36] Q. Zhang, W. Miao, Q. Liu, Z. Xu, C. Li, L. Chang, and M. Yue, "Optimized design of wind turbine airfoil aerodynamic performance and structural strength based on surrogate model," *Ocean Engineering*, vol. 289, p. 116279, 2023.

[37] T. Hansen, "Airfoil optimization for wind turbine application," *Wind Energy*, vol. 21, no. 7, pp. 502–514, 2018.

[38] A. C. Benim, M. Diederich, and B. Pfeiffelmann, "Aerodynamic optimization of airfoil profiles for small horizontal axis wind turbines," *Computation*, vol. 6, no. 2, p. 34, 2018.

[39] X. Li, L. Zhang, J. Song, F. Bian, and K. Yang, "Airfoil design for large horizontal axis wind turbines in low wind speed regions," *Renewable Energy*, vol. 145, pp. 2345–2357, 2020. [Online]. Available: https://www.sciencedirect.com/science/article/pii/S0960148119311838

[40] "Aerodynamic shape optimization of wind turbine blades for minimizing power production losses due to icing," *Cold Regions Science and Technology*, vol. 185, p. 103250, 2021. [Online]. Available: https://www.sciencedirect.com/science/article/pii/S0165232X21000318

[41] D. Eijkelhof, G. Buendía, and R. Schmehl, "Low- and high-fidelity aerodynamic simulations of box wing kites for airborne wind energy applications," *Energies*, vol. 16, no. 7, 2023. [Online]. Available: https://www.mdpi.com/1996-1073/16/7/3008

[42] A. Porta Ko, S. Smidt, R. Schmehl, and M. Mandru, "Optimisation of a multi-element airfoil for a fixed-wing airborne wind energy system," *Energies*, vol. 16, no. 8, 2023. [Online]. Available: https://www.mdpi.com/1996-1073/16/8/3521

[43] A. Saleem and M.-H. Kim, "Aerodynamic performance optimization of an airfoil-based airborne wind turbine using genetic algorithm," *Energy*, vol. 203, p. 117841, 2020. [Online]. Available: https://www.sciencedirect.com/science/article/pii/S0360544220309488

[44] "Configuration optimization and global sensitivity analysis of ground-gen and fly-gen airborne wind energy systems," *Renewable Energy*, vol. 178, pp. 385–402, 2021. [Online]. Available: https://www.sciencedirect.com/science/article/pii/S0960148121008752

[45] A. U. Zgraggen, L. Fagiano, and M. Morari, "Real-time optimization and adaptation of the crosswind flight of tethered wings for airborne wind energy," *IEEE Transactions on Control Systems Technology*, vol. 23, no. 2, pp. 434–448, 2014.

[46] F. Trevisi, I. Castro-Fernández, G. Pasquinelli, C. E. D. Riboldi, and A. Croce, "Flight trajectory optimization of fly-gen awe systems through a harmonic balance method," *Wind Energy Science Discussions*, vol. 2022, pp. 1–29, 2022.

[47] S. Costello, G. François, and D. Bonvin, "Real-time optimizing control of an experimental crosswind power kite," *IEEE Transactions on Control Systems Technology*, vol. 26, pp. 507–522, 2018.

[48] C. Jehle and R. Schmehl, "Applied tracking control for kite power systems," *Journal of Guidance, Control, and Dynamics*, vol. 37, pp. 1211–1222, 2014.

[49] D. Todeschini, L. Fagiano, C. Micheli, and A. Cattano, "Control of a rigid wing pumping airborne wind energy system in all operational phases," *Control Engineering Practice*, vol. 111, p. 104794, 2021. [Online]. Available: https://www.sciencedirect.com/science/article/pii/S096706612100071X

[50] G. Venter, *Review of Optimization Techniques*. John Wiley Sons, Ltd, 2010. [Online]. Available: https://onlinelibrary.wiley.com/doi/abs/10.1002/9780470686652.eae495

[51] Y. Ma, A. Zhang, L. Yang, C. Hu, and Y. Bai, "Investigation on optimization design of offshore wind turbine blades based on particle swarm optimization," *Energies*, vol. 12, no. 10, 2019. [Online]. Available: https://www.mdpi.com/1996-1073/12/10/1972

[52] R. Özkan and M. S. Genç, "Multi-objective structural optimization of a wind turbine blade using nsga-ii algorithm and fsi," *Aircraft Engineering and Aerospace Technology*, vol. 93, no. 6, pp. 1029–1042, 2021.

[53] K. Yang and K. Cho, "Simulated annealing algorithm for wind farm layout optimization: A benchmark study," *Energies*, vol. 12, no. 23, 2019. [Online]. Available: https://www.mdpi.com/1996-1073/12/23/4403

[54] K. Deb and R. B. Agrawal, "Simulated binary crossover for continuous search space," *Complex Syst.*, vol. 9, 1995. [Online]. Available: https://api.semanticscholar.org/CorpusID:18860538

[55] M. Drela, "Xfoil: An analysis and design system for low reynolds number airfoils. in: Mueller, t.j. (eds) low reynolds number aerodynamics," *Lecture Notes in Engineering*, vol. 54, pp. 1–12, 1989.

[56] M. Drela, "Xfoil 6.9 user primer," *Massachusetts Institute of Technology (MIT), Cambridge*, 2001.

[57] M. D. Maughmer and J. G. Coder, "Comparisons of theoretical methods for predicting airfoil aerodynamic characteristics," *US Army Aviation Research, Development and Engineering Command RDECOM TR*, 2010.

[58] D. C. Wilcox, *Turbulence Modeling for CFD*, ser. Turbulence Modeling for CFD. DCW Industries, 2006, no. v. 1. [Online]. Available: https://books.google.ca/books?id=tFNNPgAACAAJ

[59] F. R. Menter, "Two-equation eddy-viscosity turbulence models for engineering applications," *AIAA journal*, vol. 32, no. 8, pp. 1598–1605, 1994.

[60] D. C. Wilcox, "Reassessment of the scale-determining equation for advanced turbulence models," *AIAA Journal*, vol. 26, no. 11, pp. 1299–1310, 1988.

[61] N. N. Sørensen, J. Michelsen, and S. Schreck, "Navier–stokes predictions of the nrel phase vi rotor in the nasa ames 80 ft× 120 ft wind tunnel," *Wind Energy: An International Journal for Progress and Applications in Wind Power Conversion Technology*, vol. 5, no. 2-3, pp. 151–169, 2002.

[62] K. McLaren, S. Tullis, and S. Ziada, "Computational fluid dynamics simulation of the aerodynamics of a high solidity, small-scale vertical axis wind turbine," *Wind Energy*, vol. 15, no. 3, pp. 349–361, 2012.

[63] L. Wang, R. Quant, and A. Kolios, "Fluid structure interaction modeling of horizontal-axis wind turbine blades based on cfd and fea," *Journal of Wind Engineering and Industrial Aerodynamics*, vol. 158, pp. 11–25, 2016.

[64] L. Menegozzo, A. Dal Monte, E. Benini, and A. Benato, "Small wind turbines: A numerical study for aerodynamic performance assessment under gust conditions," *Renewable energy*, vol. 121, pp. 123–132, 2018.

[65] H. Sobieczky, "Parametric airfoils and wings," pp. 71–87, 1999. [Online]. Available: https://doi.org/10.1007/978-3-322-89952-1

[66] T. W. Sederberg and S. R. Parry, "Free-form deformation of solid geometric models," p. 151–160, 1986. [Online]. Available: https://doi.org/10.1145/15922.15903

[67] A. F. Abril, "Real coded (integer handling) nsga ii," *MATLAB Central File Exchange*, 2019.

[68] K. Kallstrom, "Exploring airfoil table generation using xfoil and overflow," *NASA Technical Report*, 2022.

[69] P. Echeverri, T. Fricke, G. Homsy, and N. Tucker, *The Energy Kite: Selected Results from the Design, Development, and Testing of Makani's Airborne Wind Turbines, Part I of III*. Makani Technologies LLC, 2020.

[70] P. Williams and E. Pechenik, "Kites for wind energy," in *Handbook of Wind Energy Aerodynamics*. Springer, 2022, pp. 1253–1316.

[71] L. v. Hagen, K. Petrick, S. Wilhelm, and R. Schmehl, "Life-cycle assessment of a multi-megawatt airborne wind energy system," *Energies*, vol. 16, no. 4, p. 1750, 2023.

[72] Skysails, "Onshore Unit SKS PN-14: A Revolution for Onshore Wind Power," 2024, [Accessed on June-06-2024] https://www.skysails-power.com/onshore-unit-pn-14/.

[73] G. De Fezza and S. Barber, "Parameter analysis of a multi-element airfoil for application to airborne wind energy," *Wind Energy Science*, vol. 7, no. 4, pp. 1627–1640, 2022.

[74] S. Gai and R. Palfrey, "Influence of trailing-edge flow control on airfoil performance," *Journal of Aircraft*, vol. 40, no. 2, pp. 332–337, 2003.

[75] A. A. Candade, M. Ranneberg, and R. Schmehl, "Structural analysis and optimization of a tethered swept wing for airborne wind energy generation," *Wind Energy*, vol. 23, no. 4, pp. 1006–1025, 2020. [Online]. Available: https://onlinelibrary.wiley.com/doi/abs/10.1002/we.2469

[76] N. Pynaert, T. Haas, J. Wauters, G. Crevecoeur, and J. Degroote, "Wing deformation of an airborne wind energy system in crosswind flight using high-fidelity fluid–structure interaction," *Energies*, vol. 16, no. 2, 2023. [Online]. Available: https://www.mdpi.com/1996-1073/16/2/602

[77] J. D. Anderson, *Fundamentals of Aerodynamics*, 6th ed. McGraw-Hill Education, 2017.

[78] M. M. Munk, "General biplane theory," Tech. Rep., 1923.

[79] P. D. Gall and H. C. Smith, "Aerodynamic characteristics of biplanes with winglets," *Journal of Aircraft*, vol. 24, no. 8, pp. 518–522, 1987.

[80] F. H. Norton, "The effect of staggering a biplane," Tech. Rep., 1921.

[81] Z. Cui, Y. Chang, J. Zhang, X. Cai, and W. Zhang, "Improved nsga-iii with selection-and-elimination operator," *Swarm and Evolutionary Computation*, vol. 49, pp. 23–33, 2019. [Online]. Available: https://www.sciencedirect.com/science/article/pii/S2210650218309787

[82] R. Azzouz, S. Bechikh, L. B. Said, and W. Trabelsi, "Handling time-varying constraints and objectives in dynamic evolutionary multi-objective optimization,"

Swarm and Evolutionary Computation, vol. 39, pp. 222–248, 2018. [Online]. Available: https://www.sciencedirect.com/science/article/pii/S2210650217302717

[83] J. G. Hobbie, A. H. Gandomi, and I. Rahimi, "A comparison of constraint handling techniques on nsga-ii," *Archives of Computational Methods in Engineering*, vol. 28, no. 5, pp. 3475–3490, 2021.

[84] R. M. Mock, "The distribution of loads between the wings of a biplane having decalage," Tech. Rep., 1927.

[85] F. Kursawe, "A variant of evolution strategies for vector optimization," pp. 193–197, 1991.

[86] J. D. Schaffer, "Multiple objective optimization with vector evaluated genetic algorithms," 1985. [Online]. Available: https://api.semanticscholar.org/CorpusID:262338711

[87] P. T. Binh, "Mobes : A multiobjective evolution strategy for constrained optimization problems," 1997. [Online]. Available: https://api.semanticscholar.org/CorpusID:14315597

Appendix A

NSGA-II code verification

This section is serving as the verification step for the code used in the airfoil optimization. The code implemented in the airfoil optimization is from MATLAB application center, where third party developers can publish their codes. The problems to test as a benchmark was available and compared against the optimization framework results. However, the benchmark problems have been tested in the local computer, where the airfoil optimization and wing optimization have been performed. The description of the problems have been included below:

- Kursawe function [85]

$$\begin{cases} f_1(x) = \sum_{i=1}^{2}[-10exp(0.2\sqrt{x_i^2 + x_{i+1}^2})] \\ f_2(x) = \sum_{i=1}^{3}[|x_i|^{0.8} + 5sin(x_i^3)] \\ -5 \leq x_i \leq 5 \\ 1 \leq i \leq 3 \end{cases}$$

- Schaffer function [86]

$$\begin{cases} f_1(x) = x^2 \\ f_2(x) = (x-2)^2 \\ -A \leq x \leq A \\ A \in [10, 10^5] \end{cases}$$

- Zitzler-Deb-Thiele's function 2 (ZDT2) [4]

$$\begin{cases} f_1(x) = x_1 \\ f_2(x) = g(x)h(f_1(x), g(x)) \\ g(x) = 1 + \frac{9}{29}\sum_{i=2}^{30} x_i \\ h(f_1(x), g(x)) = 1 - (\frac{f_1(x)}{g(x)})^2 \\ 0 \leq x_i \leq 1 \\ 1 \leq i \leq 30 \end{cases}$$

- Zitzler-Deb-Thiele's function 6 (ZDT6) [4]

$$\begin{cases} f_1(x) = 1 - exp(-4x_1)sin(6\pi x_1)^6 \\ f_2(x) = g(x)h(f_1(x), g(x)) \\ g(x) = 1 + 9\left[\frac{\sum_{i=2}^{10} x_i}{9}\right]^{0.25} \\ h(f_1(x), g(x)) = 1 - (\frac{f_1(x)}{g(x)})^2 \\ 0 \leq x_i \leq 1 \\ 1 \leq i \leq 10 \end{cases}$$

Although these are some examples of unconstrained problems, the code could successfully verify the constrained problems as well. The constrained problems tried to verify the code is as follows:

- Binh and Korn function [87]

$$\begin{cases} f_1(x) = 4x^2 + 4y^2 \\ f_2(x) = (x-5)^2 + (y-5)^2 \\ 0 \leq x \leq 5 \\ 0 \leq y \leq 3 \end{cases}$$

subject to:

$$\begin{cases} g_1(x,y) = (x-5)^2 + y^2 \leq 25 \\ g_2(x,y) = (x-8)^2 + (y+3)^2 \geq 7.7 \end{cases}$$

The results of the optimization problems are compared against the numerical results presented in the original NSGA-II study [4]. The same settings suggested in this publication has been implemented in the code and also 250 Generations and 100 population were implemented to verify each problem set.

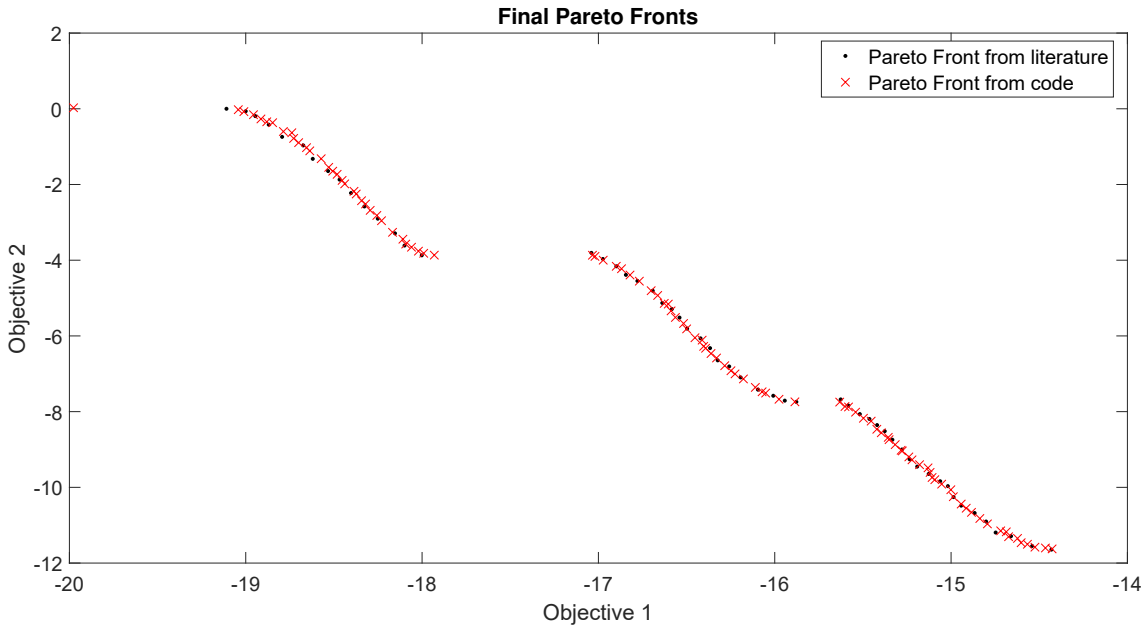

Figure A.1: Comparison of two Pareto fronts obtained from the literature [4] and the code used in the airfoil optimization for the Kursawe function

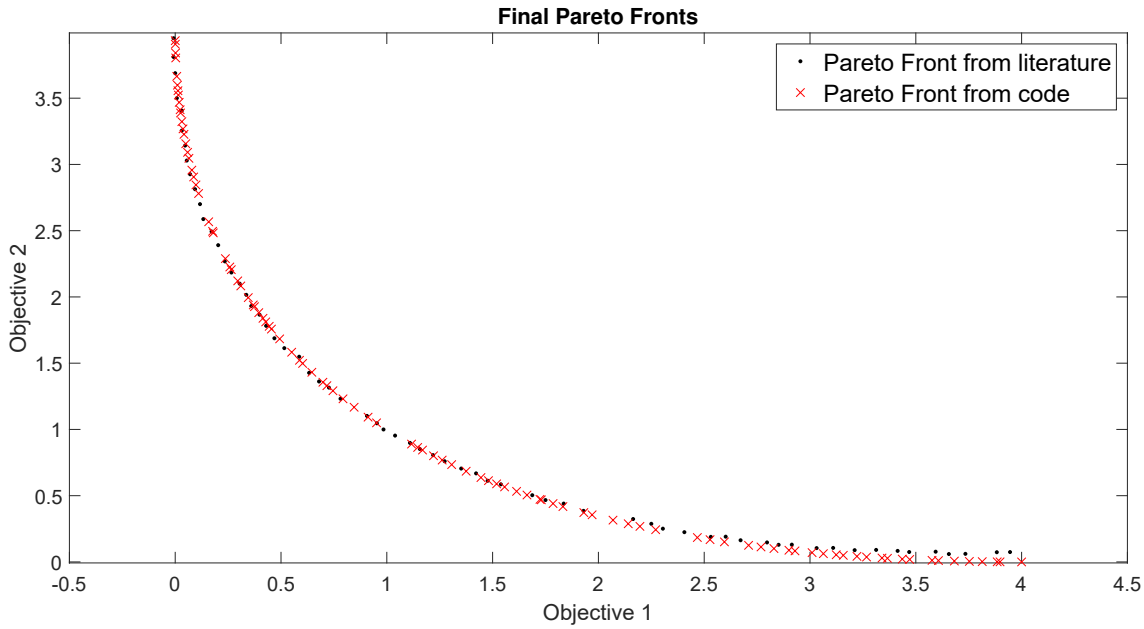

Figure A.2: Comparison of two Pareto fronts obtained from the literature [4] and the code used in the airfoil optimization for the Schaffer function

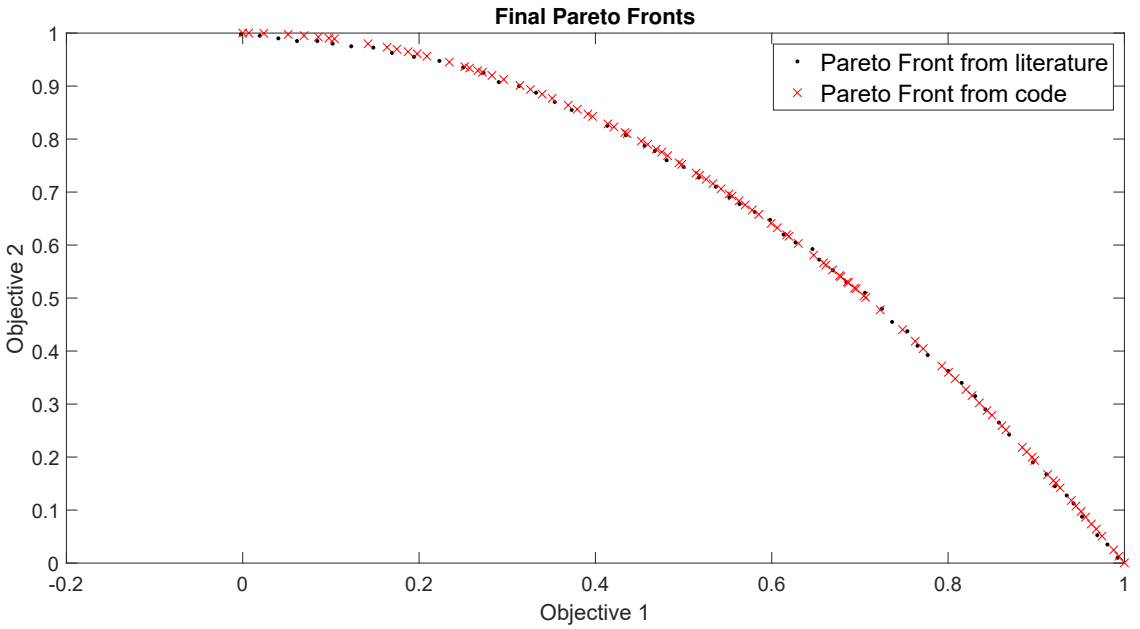

Figure A.3: Comparison of two Pareto fronts obtained from the literature [4] and the code used in the airfoil optimization for the ZDT2 function

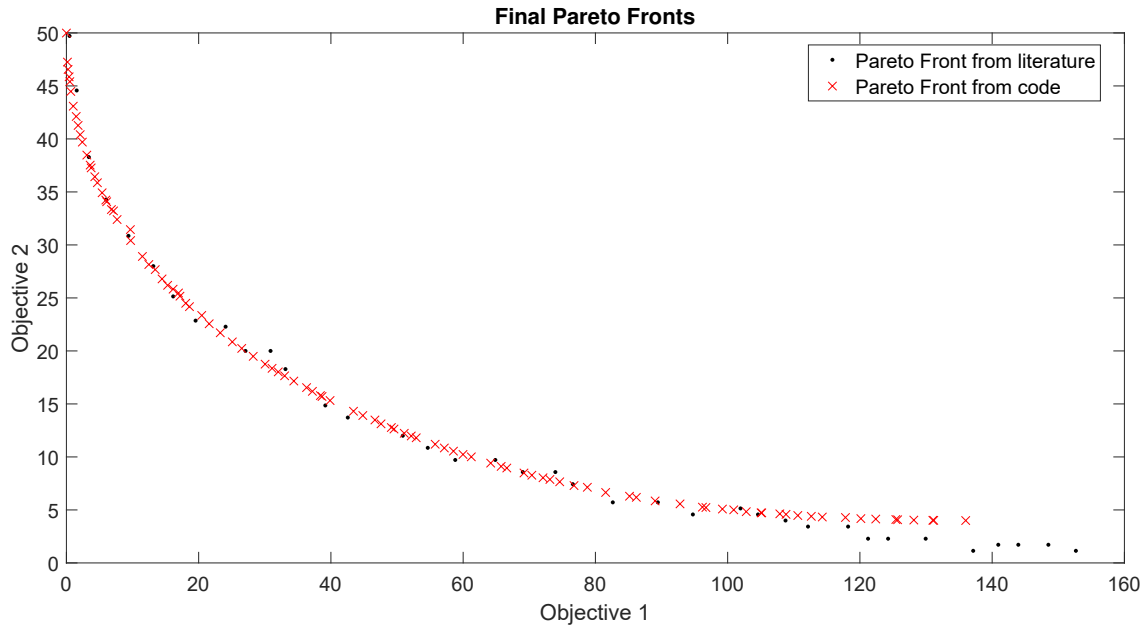

Figure A.4: Comparison of two Pareto fronts obtained from the literature [4] and the code used in the airfoil optimization for the Binh and Korn function function